UiT
THE ARCTIC
UNIVERSITY
OF NORWAY

Faculty of Science and Technology
Department of Physics and Technology

# Diagnostics of Ion Beam and Current Free Double Layer in Helicon Plasma Devices with Expanding Magnetic Field

—

**Njål Gulbrandsen**

*A dissertation for the degree of Philosophiae Doctor – April 2017*

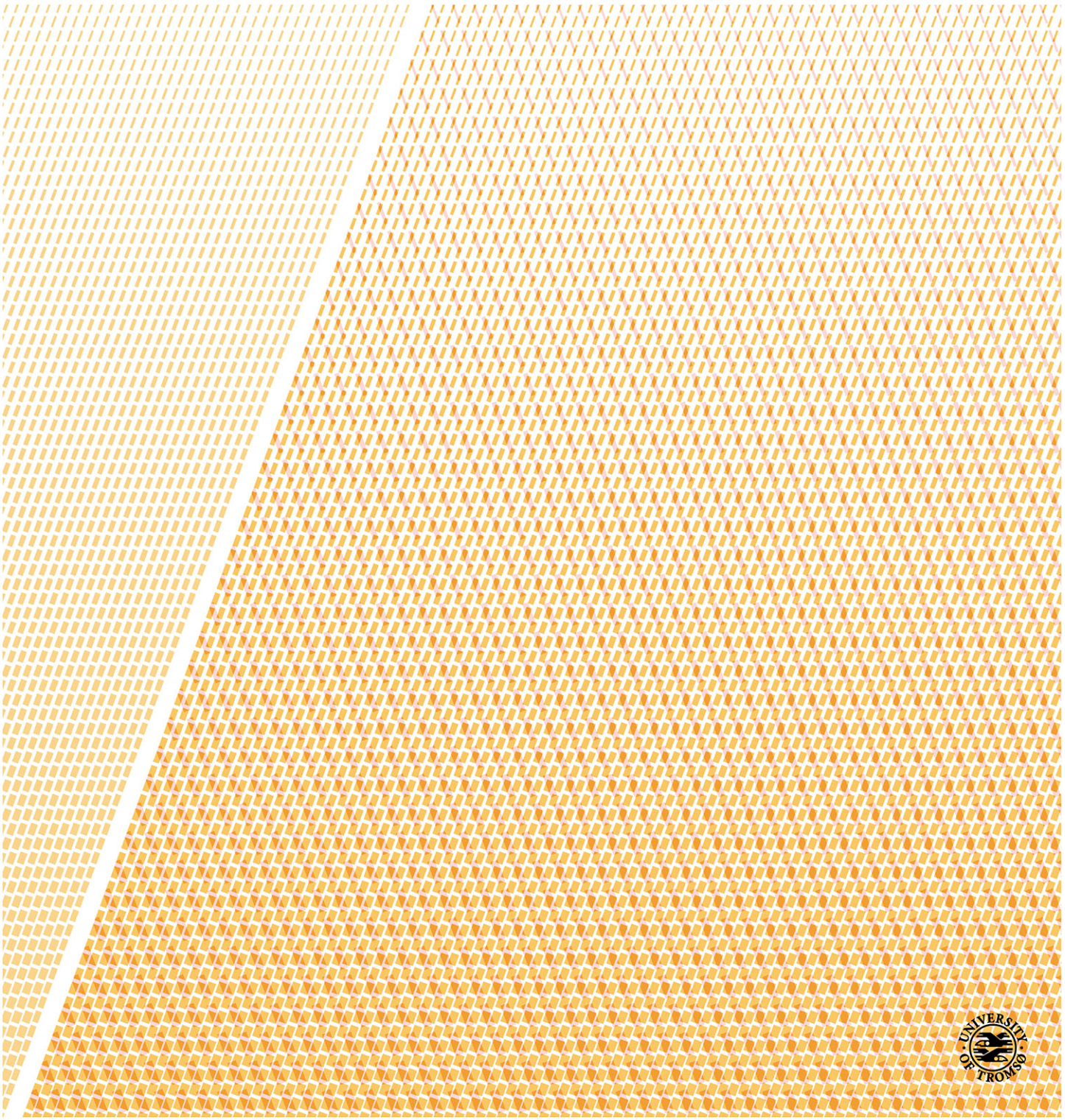

# Abstract

The main focus of this thesis is the diagnostics of ion beams in helicon plasma devices with expanding magnetic field, and running in an inductive mode. These ion beams are closely connected to the concept of current-free double layers (CFDL).

We started by investigating how to best interpret the measurements from a Retarding Field Energy Analyzer (RFEA) through 3-dimensional particle-in-cell simulation. A RFEA will be surrounded by a sheath. The ion distribution function (IDF) measured at the probe will be distorted compared to the IDF in the plasma unaffected by the sheath.

We discovered that the width of the distribution measured by RFEA was larger than expected from 1-dimensional theory. In addition, we found that the low energy part of the distribution was an effect of the probe acceptance angle. Wide acceptance angles give stronger signals at the expense of developing a low energy tail in the IDF. The low energy tails are due to ions entering the aperture at large inclination angles, so that a significant part of their momentum is in the tangential component of the velocity not seen by the probe. Due to the distorted picture of the IDF in the plasma, we found that for the relevant parameter range the RFEA can not provide a reliable ion temperature estimate.

We also found that the maximum (peak) of the IDF is at voltages slightly lower than the plasma potential. This could be associated with the potential drop in the presheath. Thus, the peak of the IDF can be associated with the plasma potential in the close vicinity to the analyzer.

Then we went on to compare RFEA-measurements with Laser Induced Fluorescence (LIF) measurements of ion velocity distribution. While the RFEA-diagnostics is intrusive and will disturb the plasma somewhat, the LIF-diagnostics is none-intrusive. The RFEA measures the ion distribution after it has been accelerated through the sheath surrounding the probe while LIF measures the ion velocity distribution in the plasma itself, without disturbing it. A new method to compare the two techniques is presented. By converting the LIF velocity distribution to an equivalent of a RFEA measurement using a simplified sheath model, we found good agreement between beam energies of the two methods. We also observed that the RFEA is capable of measuring ion beams with densities too low for the LIF to resolve, while the LIF-technique better resolves the back-ground ion distribution. We compare LIF and RFEA measurements in two different helicon plasma devices, the Njord device at the University of Tromsø and the HELIX-LEIA device at West Virginia University.

At last, we apply a RFEA to measure high-energy electrons. By inverting the grid volt-ages, a RFEA can be used to measure electrons. Only electrons with energies high enough to overcome the sheath will reach the probe. Therefore, we would only measure the high-energy part of the electron distribution.

# Acknowledgments

First, I like to thank my supervisor Åshild Fredriksen for help and guidance, and especially for been so patient with me these last years.

Then I like to thank Earl Scime and his group at the West Virginia University where I stayed 10 months as a guest researcher in 2012. The things I learned in the lab there was crucial for this project. I would especially like to thank Jerry Carr jr. for good cooperation and help with the LIF-measurements, and for the great sightseeing trips in Pennsylvania. I would also like to mention Dustin McCarren who taught me the secrets of how to optimize a Toptica diode laser, Matthew Galante who was the expert of cleaning and optimizing the dye laser, and Richard Magee who worked on the TALIF-project, in addition to the rest of the students in the lab, Stephanie Sears, Greg Lusk, Robert Vandervort and Michael Lindon.

I should also mention my friend and colleague Woichiech Miloch who I cooperated with on the RFEA-simulations.

Finally, I like to thank the technical staff at the plasma labs and workshops at the University of Tromsø and West Virginia University for their skilled and helpful assistance.

# Contents

**Abstract** iii

**Acknowledgments** v

**1 Introduction** 1

**2 Experimental setup** 5
2.1 UiT Njord system . . . 5
2.1.1 Magnetic field configurations in Njord . . . 7
2.2 The WVU HELIX-LEIA-system . . . 9

**3 Diagnostics** 11
3.1 Langmuir probes . . . 11
3.2 Emissive probes . . . 15
3.3 Retarding Field Energy Analyzer (RFEA) . . . 17
3.3.1 Energy resolution . . . 21
3.3.2 Probe construction . . . 23
3.3.3 Comparing grid configurations . . . 25
3.3.4 RFEA measurements of high energy electrons . . . 27
3.4 Laser Induced Fluorescence (LIF) . . . 29
3.4.1 UiT LIF-system . . . 30
3.4.2 WVU HELIX-LEIA LIF system . . . 34
3.4.3 Zeeman broadening . . . 35

**4 Plasma background measurements** 37
4.1 Emissive probe measurements . . . 37
4.2 Langmuir probe measurements . . . 40
4.3 RFEA measurements in Njord . . . 45
4.4 Radial profiles of HELIX-LEIA . . . 52
4.5 Radial profiles in Njord . . . 55
4.6 Summarizing observations . . . 59

**5 Articles** 61

**Paper 1:**
The role of acceptance angle in measurements with ion energy analyzers: Study by numerical simulations . . . 65

**Paper 2:**
Ion velocity distributions in the sheath and presheath of a biased object in plasma 71

**Paper 3:**
Interpretation of Ion Velocity Distributions Measured with a Grounded Retarding Field Energy Analyzer (RFEA) in an Inductively Coupled Helicon Plasma . . . 79

**Paper 4:**
A comparison of ion beam measurements by retarding field energy analyzer and laser induced fluorescence in helicon plasma devices . . . . . 87

**Paper 5:**
RFEA Measurements of High-Energy Electrons in a Helicon Plasma Device with Expanding Magnetic Field . . . . . 103

**Bibliography** **119**

# Chapter 1

# Introduction

Plasmas generated by radio-frequency (RF) waves have been studied for over 100 years [1]. RF plasma sources are now widely used in the semiconductor industry and for various surface processing [2]. They have developed from low-density, capacitively-coupled RF-sources to inductively coupled (IC) sources with higher densities and more effective processing capabilities [3]. The quest for even higher plasma densities also led to the invention of helicon devices [4], in which an external magnetic field was applied, coupling the RF waves to the whistler mode wave. Such a wave-coupled plasma provided a highly efficient plasma production with densities increasing by one to two orders of magnitude [5, 6].

As these sources displayed all the different coupling regimes, depending on working gas pressure, magnetic field, and applied power, they became subject to active research in the following decades. In 2003, the detection of a spontaneously formed potential drop at the intersection between the plasma source and a larger diffusion chamber was reported for a helicon device in a low-pressure, inductively coupled mode [7, 8]. The potential drop was named Current-Free Double Layer (CFDL), and the discovery opened up a new and active field of research on inductively coupled helicon devices.

Double layers (DLs) are sharp potential drops inside and away from walls in a plasma, and consists of two oppositely charged space charge layers. They are known to exist in space plasmas, and they were extensively studied in laboratories during 1970-80s [9–13]. Across such a double layer, ions and electrons are accelerated in opposite directions, and the plasma is separated into two different regimes, usually with different plasma parameters, such as plasma density, potential and electron and ion temperatures. In particular, beams of ions from upstream (in the direction of the ion flow) can be observed in the downstream region of the double layer. Figure 1.1 shows a classical example of the potential structure, electric field and charge distribution in a double layer, also indicated are the most common movements of charged particles.

The significance of the discovery of the CFDL was due to the fact that it formed spontaneously without externally applied potential drop, contrary to previous laboratory experiments. No externally applied currents or potentials was generating the CFDL, and thus it was named

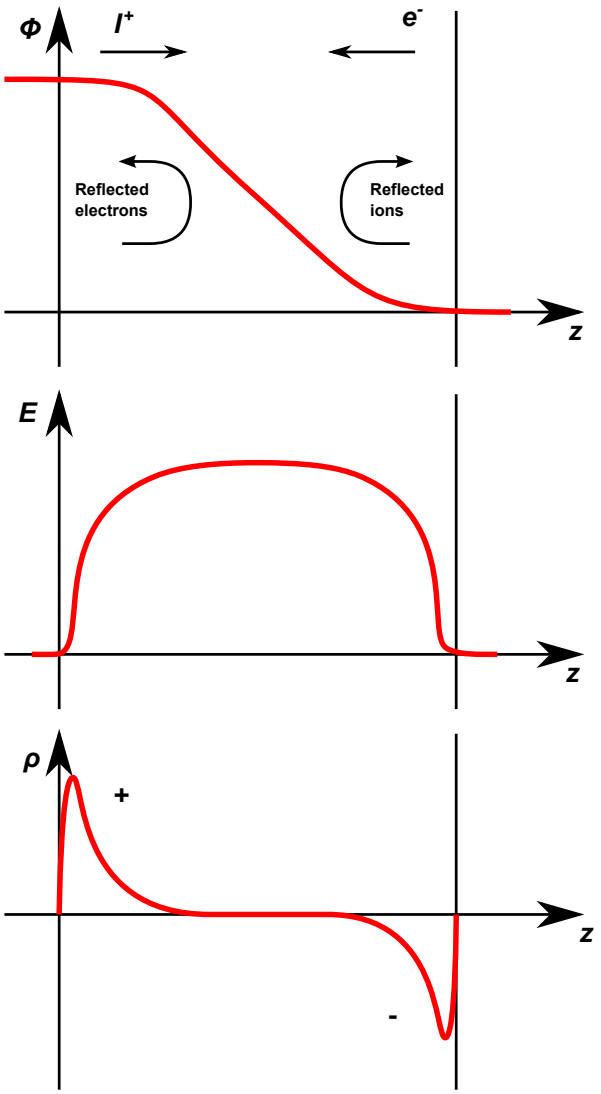


**Figure 1.1:** Potential, electric field and space charge distribution through a double layer. (Adapted from Block [9])

"current-free". The spontaneous formation of a DL with resulting ion acceleration into a beam, was soon acknowledged as an interesting candidate for an electrodeless and simple ion thruster [14, 15]. During the last decade, the research to understand, measure and control the beam formation from a CFDL has been carried out at a large number of universities world-wide [16–29] As a result of a potential the drop set up between the source and the diffusion chamber an ion beam is formed. As no external current is necessary to form this ion beam, the free electrons in the CFDL in the downstream plasma, play an important role in balancing the ion current in the beam.

Such beams are typically observed a short distance after the source plasma has flowed into an expansion chamber downstream from the source. Control parameters usually must be set to low collisionality, and magnetic field lines normally expand from the magnetized source plasma

into the low-magnetized or unmagnetized plasma in the expansion chamber.

Some theoretical models and numerical simulations have been carried out on CFDL [30]. The first one-dimensional modeling [31] and 1D PIC simulations [32] were able to reproduce the potential drops and an ion beam was produced in the simulations.

Later, others [14, 24, 33, 34] have pointed out the 2D nature of the CFDL, in that the electrons follow the magnetic field lines and escape towards the side walls, while the non-magnetized ions follow a straight path from the source into the expansion chamber [35].

The most commom diagnostics of ion beams is using a retarding field energy analyzers (RFEAs) [7]. Such probes measure ion current to a collector as a function of applied potential to a so-called discriminator grid in front of it, such that a representation of the ion velocity distribution can be obtained. Often these probes can be rotated to measure the ion distribution in different directions; assuming the probe scale is much smaller than the particle gyroradius. However, for a closer investigation of the ion distributions, the probe has the drawback that its housing is relatively large and commonly grounded and therefore surrounded by a sheath with a potential drop of about 10 V and up to 100 V in some cases. In addition, RF-produced plasmas exhibit oscillations in the plasma potential. These two effects distort and broaden the measured distribution to the extent that it is generally not possible to truthfully restore the ion velocity distribution in the undisturbed plasma. Instead, the probe measures the ion distribution entering the probe after having passed the sheath [36].

Laser Induced Fluorescence (LIF) diagnosis [37] is not intrusive, unlike the rather large RFEA probes, and it provides direct measurements of the velocity distribution of metastable ions, which is interpreted as a representation of the velocity distribution of the entire ion population [38]. The availability of tunable diode lasers with more than 10 mW effective power has made LIF-diagnostics more feasible for this type of plasmas. LIF diagnostics using tunable diode lasers were first implemented by Severn et al. [37] Low-power LIF using tunable diode lasers was later implemented at West Virginia University (WVU) [39] and was soon afterward applied in studies of flow [40]. These measurements were followed by LIF investigations of beam plasmas at Princeton Plasma Physics Laboratory (PPPL) [16] and Australian National University (ANU) [17, 26].

Still, LIF diagnosis of such beam-plasma systems is less common than RFEA measurements. Direct comparisons between the two diagnostics are rarely encountered [36], and the method of comparison has to our knowledge not yet been investigated in detail. Earlier efforts to compare the two types of diagnostics, have been based on fitting an expression for an idealized collector current from two drifting Maxwellian populations to the measurements [36, 41].

In our contribution, we have focused on the measurement of the downstream ion and electron populations in CFDL configurations. Using both retarding field energy analyzers (RFEA) and Laser Induced Fluorescence (LIF) we have investigated ion beams at different pressures and in different helicon plasma devices.

# Chapter 2

# Experimental setup

The experiments were conducted in two different plasma devices, the Njord device at the University of Tromsø (UiT) and the HELIX-LEIA chamber at West Virginia University (WVU). The devices are similar in that they are cylindrical and their helicon sources are operated in inductive mode, producing a high-density low-temperature plasma which expands into a larger chamber. However, there are differences in dimensions as well as magnetic field and radio frequencies applied. Below, a more detailed description of the two sources and their diagnostics systems are given.

## 2.1 UiT Njord system

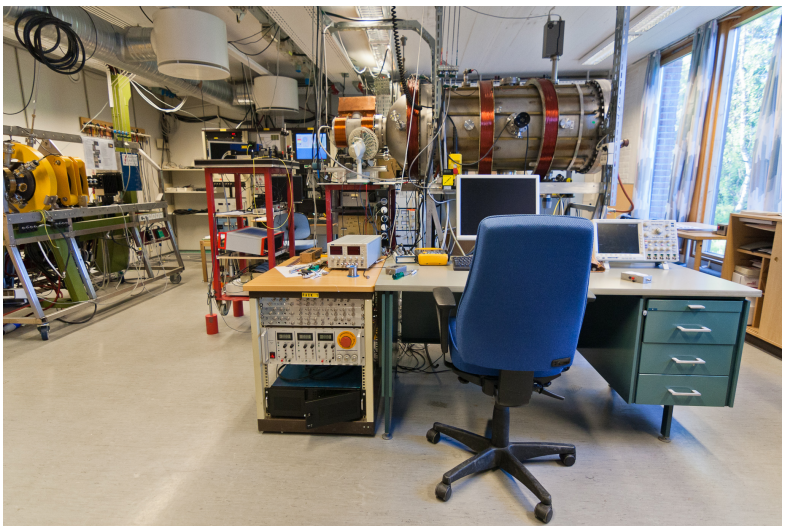

**Figure 2.1:** Photo of the UiT plasma lab with the Njord device

The Njord device (figure 2.1) at the University of Tromsø (UiT) is an inductively coupled helicon plasma device [23, 42]. The source consists of a 30 cm long, 13 cm diameter Pyrex tube with a Boswell type [4] saddle antenna wrapped around it, coupling up to 1000 W of RF-power at

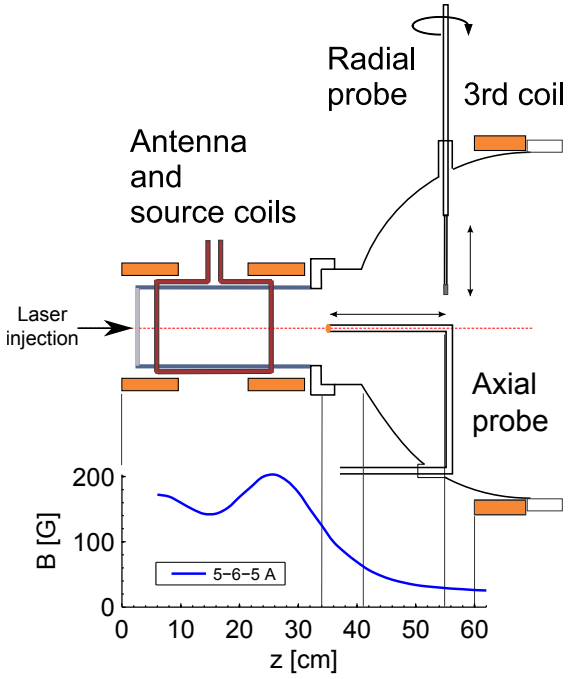


**Figure 2.2:** The UiT Njord device. Origin of the z-axis is placed at the edge of the first source coil. Below, a plot of the axial magnetic field used.

13.56 MHz to the argon gas. Two magnetic field coils are placed around the source tube. (figure 2.2)

The outer edge of the first source coil defines $z = 0$ and positive $z$ is in the direction of the gas flow, from source to the expansion chamber. The source itself starts at $z = 4$ cm. Another field coil is placed at $z = 60$ cm. This coil provides a downstream magnetic field of to improve dostream confinement and to prevent electrons from the near wall region of the source from getting lost at the walls of the large port.

In our study we used a current of 5 A in the first coil and 6 A in the second coil to produce a maximum magnetic field of 200 G in the source. In most of our experiments, we alo applied a current of 5 A in the third coil. To identifi a certan magnetic field configuration we name them after the currents in the coils, so 5-6-5 A configuration is the one with 5 A in the third coil, while the 5-6-0 A configuration has no current in the third coil. (see figure 2.3 in section 2.1.1).

The plasma expands through a 20 cm diameter, 8 cm long port into a 120 cm long, 60 cm diameter expansion chamber. A turbomolucular pump connected to the expansion chamber keeps the background pressure at $10^{-6}$ Torr.

Argon gas is fed to the source through an inlet in a grounded aluminum end plate of the source (at $z = 4$ cm in figure 2.2). The flow is controlled by a MKS flow controller and kept between 1.1 and 2.0 SCCM in this study, giving rise to pressures of 0.2 – 0.4 mTorr (30 –50 mPa) in the expansion chamber.

An axial probe feedthrough, indicated in figure 2.2, can be fitted with a probe that can

**Table 2.1:** Comparing typical parameters

| | HELIX (source) | LEIA at 80 cm | Njord (source) | Njord (downstream) |
|---|---|---|---|---|
| Pressure, $P$ (Pa) | $9.4 \cdot 10^{-2}$ Pa | $1.3 \cdot 10^{-2}$ Pa | | $4.2 \cdot 10^{-2}$ Pa |
| Pressure, $P$ (Torr) | 0.71 mTorr | $9.9 \cdot 10^{-5}$ Torr | | $3.1 \cdot 10^{-4}$ Torr |
| Magnetic field, $B$ (G) | 900 G | 22 G | 200 G | 29 G |
| Magnetic field, $B$ (T) | $9.0 \cdot 10^{-2}$ T | $2.2 \cdot 10^{-3}$ T | $2.0 \cdot 10^{-2}$ T | $2.9 \cdot 10^{-3}$ T |
| RF power | 650 W | | 1000 W | |
| RF frequency | 9.5 MHz | | 13.56 MHz | |
| Plasma density, $n_i$ | $3 \cdot 10^{11}$ cm$^{-3}$ | $7 \cdot 10^{9}$ cm$^{-3}$ | $2 \cdot 10^{11}$ cm$^{-3}$ | $3 \cdot 10^{10}$ cm$^{-3}$ |
| Electron temperature, $T_e$ | 3 eV | 4 eV | 8 eV | 6 eV |
| Ion temperature, $T_i$ | 0.7 eV | 1 eV | | 0.2 eV |
| Floating potential, $V_f$ | 2.0 V | $-1.5$ V | 27 V | 10 V |
| Plasma potential, $V_p$ | 40 V | 14 V | 60 V | 45 V |
| Debye length, $\lambda_D$ | 24 $\mu$m | 170 $\mu$m | | 110 $\mu$m |
| Beam mean free path $\lambda_b$ [a] | 7.3 cm | 53 cm | | 16 cm |
| Ion mean free path $\lambda_{\text{simp}}$ [b] | 4.5 cm | 32 cm | | 10 cm |
| Electron Larmor radius, $r_{L,e}$ | $6.7 \cdot 10^{-5}$ m | $3.0 \cdot 10^{-3}$ m | | $2.9 \cdot 10^{-3}$ m |
| Ion Larmor radius, $r_{L,i}$ | $8.5 \cdot 10^{-3}$ m | 0.43 m | | 0.14 m |
| Electron cyclotron frequency, $\omega_{ce}$ | $1.6 \cdot 10^{10}$ rad/s | $3.9 \cdot 10^{8}$ rad/s | | $5.1 \cdot 10^{8}$ rad/s |
| Ion cyclotron frequency, $\omega_{ci}$ | $2.2 \cdot 10^{5}$ rad/s | $5.3 \cdot 10^{3}$ rad/s | | $7.0 \cdot 10^{3}$ rad/s |
| Plasma frequency, $\omega_{pe}$ | $3.2 \cdot 10^{10}$ rad/s | $4.7 \cdot 10^{9}$ rad/s | $2.5 \cdot 10^{10}$ rad/s | $9.8 \cdot 10^{9}$ rad/s |
| Ion Plasma frequency, $\omega_{pi}$ | $1.2 \cdot 10^{8}$ rad/s | $1.7 \cdot 10^{7}$ rad/s | $9.1 \cdot 10^{7}$ rad/s | $3.6 \cdot 10^{7}$ rad/s |
| Electron thermal velocity, $v_{th,e}$ | $1.1 \cdot 10^{6}$ m/s | $1.2 \cdot 10^{6}$ m/s | | $1.5 \cdot 10^{6}$ m/s |
| Ion thermal velocity, $v_{th,i}$ | 1800 m/s | 2300 m/s | | 1000 m/s |
| Bohm velocity, $u_B$ | 2780 m/s | 3030 m/s | 4450 m/s | 3870 m/s |
| Plasma parameter, $N_D$ | $1.7 \cdot 10^{4}$ | $1.5 \cdot 10^{5}$ | $9.3 \cdot 10^{4}$ | $1.5 \cdot 10^{5}$ |
| Plasma $\beta$ | $1.1 \cdot 10^{-5}$ | $6.3 \cdot 10^{-4}$ | | $3.0 \cdot 10^{-4}$ |

[a] for 25 eV beam[3]
[b] calculated from [2, p. 32]

be moved axially for a distance of 20 cm. At $z = 55$ cm the chamber has three radial probe feedthrough Conflat ports, also indicated in figure 2.2. Typical parameters for the Njord device is given in table 2.1.

### 2.1.1 Magnetic field configurations in Njord

Figure 2.3 shows the magnetic field measured in Njord for different currents in the 3rd coil. the magnetic field configurations are named after the currents used in the three magnetic coils so that configuration 5-6-0 A has a current of 5 A in the fist coil, 6 A in the second coil and no current in the third coil and so forth. The main effect of the third coil is to increase the downstream magnetic field.

Using the magnetic field measurements from figure 2.3, we have calculated the magnetic field lines originating in the source of Njord for the configurations 5-6-0 A and 5-6-5 A. This is shown in figure 2.4. The magnetic field is assumed to be radially homogeneous in the source and

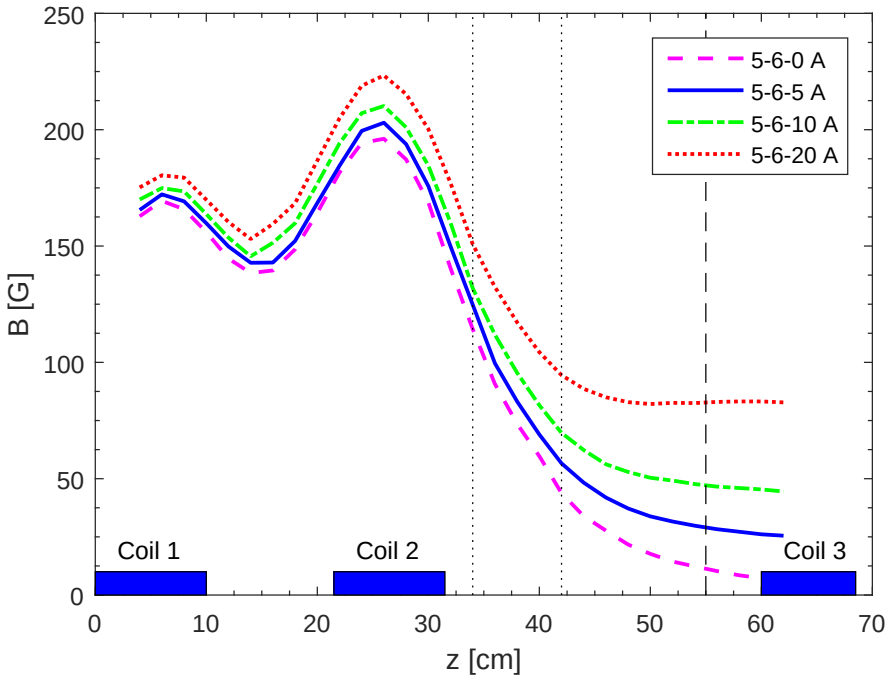


**Figure 2.3:** Magnetic field in Njord measured along the central axis. The vertical dotted lines marks the junctions between the source, the port and the expansion chamber. The vertical dashed line marks the position of the radial probes.

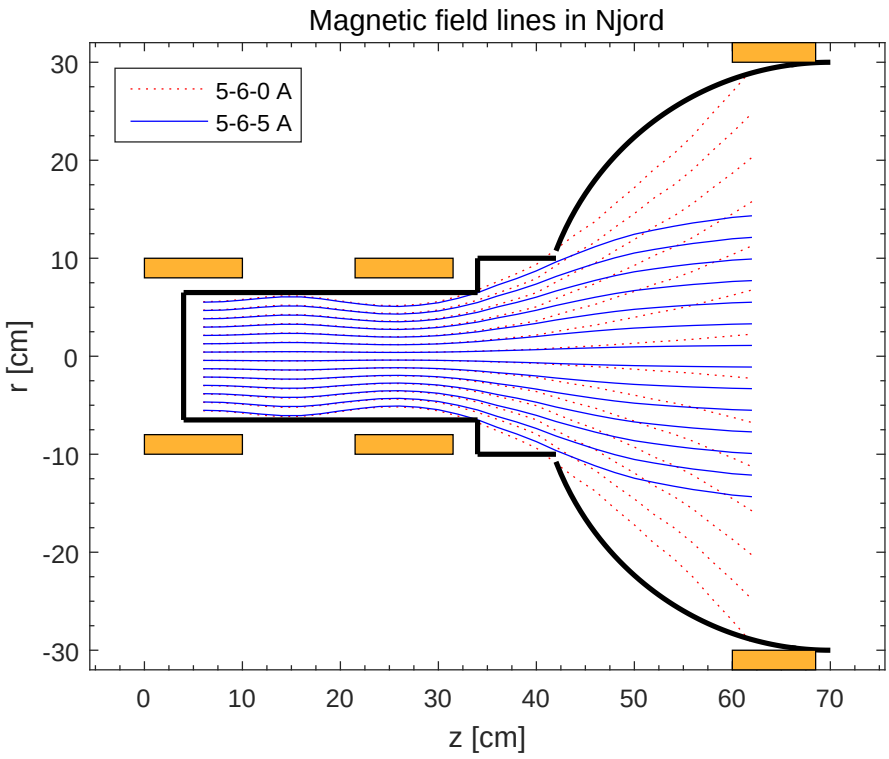


**Figure 2.4:** Magnetic field lines in Njord

the field lines are calculated using the expression [35]:

$$\frac{B}{B_0} = \left(\frac{r_0}{r}\right)^2 \tag{2.1}$$

where $r_0$ is the radius of the source and $B_0$ is the magnetic field in the source. The field lines for no downstream magnetic field (5-6-0 A) in figure 2.4 is seen to continue to expand as we move further down in the expansion chamber while the field lines for the 5-6-5 A configuration expand less and is almost straightened out downstream around $z = 60$ cm, near the third coil. The outermost field line in the 5-6-0 A configuration connects with the walls of the port between the source and the expansion chamber, but at 5-6-5 A configuration the outermost field line no longer connects to the port. When the field line connects with the walls of the port it might interfere with the plasma production, so we have choosen to use a 5 A current in the downstream coil for most of our measurements, producing a downstream magnetic field of 30 G to ensure that the outermost field line enter the expansion chamber.

## 2.2 The WVU HELIX-LEIA-system

**Figure 2.5:** Photo of the WVU HELIX-LEIA-system.

The Hot hELIcon eXperiment (HELIX)[43] at West Virginia University (WVU), shown in figure 2.5 and 2.6, consists of a 61 cm long Pyrex tube, 10 cm in diameter, connected to a 91 cm long, 15 cm diameter stainless-steel chamber. This chamber expands into a 4.5 m long, 2 m diameter space simulation chamber LEIA (Large Experiment on Instabilities and Anisotropies) [44]. Two turbomolecular pumps at the other end of LEIA keeps the base pressure at $10^{-7}$ Torr. Argon is injected through a precision MKS mass flow controller into the stainless-steel chamber of HELIX (downstream of the source area). Flow rates in the range of 1.7 – 3.0 SCCM were used

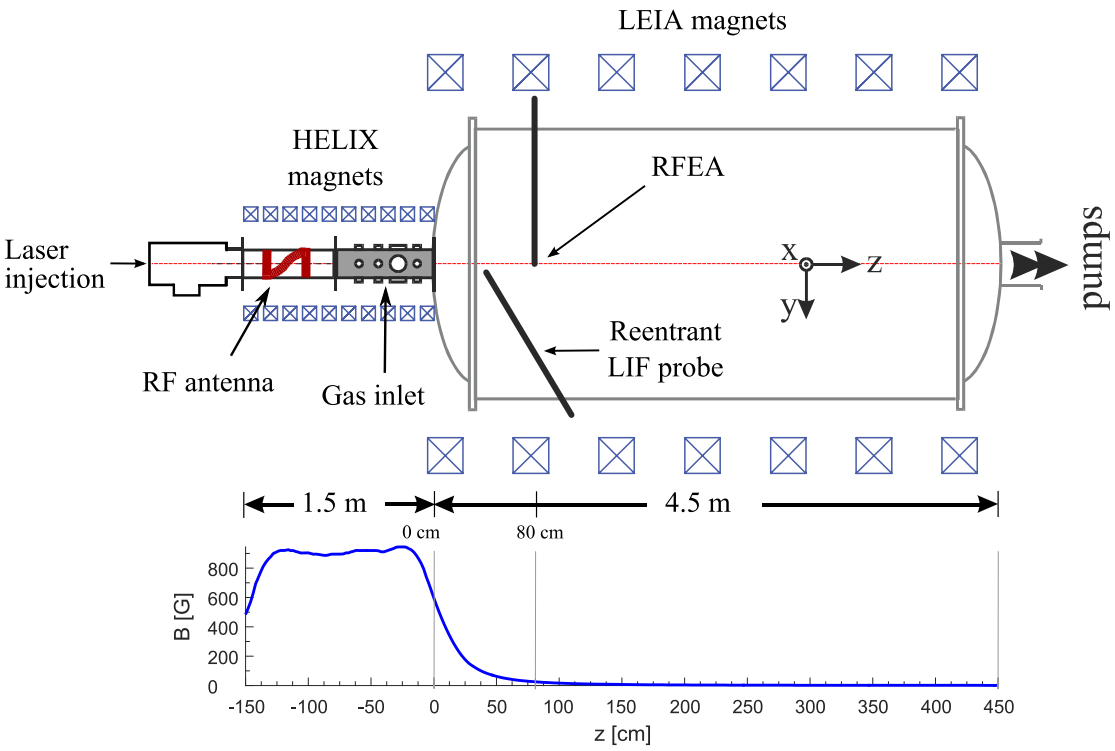


**Figure 2.6:** The WVU HELIX-LEIA-system. Origin of the z-axis is placed at the junction between the HELIX and the LEIA systems. Below, a plot of the axial magnetic field is shown.

in this study, resulting in a pressure range of 0.15 – 0.9 mTorr (20 – 120 mPa) in HELIX and 0.06 – 0.09 mTorr (8 – 12 mPa) in LEIA. An RF amplifier supplies 650 W of RF-power at 9.5 MHz to the plasma through a $\pi$ matching circuit. A 19 cm half wave helical antenna couples the RF-energy into the plasma (figure 2.6).

At HELIX, ten water-cooled electromagnets produce a steady state axial magnetic field of 0 – 1300 G. A magnetic field of 900 G was used in the measurements reported here. LEIA has seven water-cooled electromagnets, but these were not used in this study. Hence, the magnetic field is given by the HELIX magnets only. The junction between HELIX and LEIA is defined as $z = 0$ and positive $z$ is in the direction of gas flow from the HELIX-source into LEIA. At $z = 80$ cm the magnetic field is about 20 G. The main plasma parameters are given in Table (2.1).

The 91 cm stainless steel chamber on HELIX has four 6 inch Conflat crossing ports with viewports in the center of the chamber ($z \approx -45$ cm) for optical diagnostics. In addition four 2.75 inch Conflat ports are spaced evenly on either side of the larger ports (figure 2.6). LEIA has several ports for access with scanning internal probes. We are using a port at $z = 80$ for RFEA measurements and a rotatable vacuum feedthrough for the reentrant LIF probe located at $z = 132$ cm.

# Chapter 3

# Diagnostics

In low-temperature plasmas, the diagnostic tools of choice are electrical probes in various configurations. In-situ measurements by probes allow for the mapping of spatial variations in the plasma, and probes are usually simple, low-cost devices that can be constructed in-house. The main drawback of probes lies in the fact that the sheath around the probes as well as the geometry will influence the collected current, and furthermore, the probe itself disturbs to a certain extent the plasma locally. These properties complicate analysis of the signal and increase the uncertainties if the measurements.

Optical diagnostics, like spectroscopy and Laser Induced Fluorescence (LIF) measurements provide alternative means to obtain some plasma parameters. As it relies on emission lines from the atoms, this diagnostics will not disturb the plasma locally and is independent of current and sheath formations. On the other hand, the equipment cannot be constructed in-house and will generally be expensive to buy, and without additional fitting, measurements are generally not localized or it is hard to obtain measurements from more than one position. As optical and probe diagnostics are very different tools, the direct comparison between the methods is challenging. An important part of this work has been to provide a comparison between parameters obtained by LIF measurements and retarding field energy analyzer (RFEA) measurements. In the present chapter, we describe the probe and LIF diagnsostics which have been applied in this PhD project.

## 3.1 Langmuir probes

Langmuir probes are the most common type of electrostatic probe diagnostics in plasmas. In its simplest form it consists of a piece of conducting material biased by a voltage. The first theory for Langmuir probes was introduced by Irving Langmuir and Harold Mott-Smith [45] in 1926. The theory explores three basic forms, the planar Langmuir probe, the cylindrical Langmuir probe and the spherical Langmuir probe. Examples of Langmuir probes used at UiT can be seen in figure 3.1. In this study we used a cylindrical probe with a probe tip with length 5.3 mm and a diameter of 0.25 mm.

**Figure 3.1:** Examples of Langmuir probes used at UiT. The two upper probes are RF-compensated and the lower one is not compensated. The uppermost probe is the one used in this study.

In our analysis of the Langmuir probe measurements we mostly follows the techniques described by Merlino [46]. The electron current to a Langmuir probe is given as:

$$I_e(V_b) = I_{es} \cdot \exp\left(\frac{-e(V_p - V_b)}{kT_e}\right) \quad \text{for} \quad V_b < V_p \tag{3.1}$$

where $V_b$ is probe bias voltage, $V_p$ is the plasma potential and $T_e$ is the electron temperature. The electron saturation current, $I_{es}$ is given by:

$$I_{es} = -\frac{1}{4} A e n_e v_{e,th} = -A e n_e \sqrt{\frac{kT_e}{2\pi m_e}} \tag{3.2}$$

Where $A$ is the probe area, $n_e$ is the electron density, $m_e$ the electron mass and $v_{e,th} = \sqrt{8kT_e/\pi m_e}$ is the electron thermal speed. This current represent the probe current for $V_b = V_p$. For a planar probe this would also be the current for $V_b > V_p$, but for a cylindrical probe the current will continue to increase due to an increasing sheath size with increasing bias voltage.

As long as the electron temperature, $T_e$, is significantly larger than the ion temperature, $T_i$, ($T_e \gg T_i$) the ion saturation current, $I_{is}$, to the probe is determined by the Bohm ion current:

$$I_{is} = I_{\text{Bohm}} = 0.6 A e n_i \sqrt{\frac{kT_e}{m_i}} \tag{3.3}$$

Where $n_i$ is the ion density in the plasma and $m_i$ is the ion mass. To find an approximation of the ion saturation current, we used the current in the first point where derivative of the current went lower than $-0.0008$ mA/V. This is where the $I$-$V$-curve starts to curve downwards and before it has had time to change much.

The floating potential ($V_f$) can be read directly from the $I$-$V$-curve where the current ($I$) is zero. The plasma potential should be where all electrons in are captured and there is no longer any

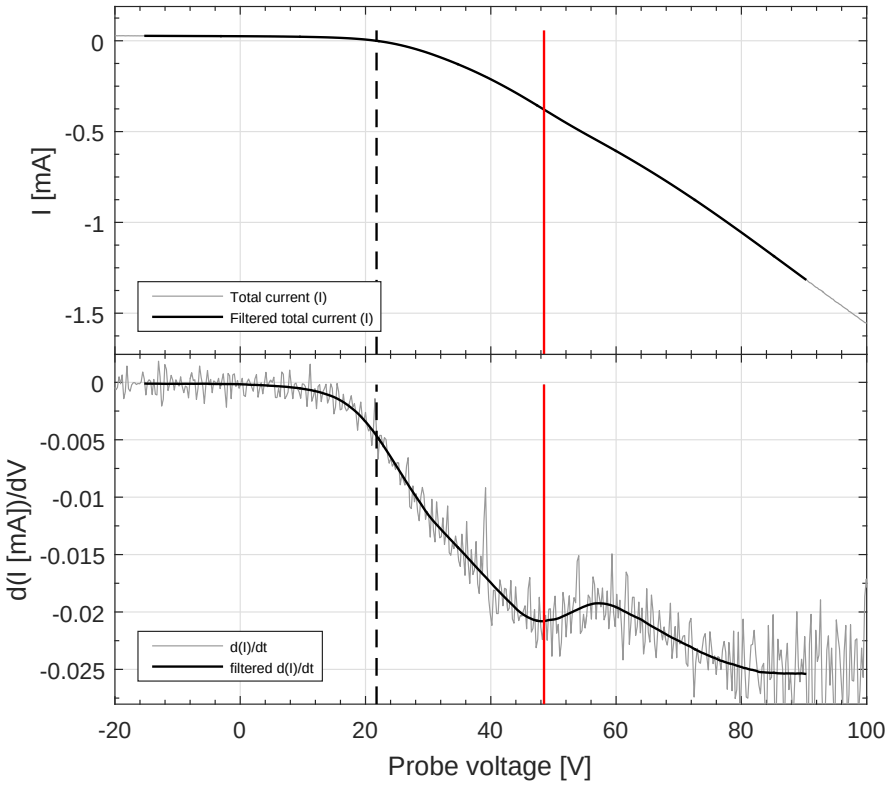


**Figure 3.2:** An *I-V*-curve from a langmuir probe with the first derivative. The solid vertical red line is the measured plasma potential ($V_p$) and the dashed vertical line is the floating potential ($V_f$). In the derivative the gray curve is the unfiltered data and the black curve is the Savitzky-Golay-filtered data. The measurment is done with a radial mounted langmuire probe at $z = 55$ cm, and $r = -18$ at with a pressure of 0.28 mTorr.

repelling effect from the bias voltage on the electrons. The current is then the electron saturation current. For a cylindrical Langmuir probe it is sometimes hard to find the plasma potential since the electron current will continue to increase even after it has reach electron saturation due to the effect of the expanding sheath with higher voltages [3]. We are using a local minimum of the derivative of the $I$-$V$-curve as an estimate of the plasma potential. We employ a 81 point, 4 degree Savitzky-Golay filter [47, 48] to find the derivative to avoid a noisy curve.

An example of an *I-V* curve from Njord with its derivative is shown in figure 3.2. From the *I-V* curve it self it is hard to see any indication of the plasma potential, but the derivative has a distinct minimum.

The exact electron saturation current is hard to find with a cylindrical probe, since it is very sensitive to the estimate of the plasma potential. We therefore use the ion saturation current to deduce the plasma density.

$$n = n_i = \frac{I_{is}}{0.6Ae\sqrt{\frac{kT_e}{m_i}}} \tag{3.4}$$

We find the electron current ($I_e$) by subtracting a linear fit of the ion saturation current from the total current. From equation (3.1) we can then derive the electron temperature ($T_e$) by taking

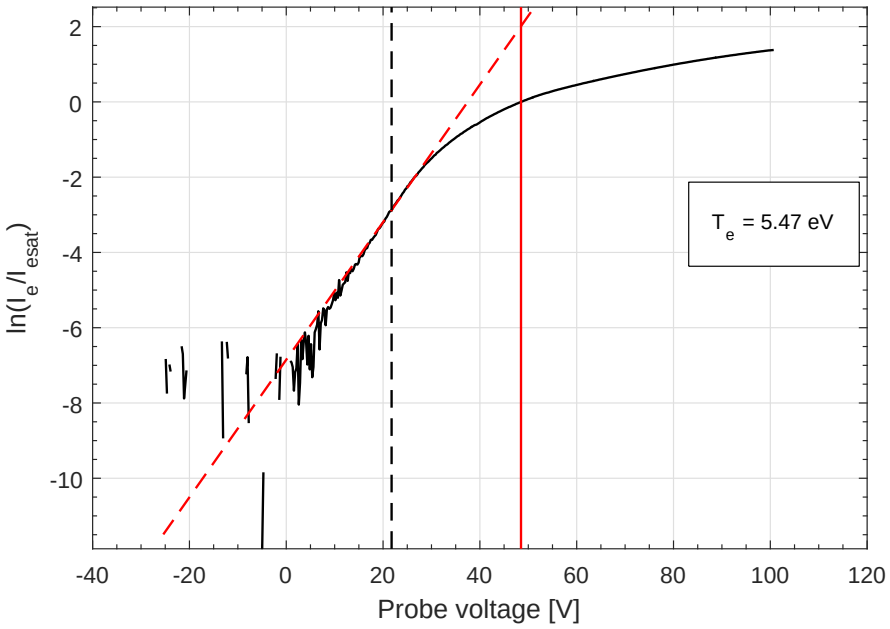


**Figure 3.3:** A plot of $\ln(I_e/I_{\text{esat}})$ versus probe voltage. The dashed tilted line is a linear fit to the area around the floating potential. The solid vertical line is the plasma potential ($V_p$) and the dashed vertical line is the floating potential ($V_f$).

the logarithm of the electron current divided by the electron saturation current:

$$\ln\left(\frac{I_e(V_b)}{I_{\text{es}}}\right) = \frac{e}{kT_e}\left(V_b - V_p\right) \tag{3.5}$$

This is now a linear function of the probe voltage where the slope is given by the electron temperature. To find the temperature we make a linear fit to the curve in the area around the floating potential. This is the area where the curve is most linear. Figure 3.3 shows an example of a plot of the logarithm of the electron current found from the measurement in figure 3.2. The dashed red line represents a linear fit around the floating potential used to derive a temperature.

Since we are using an RF-generated plasma, RF- fluctuations will be present in the plasma and these fluctuations will interfere with the Langmuir probe measurements [49]. The voltage of the probe is scanned much slower than the RF-period so in every point of the Langmuir scan we are measuring the current averaged over the RF-fluctuations. To prevent the RF-fluctuations from disturbing our analysis we can filter them out by a bandpass filter. We have used the technique described by Sudit and Chen [50] applying filters close to the probe tip to block out the fluctuations. A second probe tip with a larger area is connected to the measuring probe tip through a 50 pF capacitor to short circuit the RF-signal. Then a parallel coupling of a $8\mu$H inductor and a 17.2 pF capacitor makes up a notch filter that blocks out the 13.56 MHz RF signal (figure 3.4).

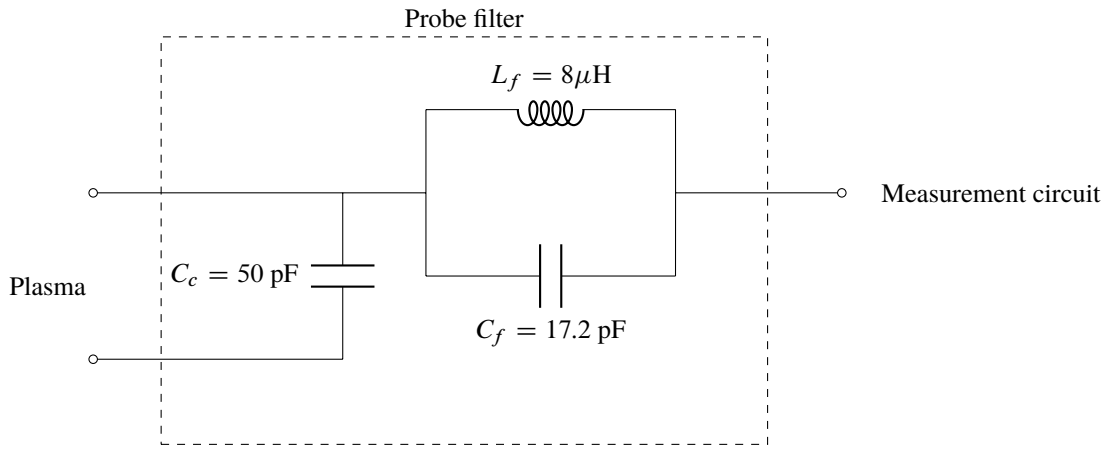


**Figure 3.4:** Filter circuit in the compensated Langmuir probe.

## 3.2 Emissive probes

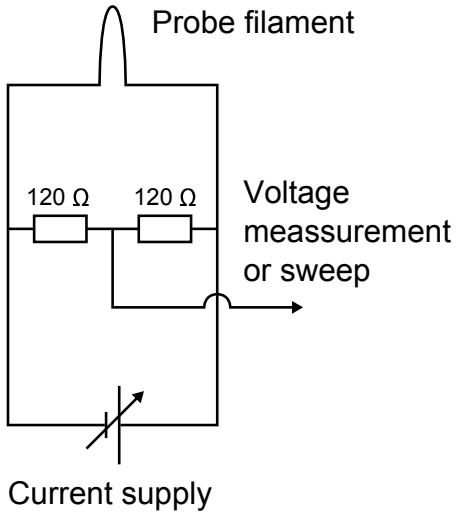


**Figure 3.5:** Sketch of the emissive probe heating circuit.

The emissive probe is a version of the Langmuir probe where the probe tip can be heated until it starts to emit electrons [51]. The most common way of heating the probe is by using a filament heated by a current as a probe tip (figure 3.5). When the probe is biased negatively relative to the plasma potential these electrons will escape from the sheath into the plasma. This gives rise to a positive current that is added on top of the small ion current to the probe. When the probe is biased positively relative to the plasma the emitted electrons are captured again by the probe and we only draw an electron current from the plasma in the same manner as a "cold" Langmuir probe [51, 52].

The most accurate way of analyzing an emissive probe is by the "Inflection-point" method

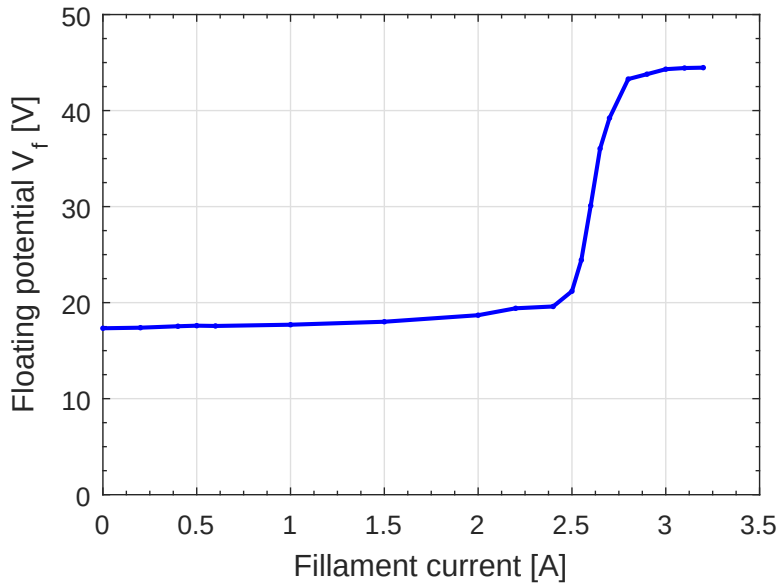


**Figure 3.6:** Floating potential from the emissive probe as a function of filament current taken at position z = 55 cm in the center of Njord at a pressure of 0.29 mTorr and RF-power of 800 W and a magnetic field configuration with 5 A in the first and second coil and no current in the third coil.

where the probe is scanned as a Langmuir-probe and the position of the peak of the derivative is taken as the plasma potential. With this method one is able to determine the plasma potential to an accuracy the order of $T_w/e$ for weak emissions, where $T_w$ is the filament temperature [52]. It is also possible to use this method in RF-plasmas where the distortions to emissive probe measurements is quite symmetric around the plasma potential. The derivative of time averaged $I-V$ characteristics would then yield two peaks. The middle position between these two peaks would then be an estimate of $V_p$ [53].

Unfortunately, our measurements from emissive probes in Njord does not yield a double peak for the parameters we are interested in. Instead, used the floating potential method where the floating potential at saturation is taken as the plasma potential. [51, 53]. When the emission current exceeds the electron saturation current, the emissive probe will float close to the plasma potential. This method is expected to give a potential slightly lower than the plasma potential with an accuracy of the order of $T_e/e$ [54, 55].

Figure 3.6 shows the floating potential, $V_f$, as a function of filament current for the emissive probe used in Njord. The floating potential saturates around 2.8 A. For all measurements of floating potential of emissive probe a filament current of 2.9 A was used. For the emissive probe we used a 0.125 mm thick tungsten wire as filament. The circuit used for heating the filament is shown in figure 3.5. The two resistors virtually place the measurement point in the middle of the filament so we do not have to bother with the potential drop across the filament.

## 3.3 Retarding Field Energy Analyzer (RFEA)

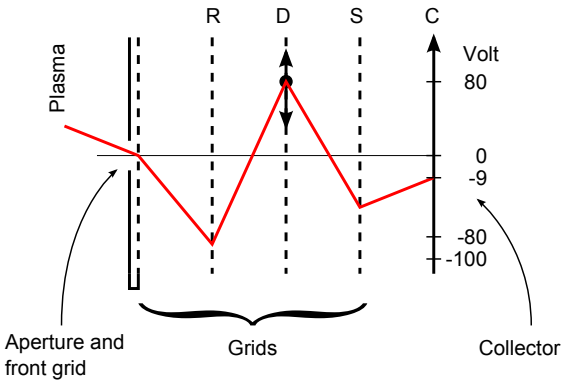


**Figure 3.7:** Typical grid configuration in an RFEA. An aperture and front grid keeps most of the plasma outside. Repeller grid (R), Discriminator grid (D), Secondary electron repeller (S), Collector (C). The red line marks the grid voltages used in this study.

To diagnose ions and ion beams in a plasma can be challenging. The most common way to diagnose ions is to use a gridded analyzer [56] often called Retarding Field Energy Analyzer (RFEA) [57] and sometimes Retarding potential analyzer (RPA) [58] or Electrostatic Analyzer [59].

The current to an ordinary Langmuir probe is dominated by the electrons due to their high mobility. To single out the ion contribution the electrons must be removed. In a RFEA a negatively biased grid is used to keep the electrons out. The ions are discriminated based on the kinetic energy parallel to an electric field inside the probe. This is achieved by sweeping the voltage of a discriminator grid or the collector [57]. Ions with sufficient kinetic energy to overcome the potential will reach the collector.

There exist several different designs of RFEAs. Some are placed in electrodes [60] or in the walls of a plasma chamber, others are mounted on probe shafts and can be moved around inside the plasma [61, 62].

The most common designs (figure 3.7) uses a front aperture, three or four grids and a collector. The first grid is either floating or grounded. The next grid is negatively biased to repel electrons (R) and one grid is swept through some voltage range to discriminate ions (D). A fourth grid, biased slightly more negative than the collector, can be used in front of the collector to prevent the escape of secondary electrons knocked off the collector by incoming ions (S). The collector is slightly negatively biased to attract the ions (C). The collector current will be a function of the sweep voltage at the discriminator grid [59].

RFEAs can also sometimes be used to measure energetic electrons [60–65]. This is done by inverting the polarity of the grids and collector, and skipping the secondary electron repeller.

As described above, the collector current $I_c$ is measured as a function of the discriminator grid potential $V_d$. This current is proportional to the ion flux to the collector which again is

assumed to be proportional to the ion flux at the probe entrance with a cutoff for velocities that cannot overcome the discriminator voltage. The current measured by the collector can then be given as [62]:

$$I(v_{\min}) = Ae \int_{-\infty}^{\infty} \int_{-\infty}^{\infty} \int_{v_{\min}}^{\infty} v_z f(\vec{v}) \mathrm{d}v_x \mathrm{d}v_y \mathrm{d}v_z \tag{3.6}$$

where $A$ is a constant depending on front-plate aperture, grid transmission factors and ion density and $e$ is the elementary charge, $v_{\min}$ is the minimum velocity for an ion to hit the collector given a certain grid potential, and $f(\vec{v})$ is the ion velocity distribution at the probe entrance, behind the plasma sheath, not in the plasma itself.

If we neglect the $x$ and $y$ directions we can rewrite this expression as [59, 62, 66]:

$$I(v_{\min}) = Ae \int_{v_{\min}}^{\infty} v f(v) \mathrm{d}v \tag{3.7}$$

Using energy conservation on the particles:

$$eV_d = \frac{1}{2} m_i v_{\min}^2 \tag{3.8}$$

where $V_d$ is the grid potential and $m_i$ is the ion mass, we find the minimum velocity as:

$$v_{\min} = \sqrt{\frac{2eV_d}{m_i}} \quad \text{for} \quad v_{\min} > 0 \tag{3.9}$$

where $V_d$ is the grid potential. We can now define a new variable $V$ so that:

$$eV = \frac{1}{2} m_i v^2 \quad \Rightarrow \quad v = \sqrt{\frac{2eV}{m_i}} \tag{3.10}$$

and $V(v_{\min}) = V_d$. With equation (3.10) we can substitute $V$ for $v$ in equation (3.7), using that $e\mathrm{d}V = m_i v \mathrm{d}v$, we get:

$$I\left(\sqrt{\frac{2eV_d}{m_i}}\right) = \frac{Ae^2}{m_i} \int_{V_d}^{\infty} f\left(\sqrt{\frac{2eV}{m_i}}\right) \mathrm{d}V \tag{3.11}$$

To solve the integral we assume there exists a function $F$ so that:

$$\frac{\mathrm{d}F\left(\sqrt{\frac{2eV}{m_i}}\right)}{\mathrm{d}V} = f\left(\sqrt{\frac{2eV}{m_i}}\right) \tag{3.12}$$

From equation (3.11) we then obtain:

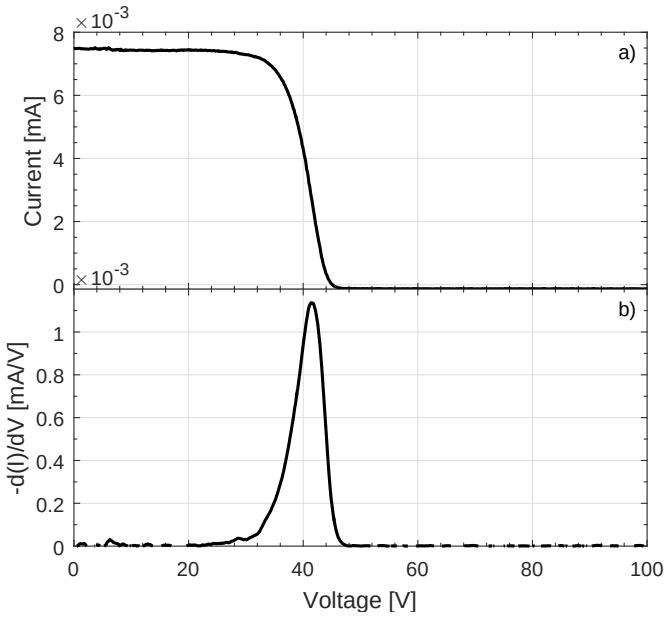


**Figure 3.8:** Typical grid RFEA measurements of a background plasma without ion beam. $P$ = 0.34 mTorr. The measurement is taken in Njord at the position 55 cm, 11 cm from the end of the source and radially close to the edge of the chamber, $r$ = 18 cm, facing perpendicular to the direction to the source. a) The collector current as a function of discriminator voltage. b) The derivative of the collector current as a function of discriminator voltage being proportional to the ion velocity distribution, *f(v)*.

$$
\begin{aligned}
I\left(V_d\right) &= \frac{Ae^2}{m_i} \int_{V_d}^{\infty} f\left(\sqrt{\frac{2eV}{m_i}}\right) \mathrm{d}V \\
&= \frac{Ae^2}{m_i}\left[F(\infty) - F\left(\sqrt{\frac{2eV_d}{m_i}}\right)\right]
\end{aligned} \tag{3.13}
$$

Assuming that $F(\infty)$ is finite we can differentiate this equation with regards to $V_d$:

$$
\frac{\mathrm{d}I(V_d)}{\mathrm{d}V_d} = -\frac{Ae^2}{m_i} f\left(\sqrt{\frac{2eV_d}{m_i}}\right) \tag{3.14}
$$

Solving for $f$ then gives:

$$
f(v_{\min}) = -\frac{m_i}{Ae^2}\frac{\mathrm{d}I(V_d)}{\mathrm{d}V_d} \quad \text{for} \quad v_{\min} > 0 \tag{3.15}
$$

From this expression we see that the ion velocity distribution function at the probe entrance is proportional to the derivative of the collector current with respect to discriminator voltage. Figure 3.8 and 3.9 shows examples of collector currents and corresponding derivatives.

To relate the ion velocity distribution at the probe to the ion velocity distribution in front of the sheath we have to make some assumptions about the effect of the sheath. The simplest

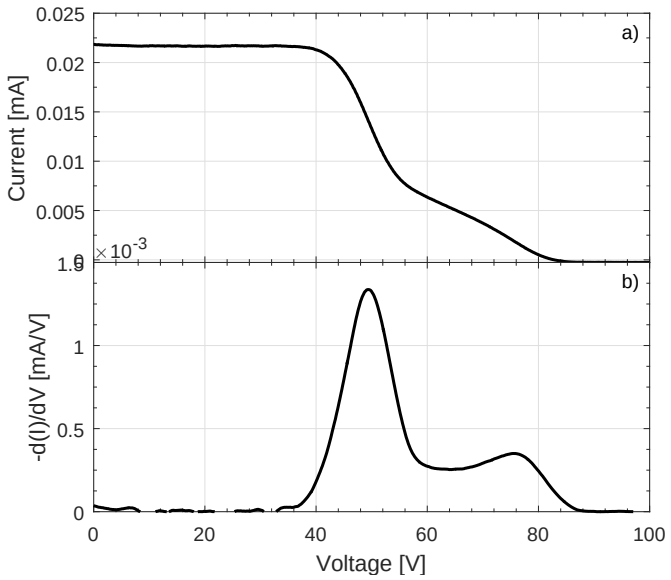


**Figure 3.9:** Typical grid RFEA measurements of a plasma with an ion beam. *P* = 0.28 mTorr. The measurement is taken in Njord at the position 55 cm, 11 cm from the end of the source and radially centered.a) The collector current as a function of discriminator voltage. b) The derivative of the collector current as a function of discriminator voltage being proportional to the ion velocity distribution, *f(v)*.

approach is to model a plasma sheath as a simple planar electrical potential drop (figure 3.10) where the potential in the plasma stays at the plasma potential, $V_p$, and the probe surface is at ground [67]. This will add a kinetic energy of $eV_p$ to the ions so that the velocity at the probe surface becomes:

$$v = \sqrt{v'^2 + \frac{2eV_p}{m_i}} \tag{3.16}$$

Where $v'$ represent the ion velocity in the plasma in front of the potential drop of the sheath. This expression is only valid for $v' > 0$. Ions moving away from the probe will never reach the surface in this model. By assuming no collisions and flux conservation through the sheath one find that [68]:

$$f(v) = f'(v') \quad \text{for} \quad v' > 0 \tag{3.17}$$

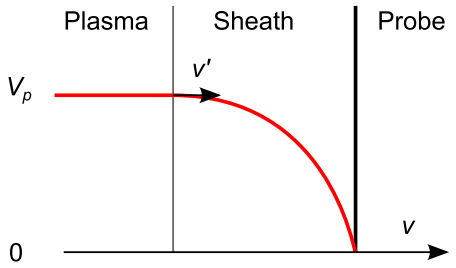


**Figure 3.10:** Simplified sheath model.

Where $f'(v')$ is the ion velocity distribution in the plasma.

In practice calculating an ion velocity distribution in the plasma from RFEA-measurements is seldom done. It would be very sensitive to a correct determination of the plasma potential. Instead, RFEA-measurements are usually presented as plots of $f(V_d)$ (or rather differential ion flux $-\mathrm{d}I/\mathrm{d}V_d$) plotted as a function of discriminator voltage, $V_d$ as shown in figure 3.8b and 3.9b. This distribution is often called the ion energy distribution function (IEDF), but this can be misleading since it is not really an energy distribution but instead a velocity distribution plotted with energy units on the velocity axis.[8] We choose to call this distribution the ion distribution function (IDF) [69].

### 3.3.1 Energy resolution

To resolve the ion energies it is important to avoid a buildup of space charge within the probe that alter the ion paths. This has some implications on the dimensions of the probe. The distance between the grids especially between the discriminator and the repeller should therefore be kept within $\sim 4$ Debye lengths ($\lambda_D$) [56]. This can be achieved by using aperture and grids with less transparency to reduce the density inside the probe and thereby increase the Debye length [70].

The energy resolution of a RFEA is partly determined by its geometry [59]. Studies [61, 71] have shown that the repeller to discriminator distance is the main factor.

RF-Oscillations in the plasma also affect the energy resolution. Using the model of Charles et. al [72]:

$$\frac{\Delta E}{2eV_{\mathrm{rf}}} = \frac{1}{\sqrt{1+\left(\frac{\omega\tau_{av}}{2}\right)^2}} \tag{3.18}$$

where $\Delta E$ is the energy broadening of the peak,$V_{\mathrm{rf}}$ is the RF-amplitude, $\omega$ is the RF-angular frequency and $\tau_{\mathrm{av}}$ is the average time taken for an ion to fall through the sheath, given as:

$$\tau_{\mathrm{av}} \approx \frac{1.2}{\omega_{pi}}\left(\frac{2eV_{\mathrm{dc}}}{KT_e}\right)^{\frac{1}{4}} \tag{3.19}$$

where $\omega_{pi}$ is the ion plasma frequency and $V_{\mathrm{dc}}$ is the sheath voltage. Using the parameters from Njord of $\omega_{pi} = 3.6\cdot 10^7$rad/s,$V_{\mathrm{dc}} = 45$ V, and $KT_e = 6$ eV we get an average time-of-flight through the sheath of $\tau_{\mathrm{av}} = 6.5\cdot 10^{-8}$ s. Combined with an RF-frequency of 13.56 MHz ($\omega = 85.2\cdot 10^6$ rad/s) this gives $\frac{\Delta E}{2eV_{\mathrm{rf}}} = 0.34$ so that the RF-broadening would be 34% of the RF-peak-to-peak-voltage. We have measured the RF in Njord using uncompensated Langmuir probe, to be about 1.5 $V_{\mathrm{pp}}$. This should give an RF-broadening in Njord of about 0.5 V. The parameters are fairly similar in HELIX-LEIA. The flight time through the sheath is $\tau_{\mathrm{av}} = 1.1\cdot 10^{-7}$ s and the ion plasma frequency $\omega_{pi} = 1.7\cdot 10^7$rad/s. With $KT_e = 4$ eV and a $V_{\mathrm{dc}} = 14$ V this results in $\frac{\Delta E}{2eV_{\mathrm{rf}}} = 0.29$.

Another factor affecting the energy resolution is the efficient acceptance angle, ie. the maximum angle of incoming ions that would reach the collector of the probe. We have seen from particle-in-cell simulations [69] (paper 1) that the acceptance angle contributes especially to a

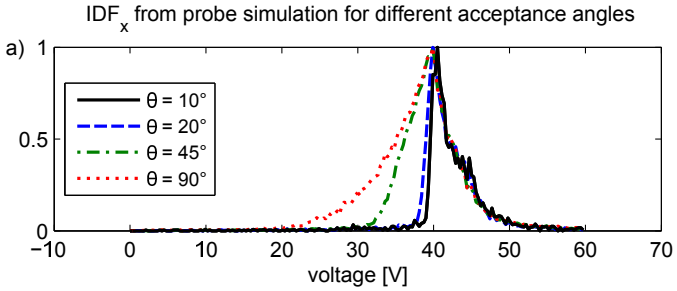


**Figure 3.11:** Simulation results of the effect of acceptance angle on the Ion distribution function (IDF). From Gulbrandsen et.al [73] (paper 3)

low energy tail. By decreasing acceptance angle the low energy tail in the IDF decreases (figure 3.11). The peak and the shape of the high energy part of the distribution seems to be unaffected of changes in the acceptance angle although a change in aperture will affect the total amount of ions entering the probe. The low energy tail can be explained by ions entering the aperture at large inclination angle, so that a significant part of their momentum is in the tangential component of the velocity.

Still, even without this tail the distribution is found to be much wider than expected [73, 74] (paper 2 and 3) resulting in artificially high temperature estimates from the distribution. Looking at the distributions in the sheath of the particle-in-cell simulations the full-with-half-maximum (fwhm) is first dropping to about half of the original distribution before they slowly start to increase as we go towards the probe (figure 3.12). This slow increase in fwhm in the inner part of the sheath appears to depend on the total voltage across the sheath. This indicates that there is some effect of weak electrostatic ion-ion collisions in the sheath altering the trajectory of the ions.

High temperature estimates has also been reported by Buzzi et. al. [75] and Andersen et al. [76] in magnetized cesium plasma. They attributed this to ion-ion collisions altering the direction of the particle trajectories.

In addition we would have electrostatic lensing effects inside the probe [71, 77, 78] due to grids and aperture. Figure 3.13 shows how variations in the voltage of the repeller grid changes

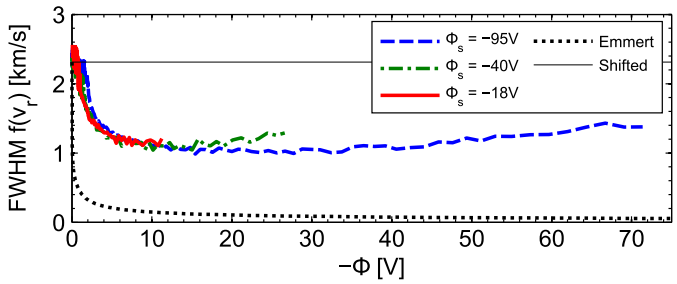


**Figure 3.12:** Simulation results of full-with-half-maximum (fwhm) of the ion velocity distribution as it is moving through the sheath. From Gulbrandsen et.al [73] (paper 3)

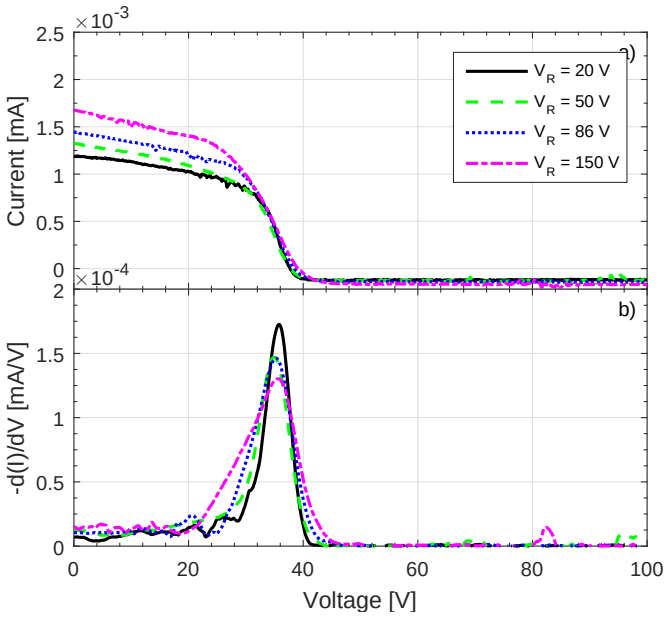


**Figure 3.13:** RFEA measurements in NJORD with varying repeller voltage. Change of repeller voltage changes the ion focusing inside the RFEA and thereby the effective acceptance angle. 2.0 sccm flow and 5-5-0 A magnetic field

the electrostatic lensing effects and alters the measured ion distribution. Comparing this to figure 3.11 we see the same effects as expected from a change in the acceptance angle of the probe.

### 3.3.2 Probe construction

Three different Retarding Field Energy Analyzers (RFEA) were used to measure Ion Distribution Functions (IDF) in this study. In measurements at WVU we used an RFEA with a ceramic housing. At UiT we used two different RFEAs, both with a grounded brass housing, of which one was mounted at a radial port looking perpendicular to the probe shaft and one was looking opposite to the probe shaft and mounted on the axial feedthrough.

#### Ceramic RFEA

For the WVU measurements we used a RFEA with a ceramic housing ($35 \times 22 \times 15$ mm) connected to a grounded probe shaft (figure 3.14a). The probe was oriented perpendicular to the shaft and could be rotated 360° around the axis to look in different directions. The probe was mounted at a radial port at $z = 80$ cm in LEIA (figure 2.6). This RFEA had four grids of stainless steel mesh with a transmission factor of 44% and 50$\mu$m wire spacing. Each grid was spotwelded to a 0.4 mm thick brass spacer. This probe had two front grids 0.4 mm apart, both electrically grounded. Two configurations of this probe were used, one with a 5 mm diameter aperture and one with a 7 mm diameter aperture. The remaining brass spacers had an inner diameter of 7 mm. Between the other grids, 0.5 mm thick ceramic spacers were used so that the distance between the grids was 0.9 mm. The ceramic spacer in front of the collector plate had an opening diameter

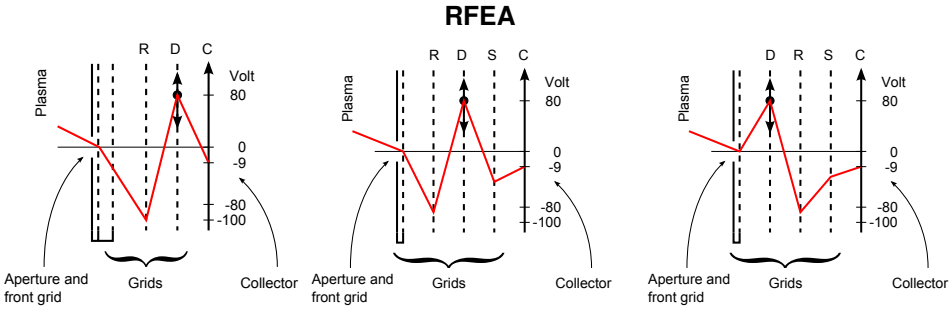


(a) Ceramic RFEA (b) Brass RFEA (c) Axial RFEA

**Figure 3.14:** Illustrations of the grid configurations in the different RFEA-probes. R is the repeller grid, D the discriminator grid, S the secondary electron repeller and C is the collector.

to match the front aperture, either 5 mm or 7 mm. This was done to maximize the beam signal relative to the background. The repeller grid was biased to $-100$ V using a power supply, while the discriminator was swept from $-80$ V to 80 V in 1000 steps. The collector was kept at $-9$ V using a battery. At each step the collector current was measured across a 100 kΩ resistor and digitized with a 16-bit DAQ from National Instruments. The grid configuration used with the ceramic RFEA is illustrated in figure 3.14a.

### Brass RFEA

For the radial measurements at UiT we used an RFEA with a grounded brass housing with a cylindrical shape, a diameter of 16 mm and a thickness of 10 mm. The probe has four grids, three of stainless steel mesh with a transmission factor of 44%, and the fourth, the repeller grid was made of a nickel mesh with transparency of 67%. The meshes are spotwelded to 0.3 mm thick brass spacers with 0.3 mm ceramic spacers in between, resulting in a distance of 0.6 mm between the grids. The front grid was electrically connected to the housing and thereby grounded. The front aperture was 2 mm. The ceramic spacer in front of the collector limited the collector

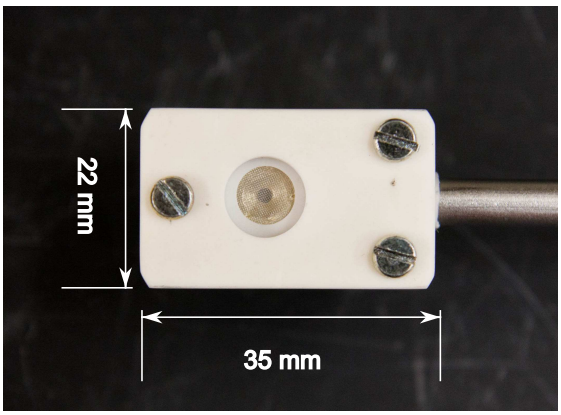


**Figure 3.15:** Dimensions of the ceramic RFEA

area to 3 mm diameter. The repeller grid was biased to −86 V using a power supply, while the discriminator was swept from −10 V to 120 V in 1000 steps using an amplifier and a series of batteries. A secondary repeller biased to −20 V using a power supply was used to keep secondary electrons from leaving the collector. The collector was kept at −9 V using a battery. At each step, the collector current was measured across a 100 kΩ resistor and digitized with a 16-bit DAQ from National Instruments. The grid configuration of the brass RFEA is illustrated in figure 3.14b.

#### Axial RFEA

For the axial measurements at UiT we used an RFEA (figure 3.14c) with a grounded brass housing mounted so it always faced the source. The housing was cylindrical with a diameter of 13 mm and length of 25 mm. This RFEA had four grids of stainless steel with a transmission factor of 44%, each spotwelded to a 0.5 mm thick brass spacer. The front aperture opening was 1 mm. Between each grid there was a 0.25 mm thick spacer so that the total distance between the grids was 0.75 mm. The spacers had an inner diameter of 10 mm which limited the collector area. When using the same grid configuration as the radial brass RFEA, this probe produced a large amount of noise in the current signals. We therefore chose to use this probe with the discriminator grid in front of the repeller grid (figure 3.14c), as further described in 3.3.3. This configuration produced slightly sharper distributions and less noise. This type of configuration with discriminator in front of the repeller has earlier been used successfully by Gahan et. al. [60]. Except for these differences this probe was used with exactly the same parameters as the radial brass RFEA; the repeller biased to −86 V, discriminator was swept from −10 V to 120 V, and the collector was kept at −9 V. At each step the collector current was measured across a 100kΩ resistor and digitized with a 16-bit DAQ from National Instruments.

### 3.3.3 Comparing grid configurations

The ceramic RFEA was made so that the grid configuration easily could be changed. Some tests were made using a floating front grid instead of a grounded and on effects by interchanging the repeller and discriminator grid. The result of these test can bee seen for HELIX-LEIA in figure 3.16 and for Njord in figure 3.17.

Our first idea was that a floating front grid would be disturbing the plasma less than a grounded front. However, we observed that in HELIX-LEIA a front grid charges up negatively when it is kept floating, often much more negatively than the floating potential measured with a Langmuir probe. The effect was less apparent in Njord. This indicates that a floating front grid might be collecting electrons, charge up negatively and thereby alter the sheath in front of the probe. The result of this is seen in HELIX-LEIA as an increased ion saturation current in comparison with the grounded front grid. This effect seems to affect only the amount of background plasma that is gathered. The ion beam flux seems to be unaffected by this change. Since we want to measure the ion beam and since the charging of the front grid was a bit unpredictable we chose to do all

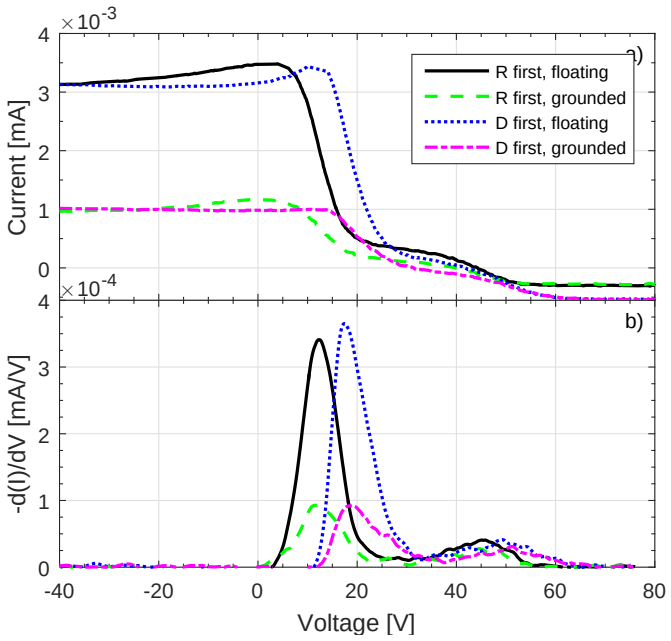


**Figure 3.16:** RFEA measurements in HELIX-LEIA comparing different grid configurations of the ceramic RFEA probe with 900 G in source and 0 G in the expansion chamber. RF frequency was $9.5$ MHz. RF power 650 W, flow 1.7 sccm, pressure in source: $1.9 \cdot 10^{-4}$ Torr and $5.6 \cdot 10^{-5}$ Torr in expansion chamber. The front grid was floating at $-28$ V.

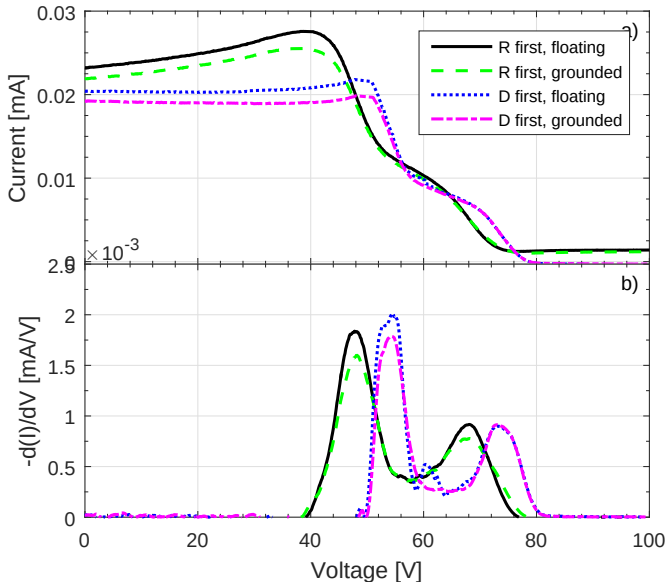


**Figure 3.17:** RFEA measurements in NJORD, comparing different grid configurations of the ceramic RFEA probe, with 2.0 sccm flow and 5-6-5 A magnetic field. The front grid was floating at $-2.5$ V.

our measurements with a grounded front grid.

The second observation was that by interchanging the repeller and discriminator grid the whole distribution shifts slightly to higher collector voltages by around 6 V in both Njord and HELIX-LEIA, but the shape of the distribution remains the same. This shift in voltage might be due to a change in the sheath voltage when the grids are interchanged.

We have used this configuration with the discriminator in front of the repeller for the Axial RFEA in Njord. This is because this probe gave very noisy measurements with the repeller in front of the discriminator. By interchanging the grid biases the measurement characteristics became much less noisy.

### 3.3.4 RFEA measurements of high energy electrons

To understand the underlying physics of characteristic parameters of current-free double layers (CFDLs) it is important to obtain information about the electrons and their energy distribution associated with a DL. For example, Takahashi et al.[79] observed, in a similar experiment, high-energy electrons at a magnetic field line mapping to the edge of the source in electron energy distribution (EEDF) obtained by a Langmuir probe. Gahan et. al. [60, 65] has shown that by inverting grid biases on an RFEA, one could obtain information on the electron distribution of energetic electrons.

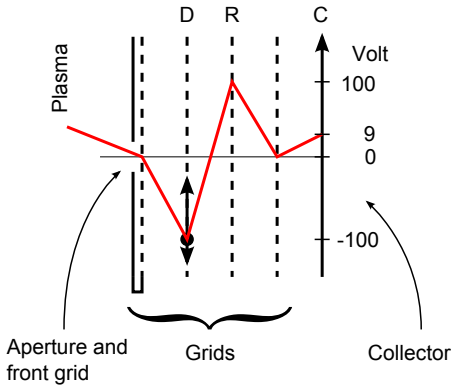


**Figure 3.18:** RFEA grid configurations for electron measurements

We have used the brass RFEA and biased the grids according to Gahan et. al. [60]. The grid configuration for electron measurements is shown in figure 3.18, where D is the discriminator grid and is scanned from 0 to $-120$ V, R is the repeller grid biased at $+100$ V and C is the collector kept at $+9$ V. The innermost grid is not needed in this configuration and is therefore grounded.

Figure 3.19a shows a logarithmic plot of collector vs. discriminator voltage from the electron-RFEA at $r = -7$ cm. Only the electrons with energies high enough to overcome the sheath potential in front of the probe will be recorded, so that the RFEA detects only the high-energy

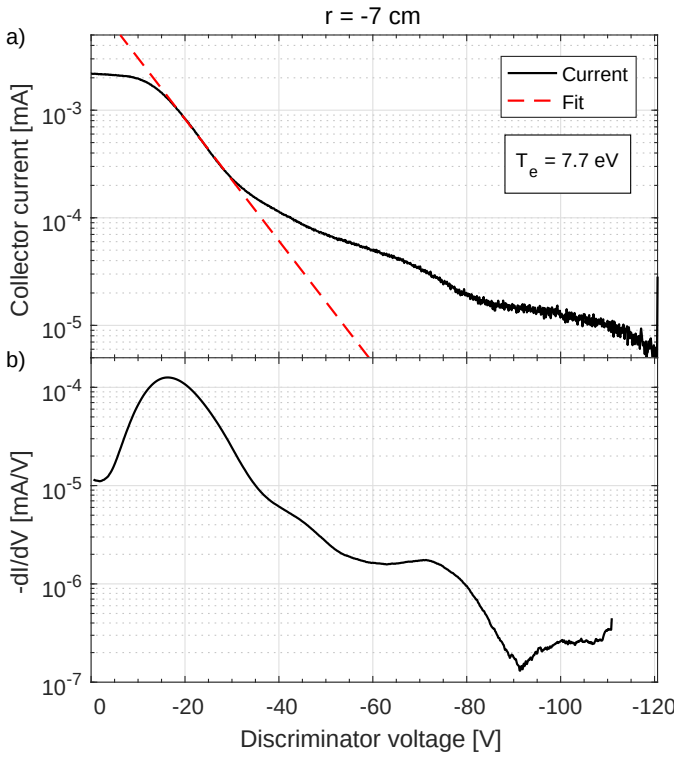


**Figure 3.19:** An electron-RFEA measurement form $p = -7$ in Njord with $2.0$ sccm flow. a) The collector current, b) the derivative of the collector current.

tail of the EEDF [80]. The electron temperature is extracted as a linear fit to this plot as [64]:

$$\frac{\mathrm{d}\big(\ln(I)\big)}{\mathrm{d}V} = \frac{e}{kT_e} \tag{3.20}$$

Figure 3.19b shows a logarithmic plot of the derivative of the collector current with regard to discriminator voltage. This derivative is proportional to the EEDF for energies high enough to enter the probe [65], which in this case is above the peak around 20 V.

## 3.4 Laser Induced Fluorescence (LIF)

Laser Induced Fluorescence (LIF) is a spectroscopic technique that can be used to measure particle velocity distribution. A laser is used to excite neutral atoms or ions. Then the Doppler broadening and shift of either the emission or the absorption line is measured, from which the velocity distribution can be deduced.

Stern and Johnson [81] were the first to perform LIF in plasma, using a single frequency argon laser. They used spectroctroscopy to measure the Doppler broadening and shift of a resonant emission line to deduce local ion densities and velocities. Hill et al. [82] were the first to use non-resonant (Metastable) transitions and scanning of the laser wavelength. They measured the absorption line shape such that velocity resolution was determined by the natural linewidth of the atomic transition only, thus increasing the possible resolution, instead of measuring the emission line shape, which is limited by the resolution of the spectrometer used for detection. This is the most common technique today and also the method we used in our measurements.

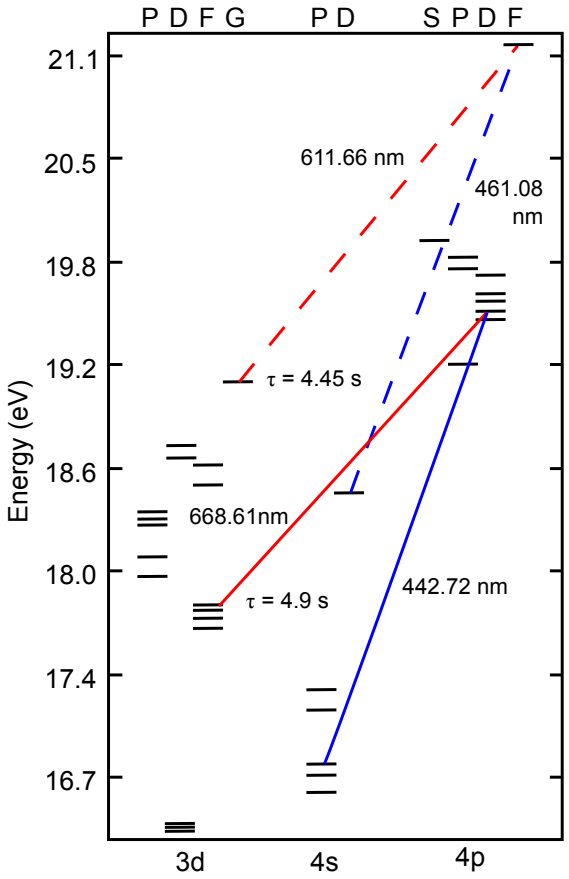


**Figure 3.20:** Energy diagram for ionized argon showing the metastable transitions used at UiT (solid) and WVU (dashed). (Adapted from Severn et. al. [37])

In a plasma there are a number of ions excited into a long-lived, so called metastable, states. If such a metastable ion is excited further by absorbing photons of the right energy, it will be

excited to an even higher but shorter-lived energy state. It will then immediately de-excitate back to its ground state by emitting a photon. (Figure 3.20)

The individual ion would experience a Doppler-shifted laser light dependent on their velocity. Only when this Doppler-shifted light is matching a natural absorption line would the metastable ion be further excited and then de-excite to emit a photon. This would give rise to a Doppler-broadening and shift of the absorption line due to the thermal movement of the ions and the flow in the plasma.

A single mode tunable laser is used to pump the metastable ions, which then decay, by photon emission. The laser is scanned through a range of frequencies while the intensity of the fluorescence line is measured. The resulting curve of fluorescence intensities can be interpreted as the velocity distribution of the metastable ions. The frequency is converted to velocity using the expression (assuming $\lambda_0 \Delta\nu \ll c$):

$$v = \lambda_0 \Delta\nu \tag{3.21}$$

where $v$ is the ion velocity, $\lambda_0$ is the excitation wavelength of the metastable at rest and $\Delta\nu$ is the frequency difference between the excitation frequency at rest and the actual excitation frequency.

The advantage of Laser Induced Fluorescence (LIF) diagnostics is that it is not intrusive [37], unlike the rather large RFEA probes. It provides direct measurements of the velocity distribution of metastable ions, which is interpreted as a representation of the velocity distribution of the entire ion population [38].

Dye Lasers has been most commonly used for LIF due to their high power and the possibility to tune them over a broad frequency range. Currently, the availability of tunable diode lasers with more than 10 mW effective power has made LIF-diagnostics more feasible. LIF diagnostics using tunable diode lasers was first implemented by Severn et al. [37].

Low-power LIF using tunable diode lasers was later implemented at West Virginia University (WVU) [39] and was soon afterward applied in studies of flow [40]. These measurements were followed by LIF investigations of beam plasmas at Princeton Plasma Physics Laboratory (PPPL) [16] and Australian National University (ANU) [17, 26].

### 3.4.1 UiT LIF-system

The UiT LIF system is set up as shown in figure 3.21. It consists of a Toptica DL Pro tunable single-mode-diode laser with a nominal wavelength of 668 nm and typical output power of 22 mW. 10% of the beam is split off by a beam splitter in to a Bristol Instruments 621-VIS wavelength meter, while the remaining light is modulated by a 1 kHz mechanical chopper and then fed via two mirrors into the plasma source along the $z$-axis, through a quartz window (figure 3.22 and 3.23).

The laser is tuned to 668.6138 nm to pump the argon ions in the $3d^4F_{7/2}$ metastable state (with a lifetime of $\tau = 4.9$ s [83]) to the $4s^4P_{2/3}$ state which then decays to the $4s^4P_{3/2}$ state

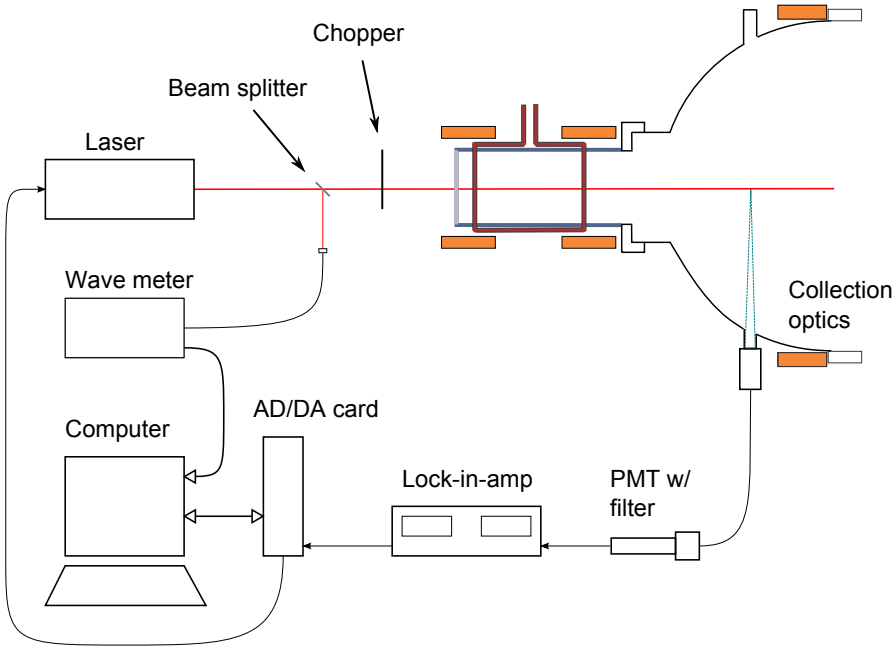


**Figure 3.21:** The LIF setup at UiT.

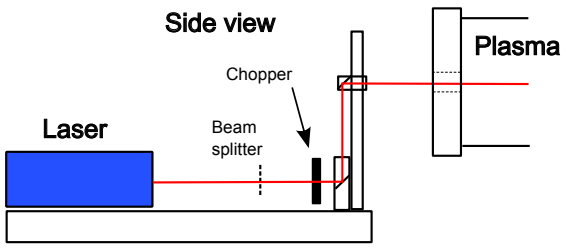


**Figure 3.22:** Laser injection at Njord. The laser light first goes through a beam splitter where 10% is split off for the wavelengthmeter. The remaining light goes through a chopper and two mirrors before it enters the plasma chamber through a quartz window.

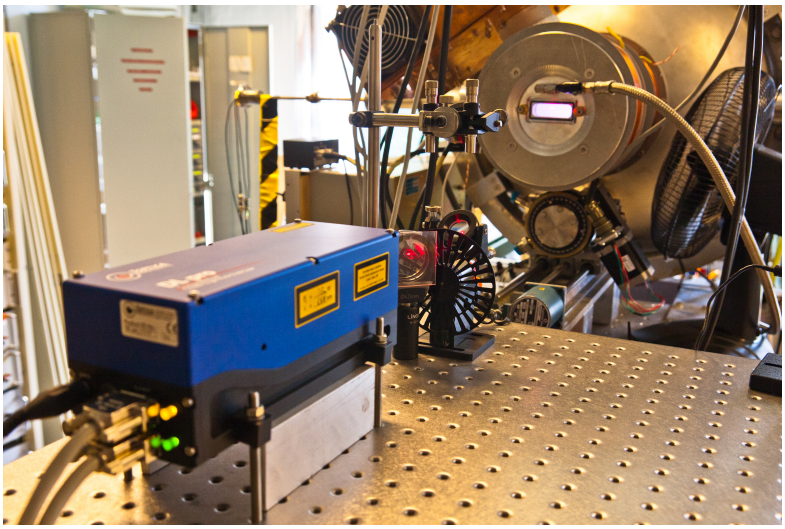

**Figure 3.23:** Photo of the UiT laser system.

by emitting 442.7244 nm photons, as shown in figure 3.20 [26].

The collection optics is mounted at a window port located at $z = 55$ cm (figure 2.2) and is pointing perpendicularly to the laser beam. The optics consists of two plane-convex lenses with focal lengths of $f_1 = 125$ mm and $f_2 = 400$ mm mounted in a 152 mm long lens tube with an optical fiber connected through an end cap (figure 3.24). The lense tube is mounted on a adjustable carrier so that the viewing dirrection can be adjusted. This carrier is again mounted at a 65 mm long, 38 mm inner diameter, steel tube that is bolted to the Conflat window and flanges of the vacuum chamber. This tube acts as an aperture for the optical system making the efficient front optics diameter 38 mm. The optical system has a combined focal length of $f = 108$ mm and is set up so that the (paraxial) focus point is a little bit past the the laser beam in the center of the chamber. The optical fiber would view an area of the laser beam less than 5 mm in diameter making it for all practical purposes a measurement of a single point.

The optical fiber brings the light from the collection optics to a Hamamatsu photo multiplier (PMT) with a 442 nm, 1 nm bandwidth interference filter in front. The signal from the photomultiplier is then fed into a EG&G Instruments 7265 lock-in amplifier using a time constant of 20 s for the filters. In these experiments the laser was stepped through 61 different wavelengths. At each step the wavelength was kept constant for 100 s to let the signal from the lock-in amplifier stabilize. It was then sampled by a 16-bit DAQ from National Instruments while the corresponding wavelength was recorded by the wavelength meter. The signal and the wavelength were then stored in the computer system. The stepping of the laser and the recording of the data was controlled by a LabView program.

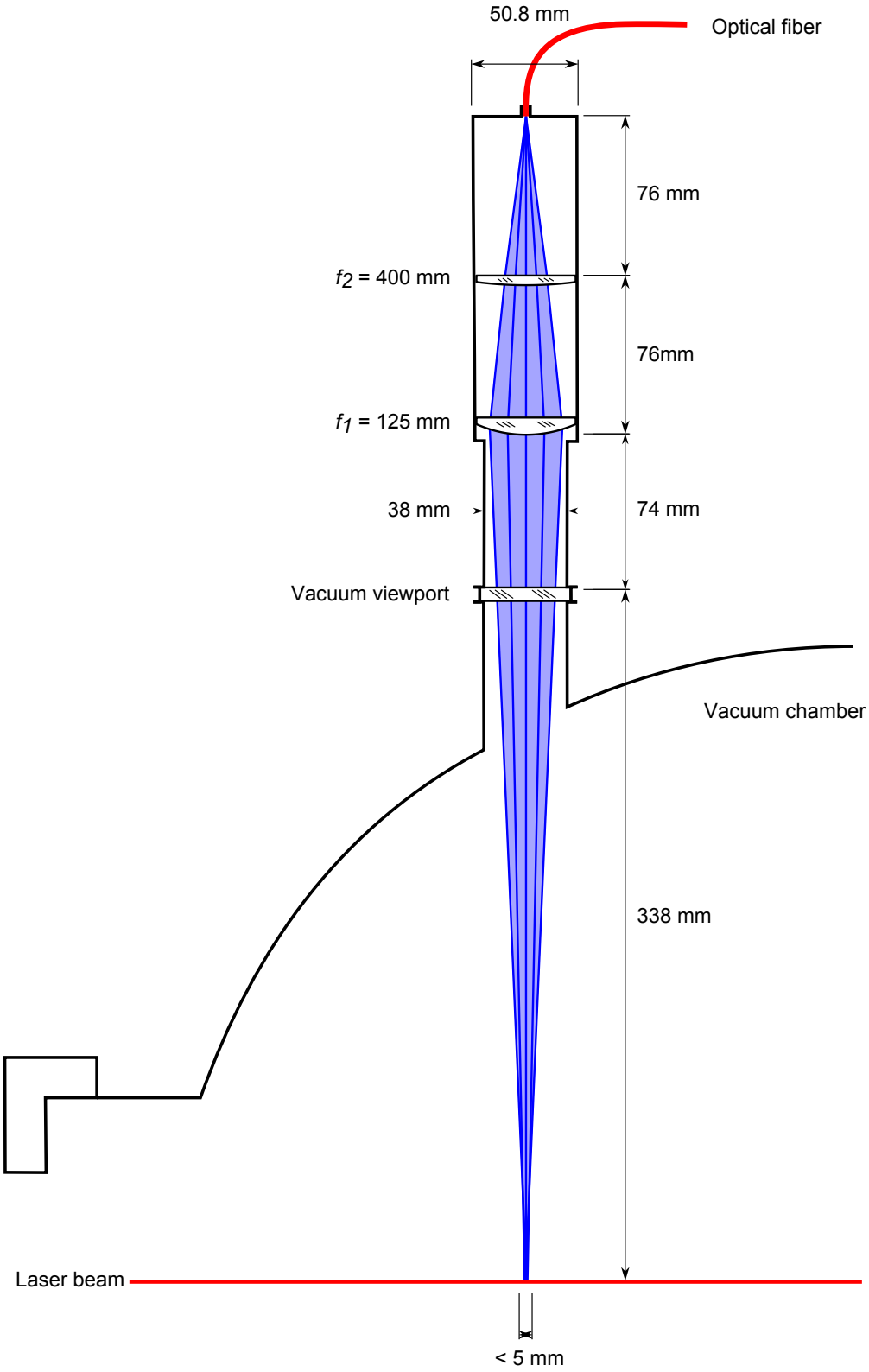


**Figure 3.24:** Collection optics used at Njord. The blue lines represent a realistic ray tracing of the area viewed by the optical fibre for 442.72 nm light.

### 3.4.2 WVU HELIX-LEIA LIF system

The HELIX-LEIA LIF system consists of a 10 W Spectra-Physics Millennium Pro diode laser pumping a Sirah Matisse-DR tunable ring dye laser (figure 3.25) running rhodamin-6G dye [84] . Typical output power is around 800 mW. The laser is tuned to 611.6616 nm (vacuum wavelength) to pump the Ar-II $3d^2G_{9/2}$ metastable state (with a lifetime of $\tau = 4.45$ s [83]) to the $4p^2F_{7/2}$ which then decays to the $4s^2D_{5/2}$ state by emitting 461.086 nm photons, as shown in figure 3.20 (dashed line). About 10% of the laser beam is split off by a beam splitter to a Bristol Instruments 621-VIS wavelength meter while the rest is modulated with a 1 kHz mechanical chopper and injected into the HELIX source through a fiber.

The emission is collected with a movable reentrant glass probe in the expansion chamber (figure 2.6) [85]. The probe is kept at approximately 2 cm radial distance from the laser beam. The light from the probe is fed through an optical fiber to a filtered (1 nm bandwidth at 461 nm) Hamamatsu photomultiplier tube. The signal is then fed to a Stanford Research SR830 lock-in amplifier using a time constant of 10 s to remove the background emissions. The laser was stepped through 128 different wavelengths in a total range of 20 – 30 GHz (12 – 15 km/s) and the signal from the lock-in amplifier was sampled after it had stabilized for 10 s. The filtered signal was then recorded with a computer together with the wavelength from the wavelength meter. An example of LIF measurements can bee seen in figure 3.26, where the solid line is a LIF measurement from close to the the source in the middle of the stainless steal chamber of HELIX at $z = -45$ cm. The dashed line is a LIF measurement from the expansion chamber LEIA at $z = 32$ cm showing a beam around 11 km/s and background plasma. A comparison of the LIF systems at UiT and WVU is found in table 3.1.

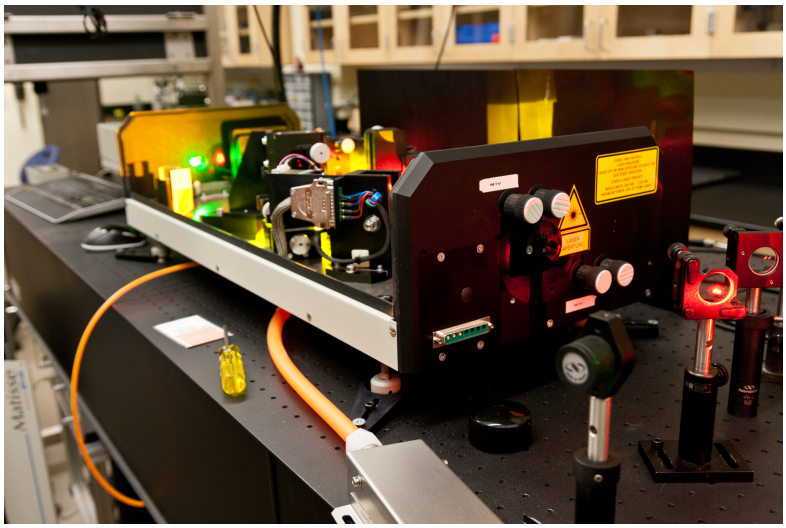

**Figure 3.25:** Photo of the WVU laser system.

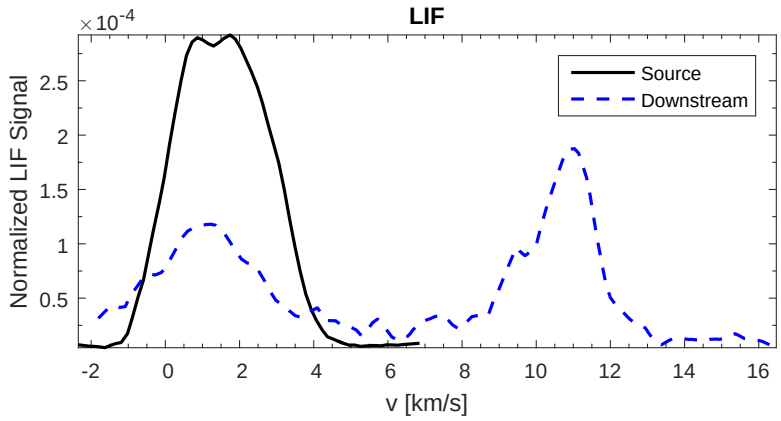


**Figure 3.26:** Example of LIF measurements from HELIX-LEIA. In the source HELIX at $z = -39$ cm (solid line) and in the expansion chamber LEIA at $z = 32$ cm (dashed line). RF frequency: 9.5 MHz. RF power: 650 W. Flow: 3.0 sccm

**Table 3.1:** Comparing LIF parameters

| | WVU LIF | UIT LIF |
|---|---|---|
| Laser: | Sirah Matisse-DR | Toptica DL pro |
| Nominal wavelength: | 611.66 nm | 668 nm |
| Output power: | 800 mW | 22 mW |
| Chopper: | 1 kHz mechanical | 1 kHz mechanical |
| Collection filter: | 461 nm | 442 nm |
| Lock-In time constant: | 10 s | 20 s |
| Sample periode: | 10 s | 100 s |

### 3.4.3 Zeeman broadening

There are other broadening mechanisms than Doppler broadening that can contribute to the width of an absorption line, such as Stark broadening, power broadening and Zeeman broadening. All of these give much smaller contributions than the Doppler broadening. [86] Of these mechanisms the Zeeman broadening is the most significant, and then only in the source of HELIX where the magnetic field is strong enough. Assuming a magnetic field of 1 kGauss the Zeeman broadening would contribute with about $2.6 \cdot 10^{-4}$ nm [86, 87] witch corresponds to about 100 m/s wich is barely detectable in our measurements. Since most of our measurements is done in much weaker magnetic fields, we conclude that the Zeeman Broadening can be ignored in our measurements and that Doppler broadening is the dominant mechanism.

# Chapter 4

# Plasma background measurements

This section presents background measurements of the plasma parameter in Njord and HELIX-LEIA. In these measurements $z$ is in the axial direction pointing from the source and into the expansion chamber. For radial measurements the coordinate $r$ is used. This could be either the $x$-coordinate or the $y$-coordinate depending on the setup. Positive values of $r$ means that the measurement is done in a radial position on the same side of the center line as the port for the probe feedtrough. Negative values of $r$ indicates that the measurement is done on the opposite side of the center line with the probe shaft crossing the center of the plasma. Since the probe shaft is grounded this last configuration might alter the plasma slightly, but measuring across the center line might also reveal asymmetries in the plasma.

## 4.1 Emissive probe measurements

Emmissive probe measurements were conducted to map out the plasma potential in Njord for different magnetic field configurations and pressures. The different magnetic field configurations used are described in section 2.1.1 and can be seen in figure 2.3. The different pressures and flows are listed in table 4.1.

**Table 4.1:** Pressure for different flows in Njord

| Flow [sccm] | Pressure [mTorr] | Pressure [mPa] |
|---|---|---|
| 1.1 | $0.21 \pm 0.02$ | $27 \pm 2$ |
| 1.5 | $0.28 \pm 0.03$ | $37 \pm 3$ |
| 2.0 | $0.34 \pm 0.02$ | $46 \pm 3$ |

Figure 4.1 shows radial profiles of the plasma potential measured at $z = 55$ cm with the emissive probe for different downstream magnetic fields. The plasma potential is seen to increase with increasing downstream magnetic field. Especially for 5 and 10 A in the third coil the plasma potential shows two distinct peaks around $r = \pm 7$ cm with a slightly lower potential in the middle. At higher magnetic fields downstream the plasma potential develops towards a single

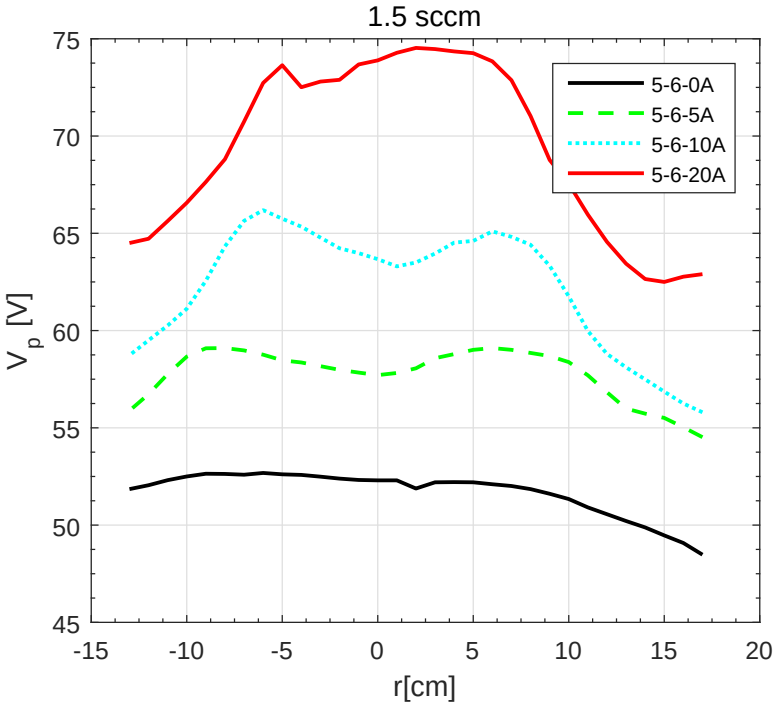


**Figure 4.1:** Radial profiles of plasma potential from emissive probe for different downstream magnetic fields. Flow 1.5 sccm, Pressure 0.28 mTorr, RF-Power 1000 W

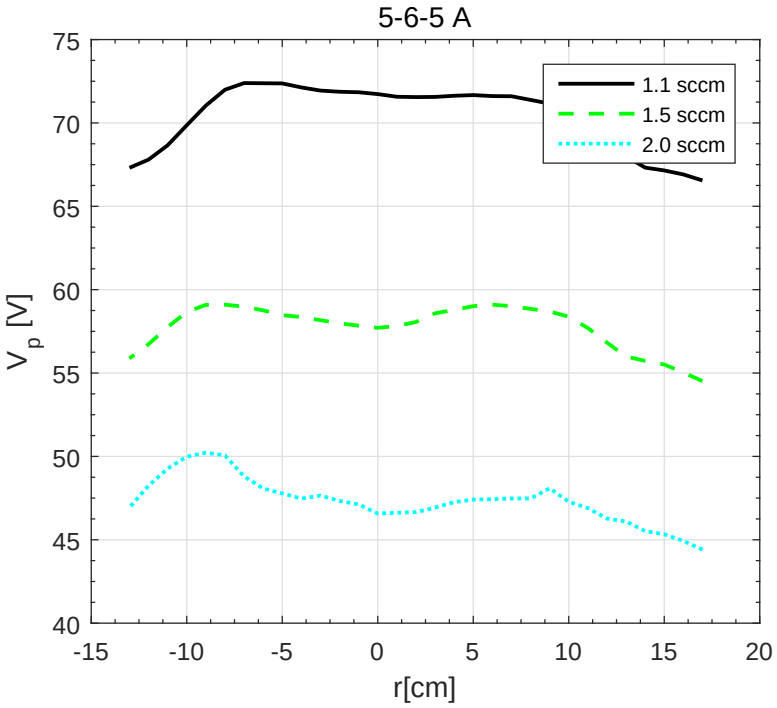


**Figure 4.2:** Radial profiles of plasma potential from emissive probe for different pressures. Magnetic field 5-6-5 A, RF-Power 1000 W

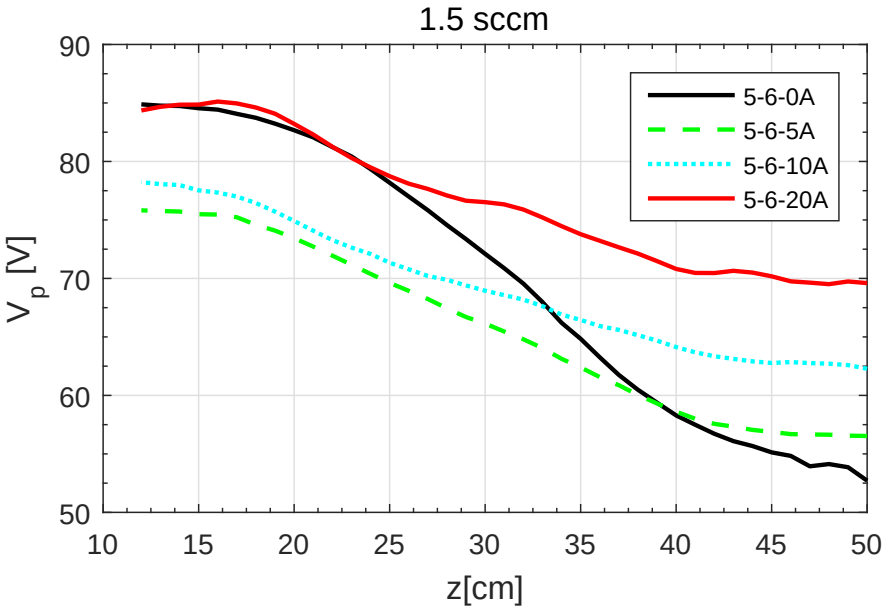


**Figure 4.3:** Axial profiles of plasma potential from emissive probe for different downstream magnetic fields. Flow 1.5 sccm, Pressure 0.28 mTorr, RF-Power 1000 W

peak. The configration 5-6-0 A is different from the other magnetic field configurations in that the potential stays almost flat in the entire central part of the plasma.

In figure 4.2 the radial profiles of plasma potential for different pressures for the 5-6-5 A magnetic field configuration are plotted. We see that the plasma potential decreases with increasing pressure. The double peak feature is present at all three pressures.

Since the axial probe feedthrough only can be moved 22 cm in axial direction, two different lengths of probes were used for the axial emissive probe measurements to cover both the source and the expansion chamber. The measurements from the two probes were merged to create one axial profile.

Figure 4.3 shows the axial profiles of the plasma potential for 1.5 sccm. We have a relatively high potential in the source, possibly due to loss of electrons to the grounded back wall. Already inside the source the potential drops as we moves towards the expansion chamber. The potential drop continues until around $z = 40$ cm where the gradient decreases. Increasing the downstream magnetic field results in increased plasma potential downstream. The same trend is also seen in the source except for the magnetic field configuration 5-6-0 A, where the potential is very high in the source and low in the expansion chamber providing the largest potential drop between source and chamber. One explanation for this might be that in the 5-6-0 A configuration more electrons are lost to the walls at the port between the source and the expansion chamber because of the field line connected to the source (Se the discussion on magnetic field configuration in section 2.1.1).

Figure 4.4 shows the axial profiles of plasma potential for the 5-6-5 A magnetic field configuration at different pressures. We see that the plasma potential decreases with increasing pressure

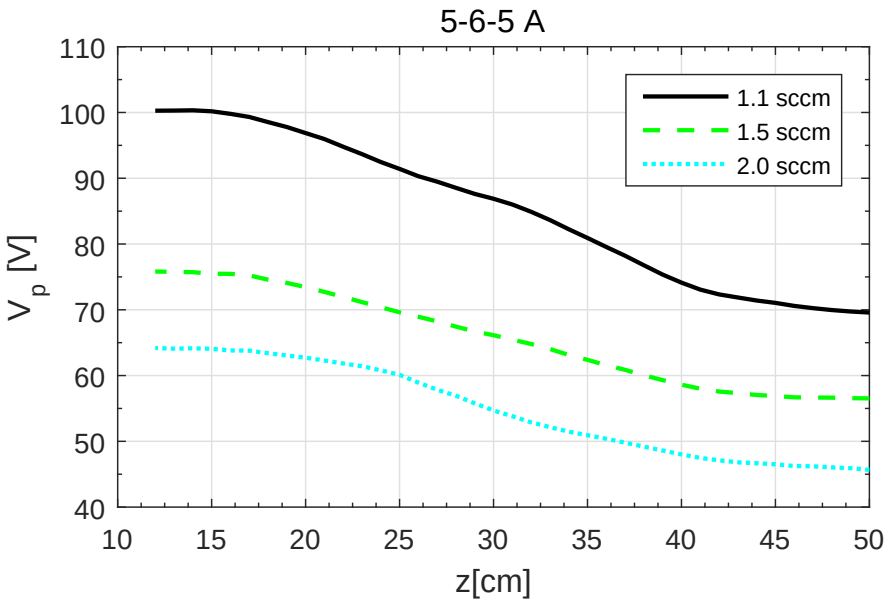


**Figure 4.4:** Axial profiles of plasma potential from emissive probe for different pressures. Magnetic field 5-6-5 A, RF-Power 1000 W

both in the source and in the expansion chamber. Except for the difference in potential the profiles are behaving similarly for all three pressures. One thing to notice is that the potential difference between the source and the expansion chamber is seen to increase with decreasing pressure. The values for the plasma potentials in the source and the expansion chamber and their difference based on the measurements in figure 4.4 are given in table 4.2. The potential difference is quite close to the beam energies measured in paper 4 [67] both with RFEA and LIF for the same pressures.

**Table 4.2:** Plasma potential difference in Njord

| Flow [sccm] | Pressure [mTorr] | $V_p$ (source) [V] | $V_p$ (downstream) [V] | $\Delta V_p$ [V] |
|---|---|---|---|---|
| 1.1 | 0.21 | 100 | 70 | 30 |
| 1.5 | 0.28 | 76 | 57 | 19 |
| 2.0 | 0.34 | 64 | 46 | 18 |

## 4.2 Langmuir probe measurements

For the axial Langmuir probe measurements we only used one compensated Langmuir probe. We were thus limited by the probe feedthrough and could therefore only measure in the expansion chamber and the part of the source closest to the junction.

Figure 4.5 shows the axial profile of the plasma density measured with the Langmuir probe for a gas flow of 1.5 sccm and two different downstream magnetic fields. The main characteristic

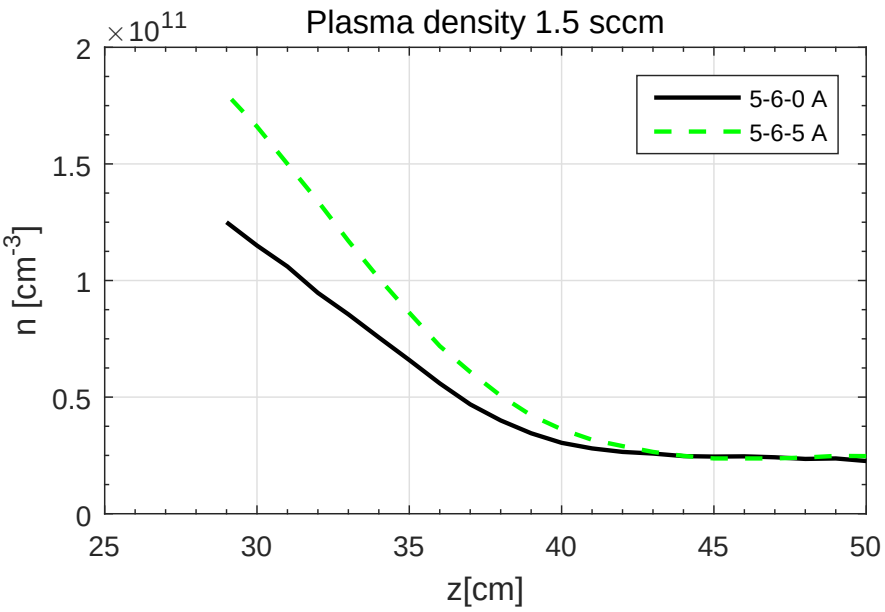


**Figure 4.5:** Axial profiles of plasma density from Langmuir probe for different downstream magnetic fields. Flow 1.5 sccm, Pressure 0.28 mTorr, RF-Power 1000 W

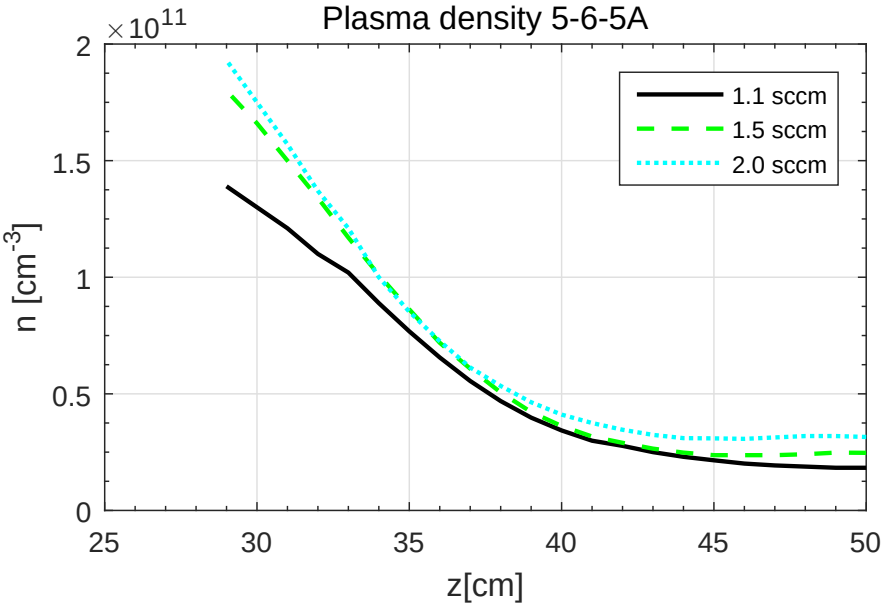


**Figure 4.6:** Axial profiles of plasma density from Langmuir probe for different pressures. Magnetic field 5-6-5 A, RF-Power 1000 W

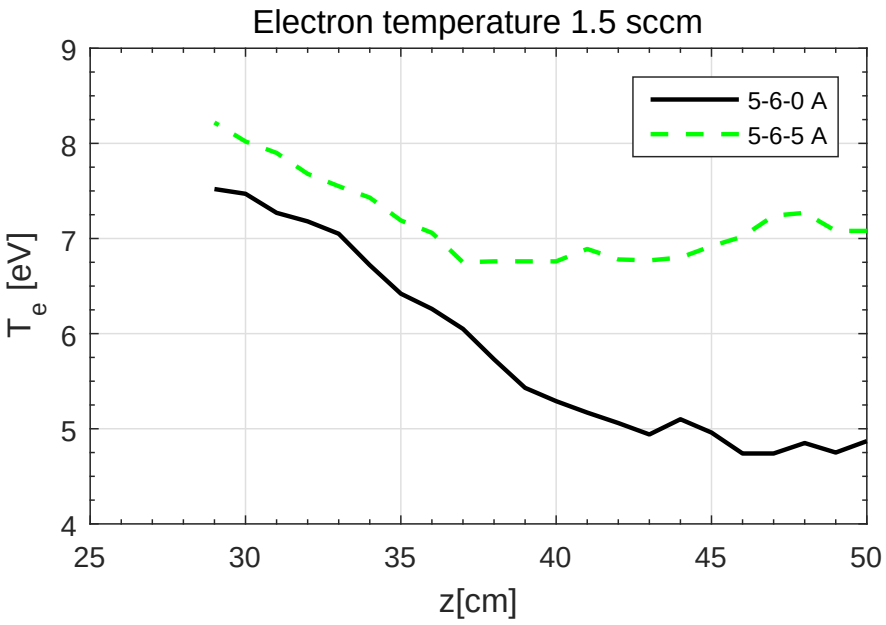


**Figure 4.7:** Axial profiles of electron temperature from Langmuir probe for different downstream magnetic fields. Flow 1.5 sccm, Pressure 0.28 mTorr, RF-Power 1000 W

of the profiles is that the density decreases away from the source and then stabilizes at a fairly constant level after around $z = 40$ cm. We can also see that the 5-6-5 A configuration gives a higher density in the source than the 5-6-0 A configuration, while the downstream density is almost similar for both.

In figure 4.6 the density profiles for different pressures using the 5-6-5 A magnetic field configuration is shown. Here we see that the source density increases with the pressure (or gas flow) while the downstream density is only marginally affected by the pressure.

Figure 4.7 show the electron temperature deduced from the Langmuir probe measurements for a gas flow of 1.5 sccm for two different downstream magnetic fields. The 5-6-5 A magnetic field configuration results in an overall higher electron temperature. This is especially pronounced downstream in the expansion chamber where the temperature first stabilizes and then increases as we move away from the source.

Figure 4.8 shows the electron temperature for three different pressures with the 5-6-5 A magnetic field configuration. The electron temperature is seen to increase with decreasing pressure. In addition all of the profiles has a minimum in the electron temperature somewhere after the beginning of the expansion chamber.

Figure 4.9 shows the electron temperature for the same pressures as in figure 4.8 only with no current in the third coil (5-6-0 A). The electron temperature is here seen to decrease away from the source with no distinct minima.

Figure 4.10 shows the axial profile of the floating potential measured with the Langmuir probe for a gas flow of 1.5 sccm. With the 5-6-0 A magnetic field configuration the floating

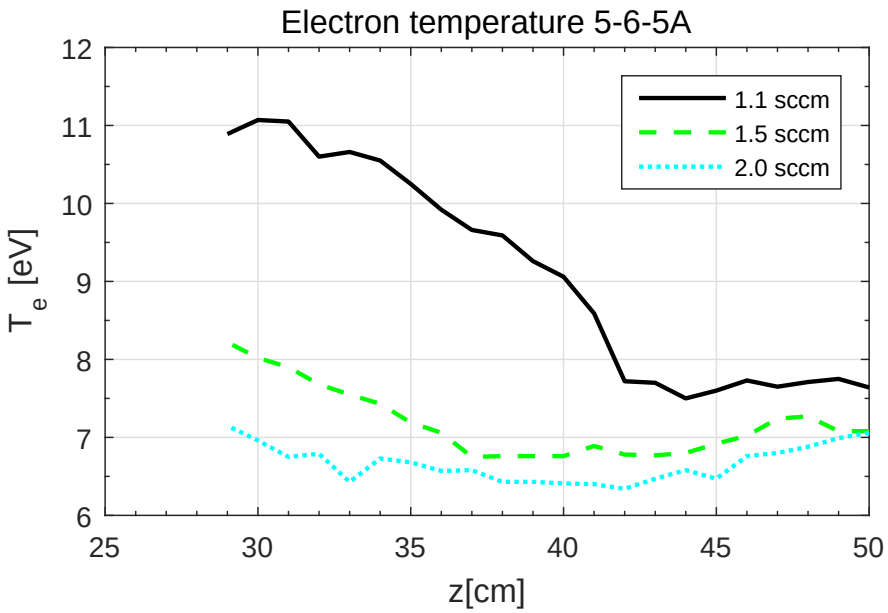


**Figure 4.8:** Axial profiles of electron temperature from Langmuir probe for different pressures. Magnetic field 5-6-5 A, RF-Power 1000 W

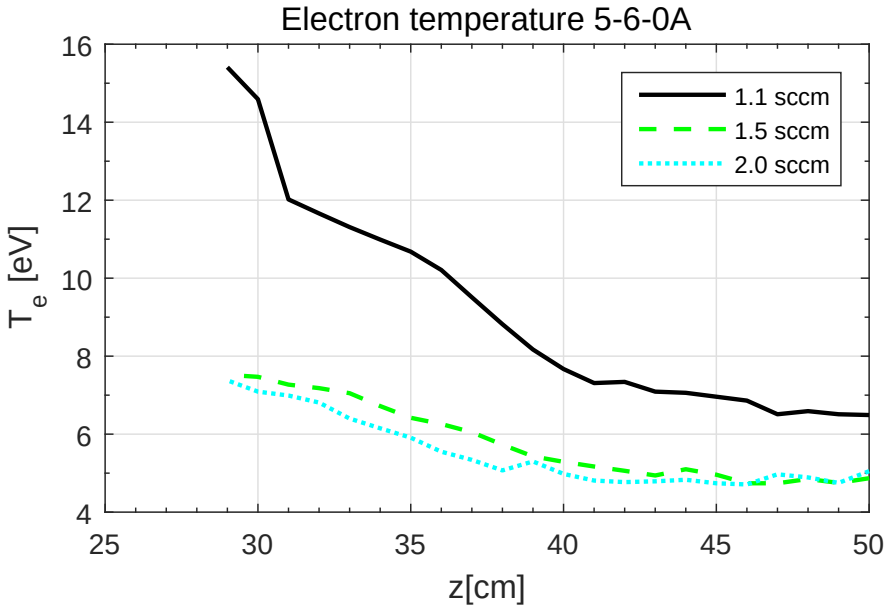


**Figure 4.9:** Axial profiles of electron temperature from Langmuir probe for different pressures. Magnetic field 5-6-0 A, RF-Power 1000 W

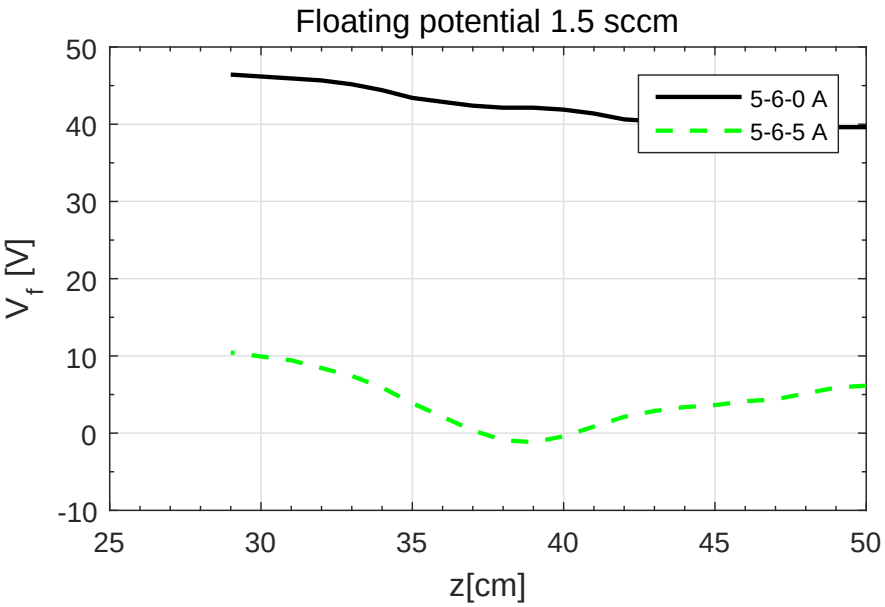


**Figure 4.10:** Radial profiles of floating potential from Langmuir probe for different downstream magnetic fields. Flow 1.5 sccm, Pressure 0.28 mTorr, RF-Power 1000 W

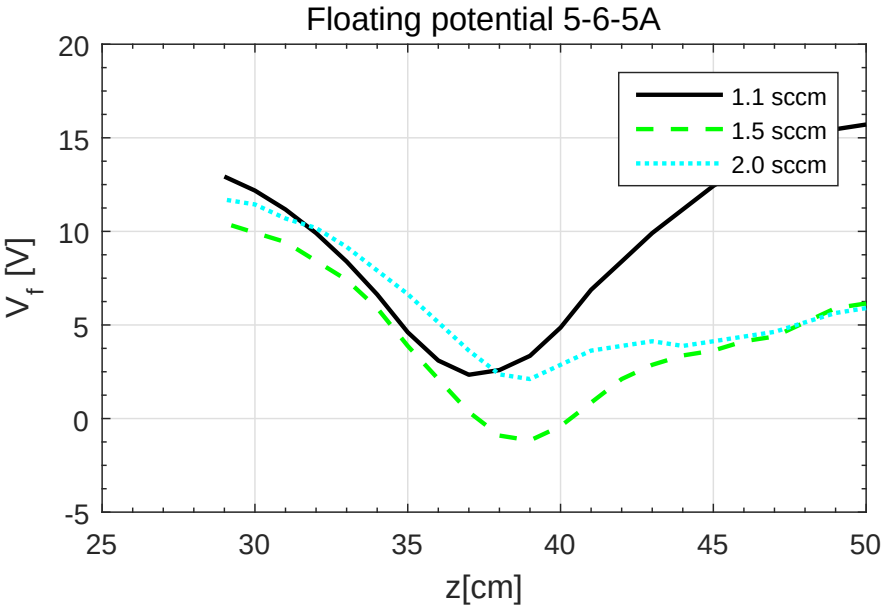


**Figure 4.11:** Axial profiles of floating potential from Langmuir probe for different pressures. Magnetic field 5-6-5 A, RF-Power 1000 W

potential is fairly high and is decreasing steadily away from the source. In the 5-6-5 magnetic field configuration the floating potential has a very distinct minimum around $z = 38$ cm. This minimum can be seen for all the three pressures as can be seen in figure 4.11.

## 4.3 RFEA measurements in Njord

Figure 4.12 shows axial profiles of the RFEA measurements (IDF) from Njord for three different pressures, all with the magnetic field configuration 5-6-0 A (no current in the third coil). A gray line marks the plasma potential as measured with the emissive probe. A white line marks the maximum peak of the main distributions measured with the RFEA, and a red line marks the peak of an ion beam where a peak is detectable. A broad distribution is emerging from the source. Around $z = 40$ – 50 cm this distribution starts to disappear and a much narrower background distribution grows up from around $z = 45$ cm, probably due to charge exchange collisions. The remains of the source distribution is seen as a high energy tail or a weak ion beam continuing into the expansion chamber. For the 1.1 sccm we see only a weak high energy tail, for 1.5 sccm there is sometimes an indication of a beam peak and at 2.0 sccm we can clearly see a beam peak from $z = 39$ cm and until 54 cm. The plasma potential from the emissive probe is seen to follow with the lower energy part of the distribution and it corresponds well with the peak of the background distribution downstream. The only exception is for 2.0 sccm where the plasma potential from the emissive probe is higher than indicated from the background distribution.

Figure 4.13 shows axial profiles of the RFEA measurements from Njord for three different pressures with the magnetic field configuration 5-6-5 A. As with figure 4.12 the gray line marks the plasma potential as measured with the emissive probe. A white line marks the maximum peak of the main distributions measured with the RFEA, and a red line marks the peak of the beam. A very wide distribution is emerging from the source. At around $z = 40$ cm the lower energy part of the distribution disappears gradually until only a single ion beam is left. At the same time a new background distribution grows up to a higher density than the beam. All the three pressures used give clear beam signatures from around $z = 40$ – 45 cm and continue as far back as we have measured. The voltage of the IDF from a grounded RFEA can be taken as a crude approximation of the sum of kinetic and potential energy of the ions, indicating at which plasma potential the ions were created. We can see that the beam is a continuation of the source distribution and that the beam voltage $V_b$ is approximately the same as the plasma potential in the source. The plasma potential from the emissive probe is seen to lie a little bit higher than the peak of the background distribution in the expansion chamber. We speculate that maybe the ion beam can push the potential of the emissive probe higher, resulting in an overestimation of the background plasma potential.

Figure 4.14 shows a collection of radial RFEA profiles at different pressures and magnetic field configurations. For the 5-6-5 A configuration (a,c,e) a beam is clearly visible at all pressures. The main effect of the pressure seems to be the decrease of beam energy (velocity) with increasing

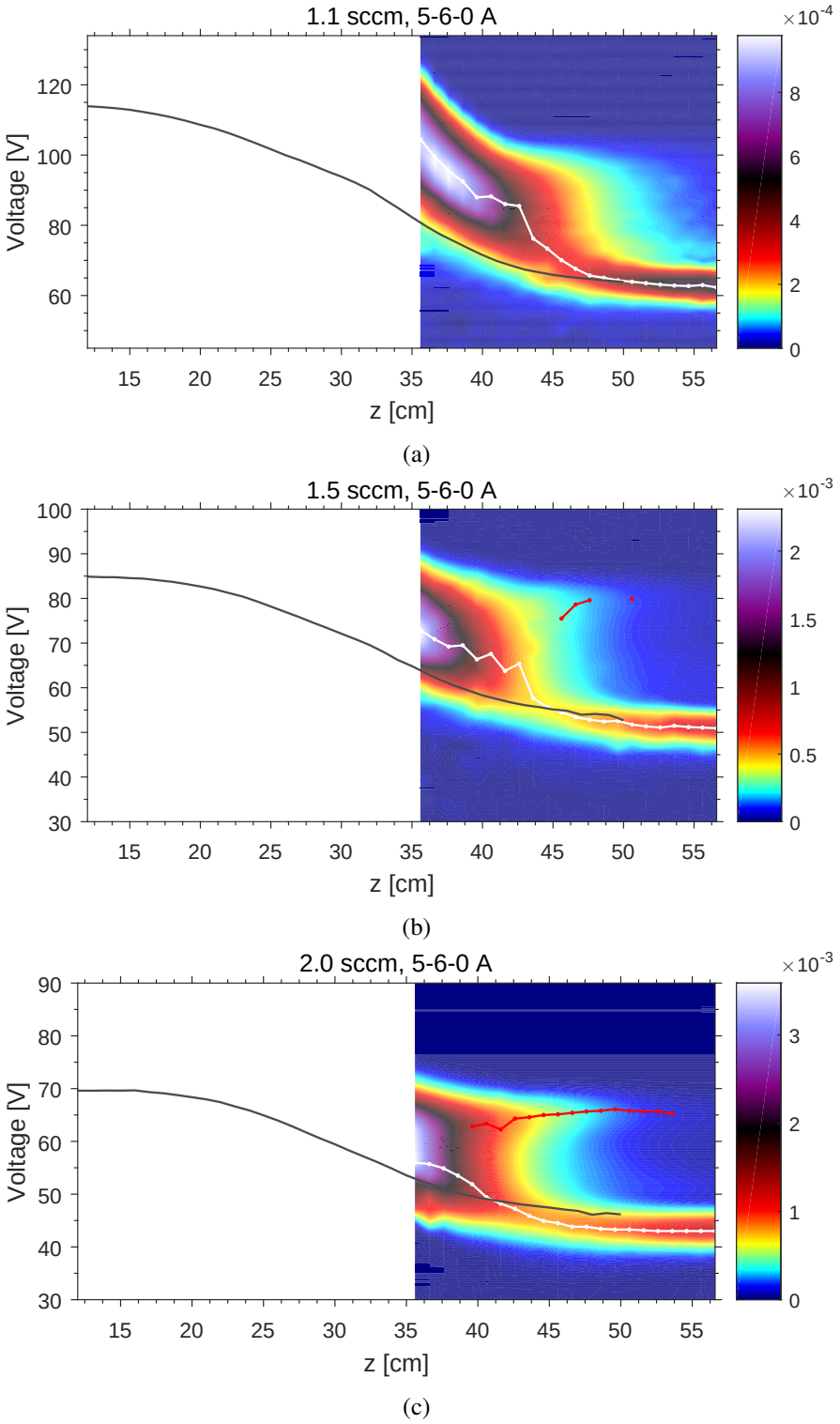


**Figure 4.12:** Axial RFEA measurements from Njord for the magnetic field configuration 5-6-0 A at different pressures. The gray line is the plasma potential from the emissive probe. The white line represents the peak of the ion distribution and the red line represent the peak of the beam where it is detected.

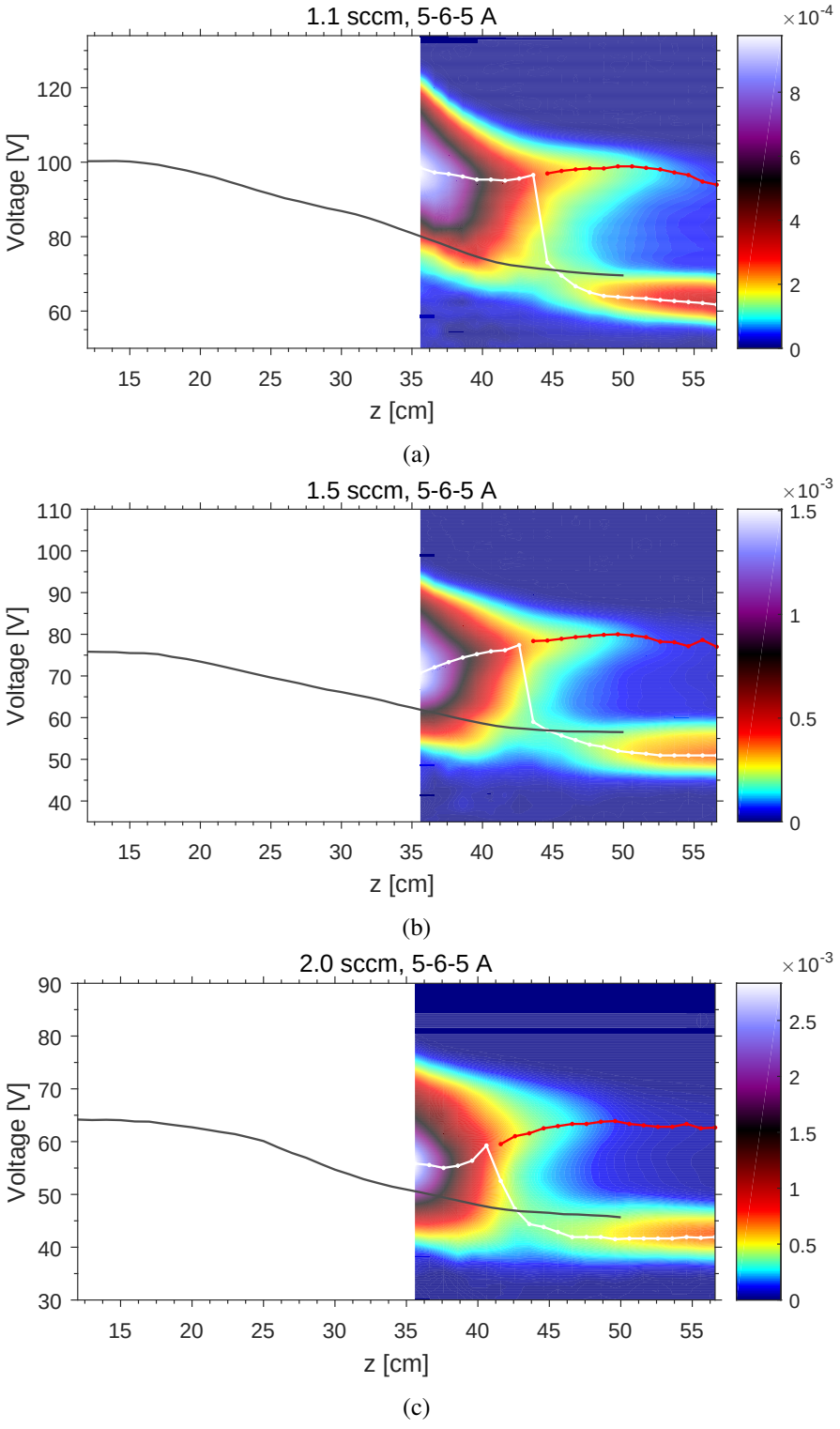


**Figure 4.13:** Axial profiles of ion distribution functions (IDF) from RFEA for the magnetic field configuration 5-6-5 A at different pressures in Njord. The gray line is the plasma potential from the emissive probe. The white line represents the peak of the ion distribution and the red line represent the peak of the beam where it is detected.

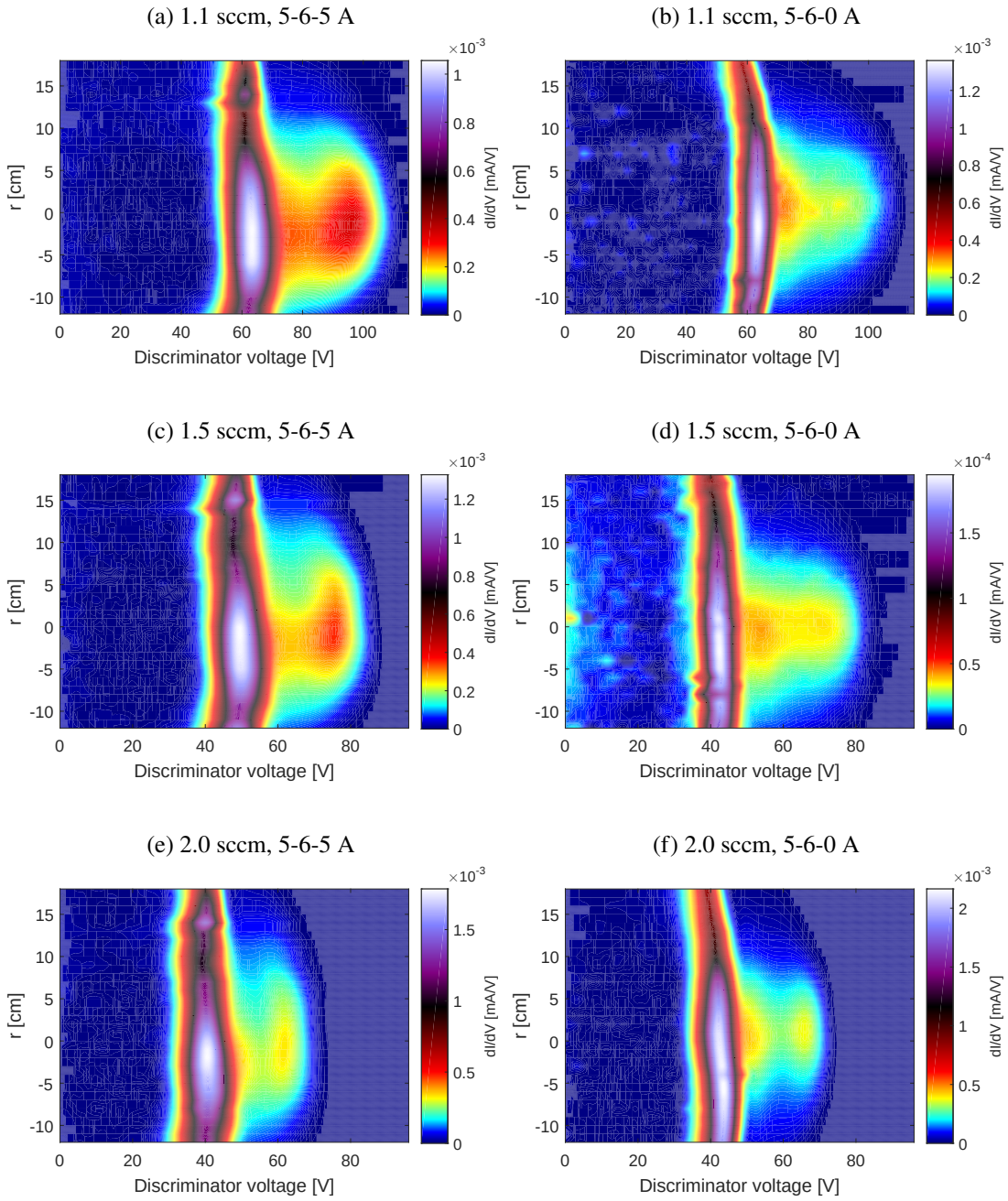


**Figure 4.14:** Radial profiles of ion distribution functions (IDF) from RFEA for different pressures and magnetic field configurations in Njord.

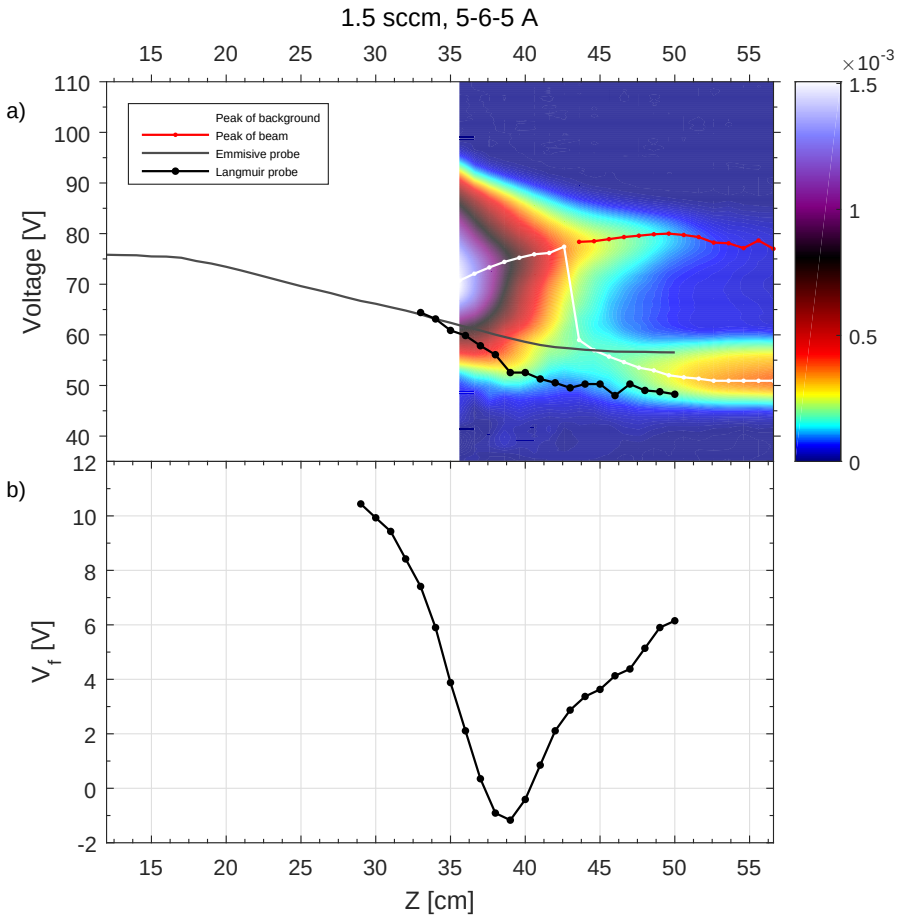


**Figure 4.15:** Comparison of different probe measurments for the 5-6-5 A magnetic field configuration in Njord with a pressure of 0.28 mTorr. The gray line is the plasma potential from the emissive probe. The white line represents the peak of the ion distribution and the red line represent the peak of the beam. The black line is the plasma potential and floating potential (separate plot) from the Langmuir probe

pressure. The density of the beam is comparable for the three pressures, although the background plasma density increase with increasing pressure. The beam widths also seems to be the same. All the measurements with the 5-6-5 A configuration has a small peak in background density around $r = 15$ cm, in addition to the main peak in the center.

With the 5-6-0 A configuration (b,d,f) only a narrow and diffuse beam is seen. At low pressure (1.1 sccm) hardly any beam is seen at all, instead a "tail" of high energy ions is slowly decreasing as we go to higher energies, and with the highest densities close to the background distribution. For 2.0 sccm a double peaked beam is seen, with one peak close to the background distribution and an other further away. The maximum energies of the distribution seems to correspond to the maximum energies for the 5-6-5 A configuration at the same pressures.

In figure 4.15 we give a comparison between the data from figure 4.13b and the plasma potential and floating potential from the Langmuir probe, shown as black lines. In 4.15a the gray line marks the plasma potential as measured with the emissive probe, the white line marks the

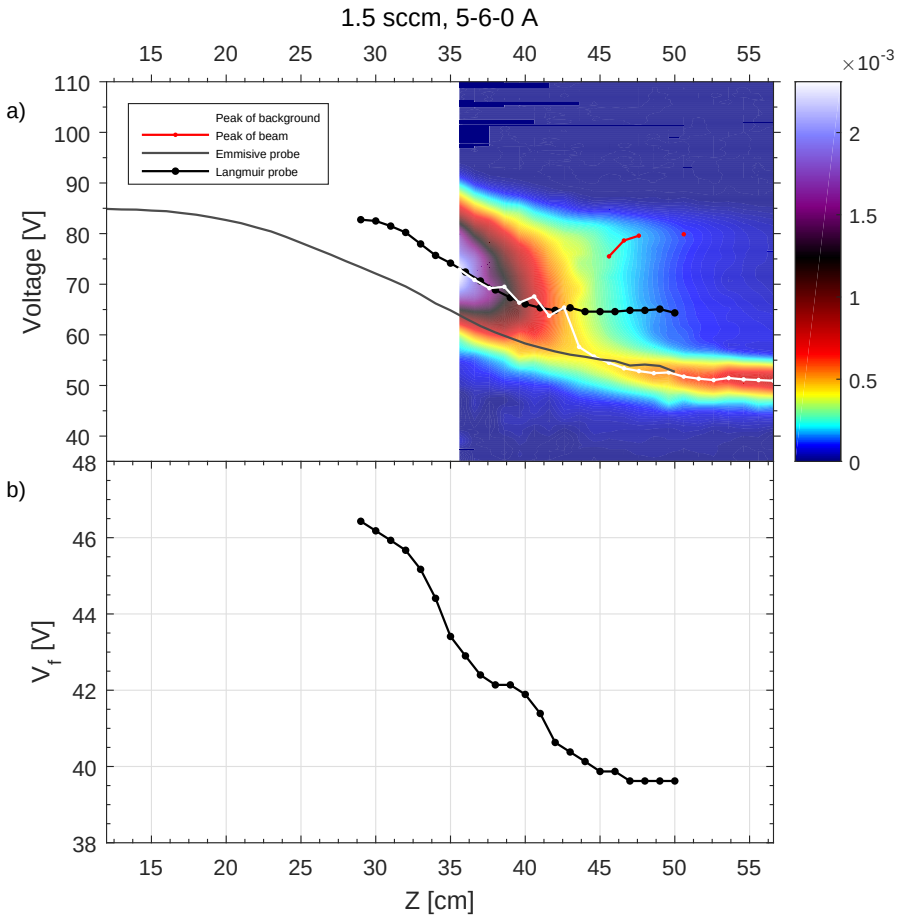


**Figure 4.16:** Comparison of different probe measurments for the 5-6-0 A magnetic field configuration in Njord with a pressure of 0.28 mTorr. The gray line is the plasma potential from the emissive probe. The white line represents the peak of the ion distribution and the red line represent the peak of the beam where it is detected. The black line is the plasma potential and floating potential (separate plot) from the Langmuir probe

maximum peak of the main distributions, the red line marks the peak of the beam, and the black line marks the plasma potential from the Langmuir probe. The Langmuir probe measurements can only reach the edge of the source, but in that area we see the plasma potential from the Langmuir probe and the emissive probe matches well. As we go into the junction and expansion chamber the plasma potential from the Langmuir probe moves away to lower potentials than the emissive probe. In the expansion chamber the plasma potential from the Langmuir probe matches the peak of the background distribution while the emissive probe stays at a slightly higher potential.

The floating potential from the Langmuir probe in figure 4.15b has a minimum at $z = 39$ cm. This is half way through the junction between the the source and the expansion chamber, and is the same area where the lower energies of the source distribution starts to disappear.

Figure 4.16 is the same as figure 4.15 only for the 5-6-0 A magnetic field configuration. In

figure 4.15a we see that the plasma potential from the emissive probe follows the lower border of the source distribution, and that it also matches well with the peak of downstream background distribution, in contrast to what happened with the 5-6-5 A configuration, where the emissive probe measurements where higher (figure 4.15). The Langmuir probe plasma potential (in black) also behave differently here, and seems to line up with the peak of the ion distribution coming from the source in stead of aligning with the emissive probe measurements. This trend of the Langmuir probe measurements seems to continue into the expansion chamber even if the peak of source distribution disappear and is replaced by the downstream background distribution. The plasma potential from the Langmuir probe stays much higher than the peak of the background distribution. This is opposite behavior than that we saw for the 5-6-5 A configuration (figure 4.15a).

In figure 4.16b we see the floating potential from the Langmuir probe is gradual decreasing away from the source. There is no indication of a minimum like the one we saw in figure 4.15b.

In figure 4.17 LIF-measurements from the plasma condition in figure 4.15 and 4.16 is given for comparison. Both measurements is taken at $z = 55$ cm and with 1.5 sccm flow. The most striking differences in the figure is size and the position of the background distribution. For the 5-6-5 A magnetic field configuration the background distribution is centered around 0 km/s while for the 5-6-0 A magnetic field configuration the background distribution is centered around 1 km/s that means it has a significant flow. The background distribution for 5-6-0 A is also significantly lower than for 5-6-5 A. When it comes to the beam the 5-6-5 A configuration has a clear beam around 11 km/s while for 5-6-0 A the beam is smaller and much more spread out. The beam velocity seems to be the same.

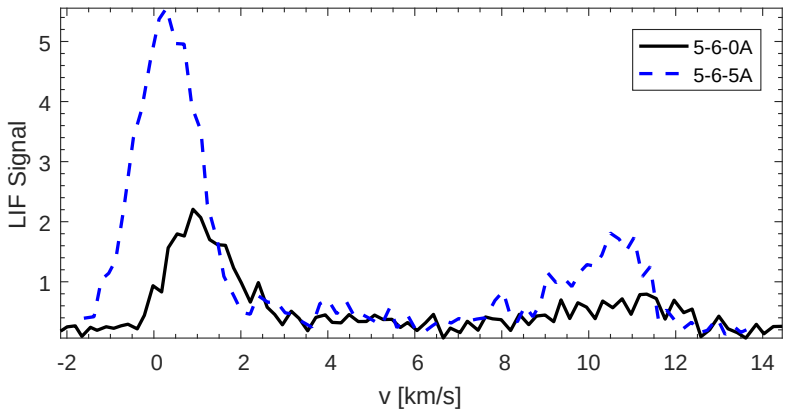


**Figure 4.17:** LIF measurements of velocity distribution function, $f(v)$ taken at $z = 55$ cm in Njord for the two different magnetic field configurations 1.5 sccm giving a pressure of 0.28 mTorr. The solid line is the 5-6-0 A configuration while the dashed line is the 5-6-5 A configuration.

## 4.4 Radial profiles of HELIX-LEIA

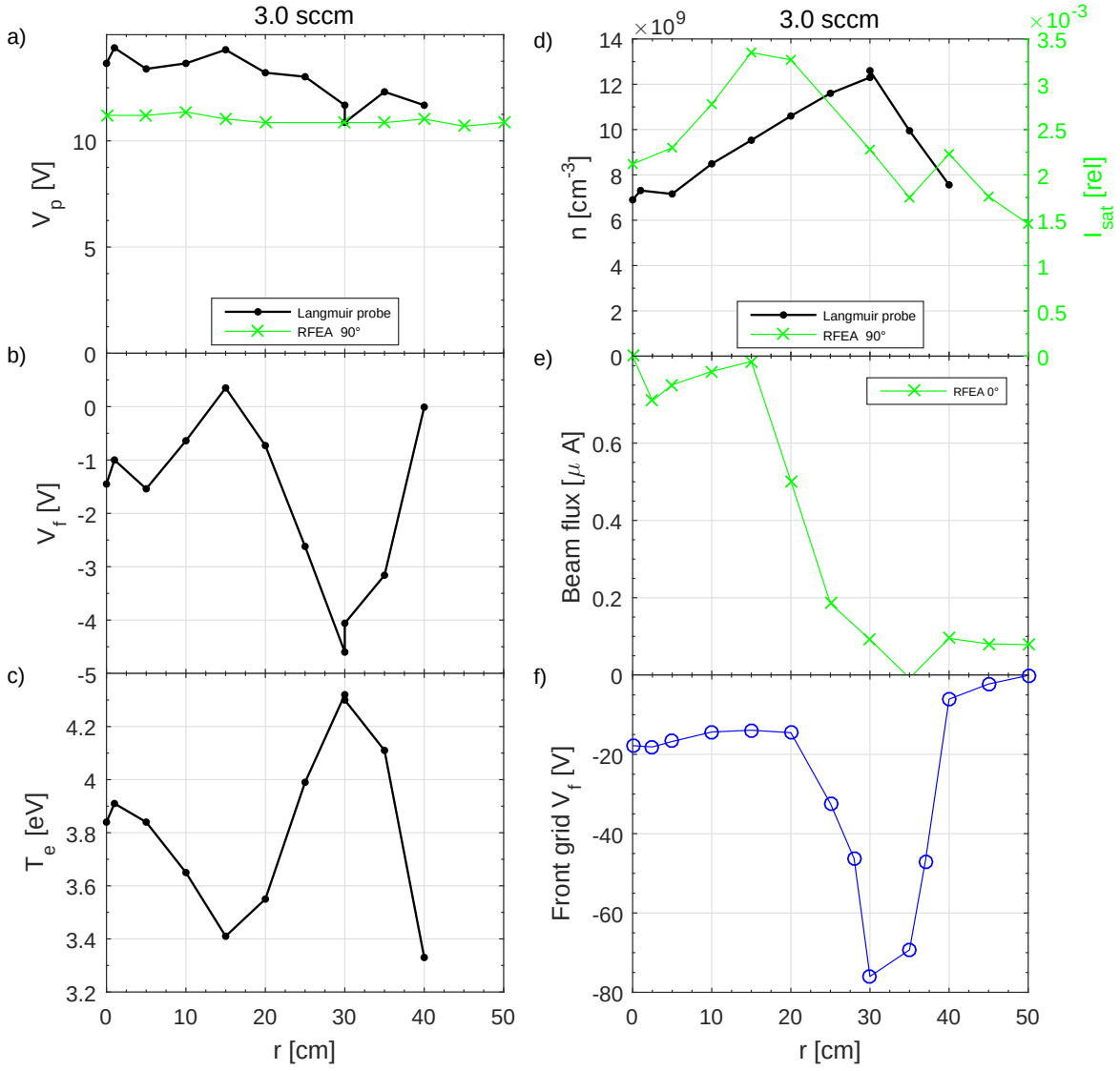


**Figure 4.18:** Radial profiles from LEIA at $z = 80$ cm with a flow of 3.0 sccm. a) Plasma potential from Langmuir probe (dots) and RFEA (crosses). b) Floating potential from Langmuir probe. c) Electron temperature from Langmuir probe. d) Ion densities from Langmuir probe (dots) and Ion saturation current from RFEA (crosses). e) Beam flux (in units of current) from RFEA. f) Potential of a floating front grid of the RFEA.

Figure 4.18 shows some radial profiles from LEIA at $z = 80$ cm done with Langmuir probe and RFEA. In figure 4.18a the plasma potential from the Langmuir probe and the RFEA is fairly consistent. The plasma potential from RFEA is taken as the peak of the distribution when the RFEA is facing 90° away from the source. The potential measured with the Langmuir probe is about 20% higher in the center and decrease towards the RFEA value at $r = 20$ cm. This difference might be related to the difficulty of finding an accurate plasma potential with a Langmuir probe in a RF-plasma [49].

In figure 4.18b the floating potential has a peak around $r = 15$ cm and then drops to a minimum around $r = 30$ cm.

The electron temperature in figure 4.18c has one minimum of 3.4 eV at around $r = 15$ cm and a maximum of about 4.2 ev at $r = 30$ cm.

Figure 4.18d shows the ion density from the Langmuir probe and the ion flux to the RFEA (measured 90° away from the source). The density peaks at $r = 30$ cm while the ion flux to the RFEA has a peak at $r = 15$ cm and a smaller peak at $r = 40$ cm.

In figure 4.18e the total integrated beam flux is fairly stable out to $r = 15$ cm, then it fades out and disappear at $r = 30$ cm. Using the reduction to half of the maximum flux as a measure of the beam width [35] we find the beam radius to be $r_{1/2} = 20$ cm.

For the RFEA measurements in LEIA we did some control measurements with a floating front grid where we also registered the potential of the floating grid and kept the probe facing the source. We discovered that the front grid was floating at a much lower potential than the Langmuir probe. Figure 4.18f shows this front grid potential, and we notice that around $r = 30$ – 35 cm the potential drops dramatically to around $-75$ V. We suspect that it might be due to a flux of energetic electrons hitting the front grid in this region.

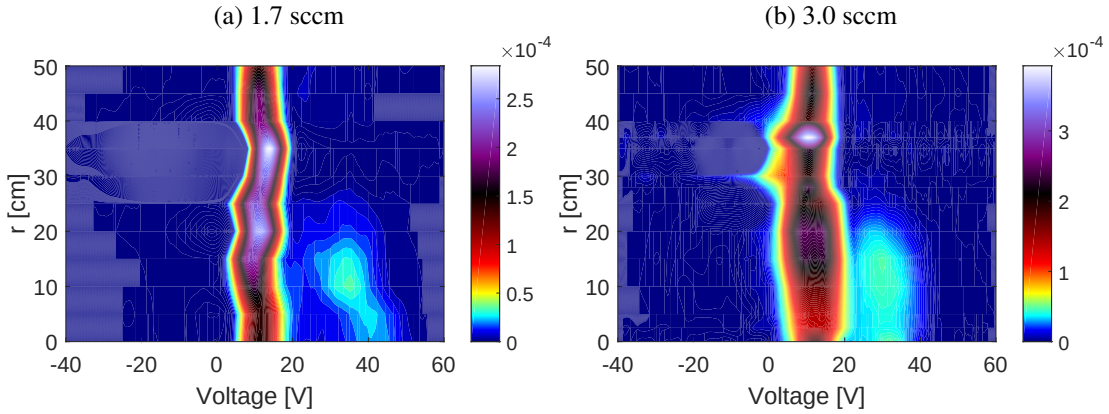


**Figure 4.19:** Radial profiles of ion distribution functions (IDF) from RFEA in HELIX-LEIA at $z = 80$ cm.

Figure 4.19 shows the full radial RFEA scans for 1.7 sccm, figure 4.19a, (corresponding to 0.15 mTorr in HELIX and 0.058 mTorr in LEIA) and 3.0 sccm, figure 4.19b, (corresponding to 0.92 mTorr in HELIX and 0.089 mTorr in LEIA). At 1.7 sccm the beam seems to have a higher velocity (energy) in the center than at the edges. The beam also has a higher density at the edges than in the center. both these things might be related to the radial expansion of the beam. We also see that the lover pressure (1.7 sccm) gives a higher beam energy (velocity) than the higher pressure (3.0 sccm).

Figure 4.20 presents the parameters derived from the RFEA measurements for 1.7 sccm in figure 4.19a. In figure 4.20a the plasma potential from RFEA is taken as the peak of the distribution when the RFEA is facing 90° away from the source. The potential is fairly flat

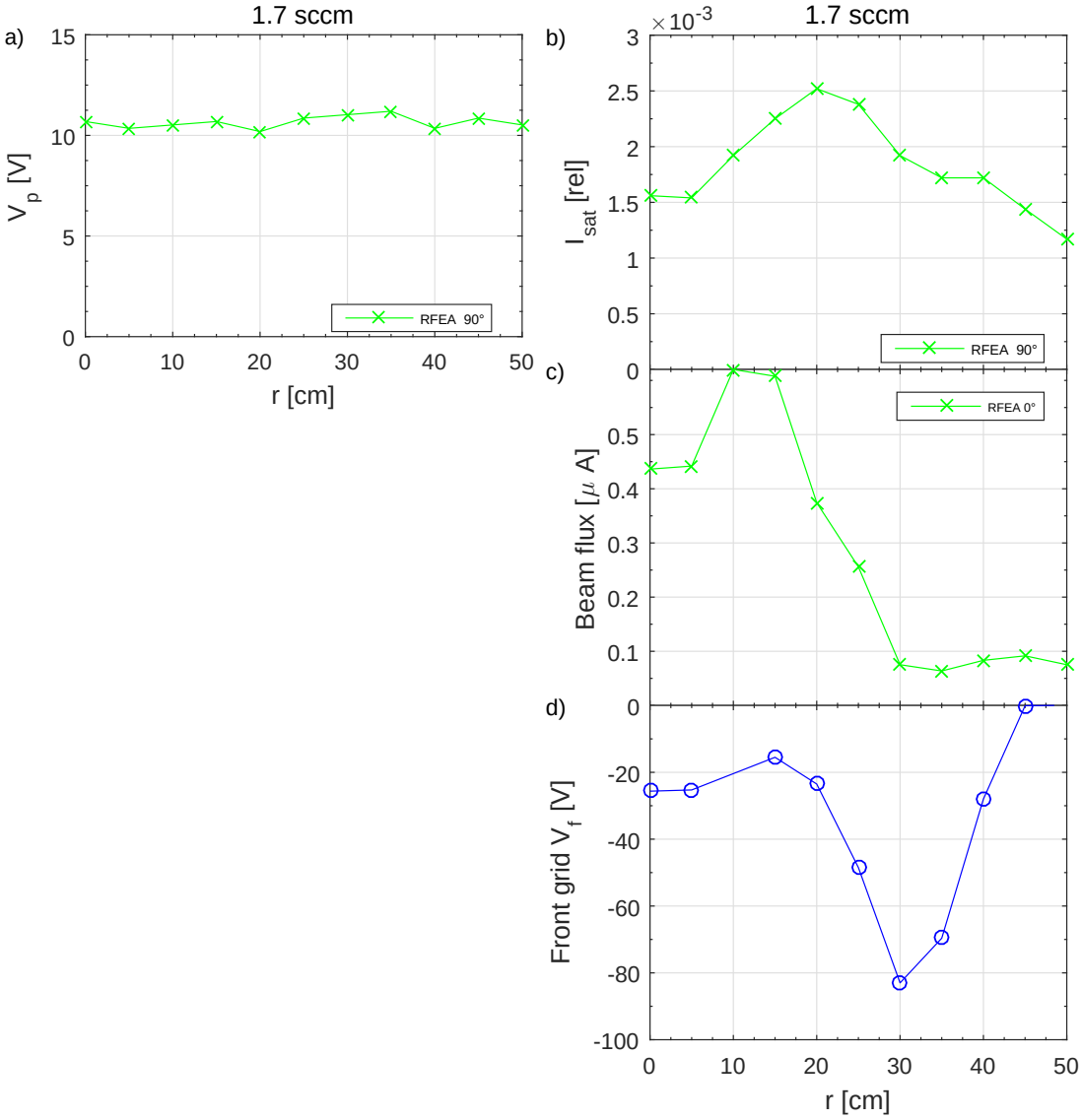


**Figure 4.20:** Radial profiles from LEIA at $z = 80$ cm with a flow of 1.7 sccm. a) Plasma potential RFEA (crosses). b) Ion saturation current from RFEA (crosses). c) Beam flux (in units of current) from RFEA. d) Potential of a floating front grid of the RFEA.

through out the scan, and it is also similar to the one at 3.0 sccm (figure 4.18a). Also the ion saturation current (figure 4.20b) behaves similar to figure 4.18d, with a main peak at 20 cm and a smaler peak at 40 cm. The beam flux (figure 4.20c) behaves a bit differently than for 3.0 sccm. A clear maximum in the beam flux is seen between $r = 10$ cm and $r = 15$ cm, while the beam flux is lower in the center. the beam still stretches about to about $r = 30$ cm and the beam radius is $r_{1/2} = 23$ cm. The floating front grid in figure 4.20d has a very similar behavior to the one for 3.0 sccm in figure 4.18f.

## 4.5 Radial profiles in Njord

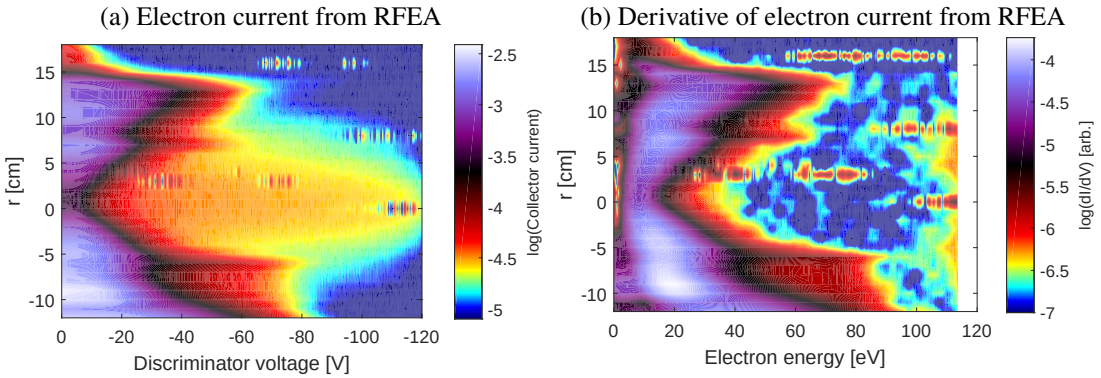


**Figure 4.21:** Radial profile of electron-RFEA measurements in Njord with 2.0 sccm flow. a) Collector currents, b) derivatives of the collector currents.

For the results presented in figure 4.21 the RFEA was used with grids biased to collect energetic electrons as described in section 3.3.4 in chapter 3. In figure 4.21a the logarithm of the collector current is plotted vs discriminator voltage and radial position. The high-energy electrons seen at $\pm 7$ cm corresponds to the width of the source and the width of the ion beam, while the high energy electrons at 14 cm corresponds well with a magnetic field line emerging from the edge of the source [67]. We have earlier seen increased ion densities in this position [67] (se figure 4.23a), possibly due to ionization from the high-energy electrons. The yellow "thong" in the figure indicates a small density of electrons with energies larger than 100 eV near the center of the plasma column. Figure 4.21b shows the derivative of the collector current witch is proportional to the EEDF for high energy electrons. Much of the same features observed in figure 4.21a are also observed in the here, but the derivative is more noisy and does not offer any additional information, so for the rest of the discussion we prefer to interpret the collector current directly without taking the derivative.

Figure 4.22a shows the plasma potential from Langmuir probe (dots), emissive probe (circles), RFEA facing the source (crosses) and away from the source (triangles). The plasma potential from the RFEA measurements corresponds well with the Langmuir probe while the plasma potential from emissive probe is a 7–8 V higher. These measurement are not carried out at the same time so it might be that the plasma conditions were slightly different due to different antenna matching conditions. Also the Langmuir probe and the RFEA may affect the plasma and reduce the plasma potential. It is also worth to notice that the potential from the emissive probe has peaks near $r = \pm 10$ cm while the Langmuir probe and the RFEA has minimas at the same place.

In figure 4.22b the floating potential from Langmuir probe also shows distinct minima around $r = \pm 8$ cm.

Figure 4.22c shows electron temperature from Langmuir probe (dots) and electron-RFEA

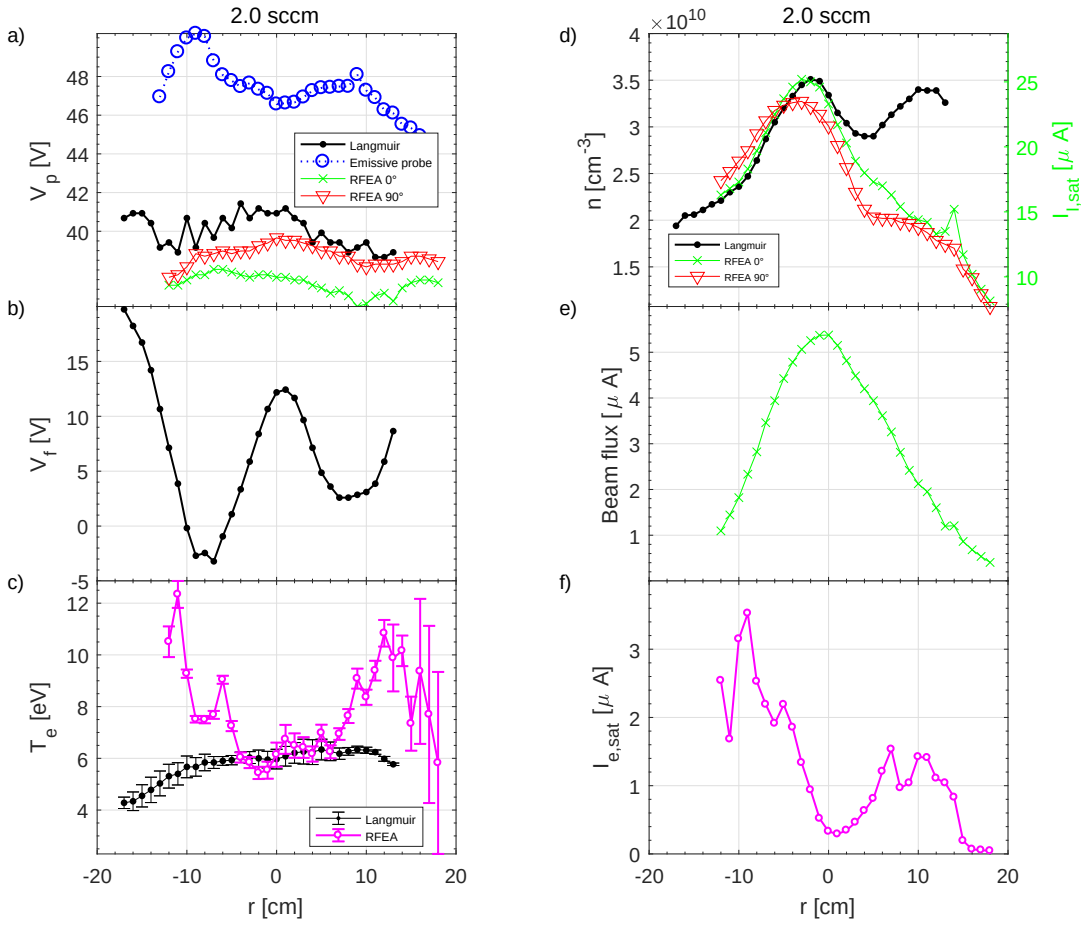


**Figure 4.22:** 2.0 sccm 5-6-5A 1000W. a) Plasma potential from Langmuir probe (dots), emissive probe (circles) and RFEA (crosses). b) Floating potential form Langmuir probe. c) Electron temperature form Langmuir probe (dots) and electron-RFEA (crosses). Ion density from Langmuir probe (dots) Ion saturation current from the RFEA facing the source (crosses), Ion saturation current from the RFEA facing 90° away from the source (triangles). e) Beam flux (in units of current) from RFEA. f) Electron saturation current from electron-RFEA.

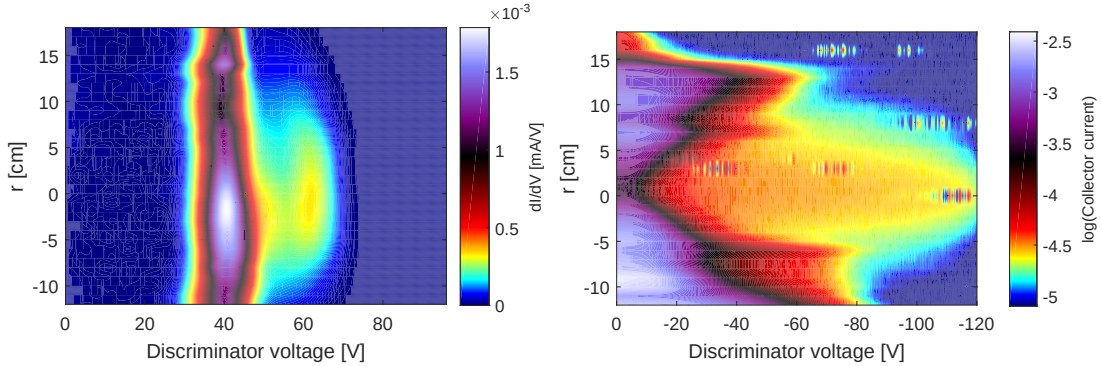


(a) IDF from RFEA.

(b) Electron current from RFEA

**Figure 4.23:** RFEA measurements of (a) ions and (b) electrons in Njord at 2.0 sccm flow and 5-6-5 A magnetic field.

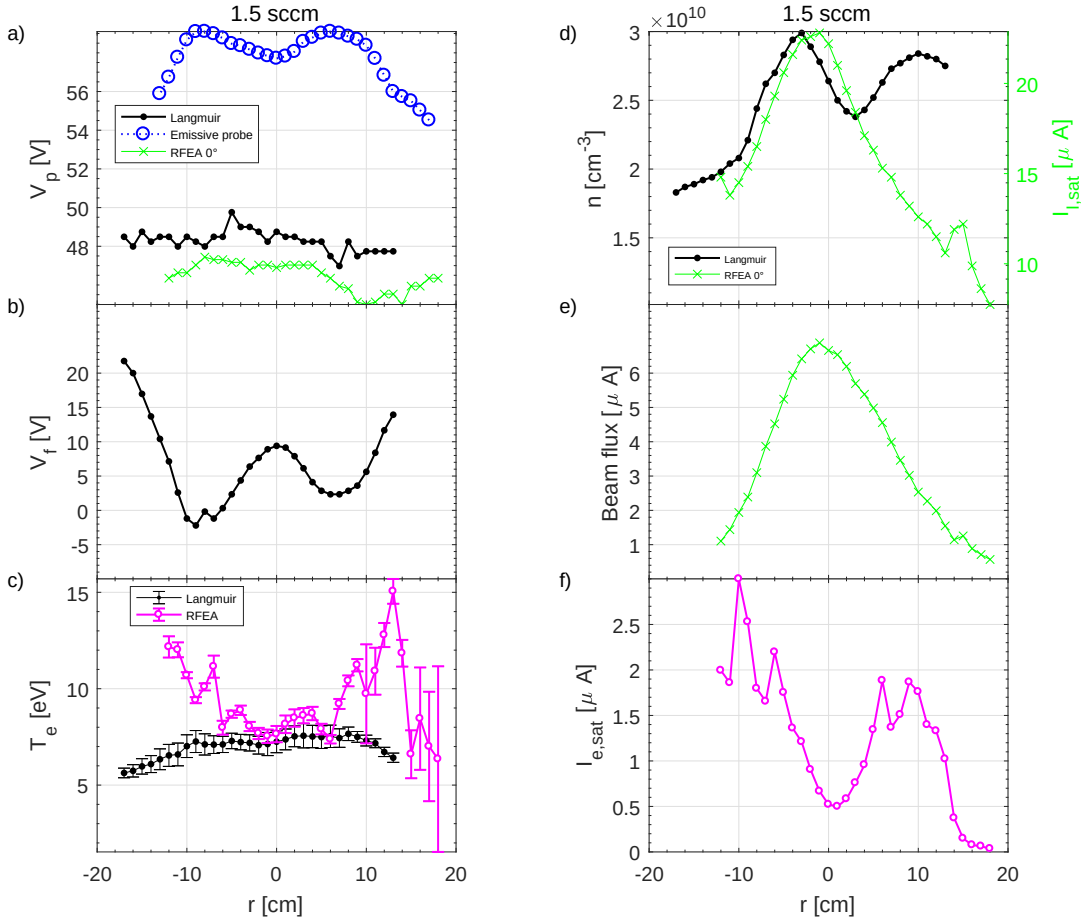


**Figure 4.24:** 1.5 sccm 5-6-5A 1000W. a) Plasma potential from Langmuir probe (dots), emissive probe (circles) and RFEA (crosses). b) Floating potential form Langmuir probe. c) Electron temperature from Langmuir probe (dots) and electron-RFEA (crosses).d) Ion density from Langmuir probe (dots) Ion saturation current from the RFEA (crosses). e) Beam flux (in units of current) from RFEA. f) Electron saturation current from electron-RFEA.

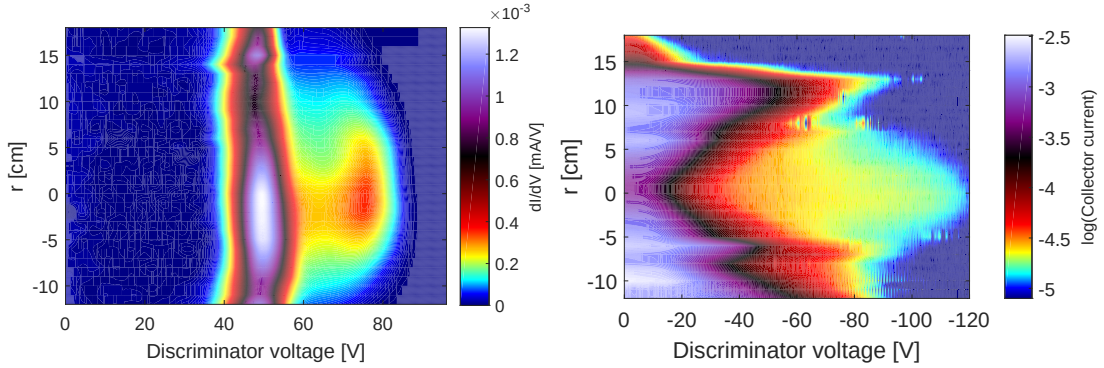


(a) IDF from RFEA

(b) Electron current from RFEA

**Figure 4.25:** RFEA measurements of (a) ions and (b) electrons in Njord at 1.5 sccm flow and 5-6-5 A magnetic field

(crosses). The electron temperature is extracted from the current-voltage characteristic of the RFEA. Only the the high-energy tail of the EEDF is detected [65]. In the center the RFEA and Langmuir probe corresponds well, but at the edges the RFEA detects a higher temperature indicating a high energy population of electrons [20].

Figure 4.22d shows the ion density from the Langmuir probe and the ion flux to the RFEA both facing the source, 0°, and 90° away from the source. Both the density and the ion flux has a peak in the center corresponding to where the beam is detected. The density also has a peak around $r = +10$ cm that is not observed for $r = -10$, and it is also not observed in the ion flux. Instead we observe a small peak in the ion flux at $r = 14$ cm when the RFEA is facing the source that does not exist when the probe is turned 90° away from the source. The asymmetry in the density profile might be explained at least in part by the fact that for negative $r$ the probe shaft is crossing the center of plasma and this might change the plasma somewhat.

In figure 4.22e the total integrated beam flux has a peak in the center and then falls om to each side. Using the halfwidth the beam radius is around $r_{1/2} = 7$ cm.

Figure 4.22f show the electron saturation current from electron-RFEA,wich is propotional to the energetic electron flux to the RFEA. The profile has a minimum in the center and peaks at $r = 7$, 10, $-5$ and $-9$ cm.

Figure 4.23 shows a comparison between the radial profile of the ion distribution function (IDF) and the electron current from the electron-RFEA. These are the complete data that the RFEA parameters in figure 4.22 are derived from. In figure 4.23a radial profiles of RFEA Ion Distribution Function (IDF) [67] measured at $z = 55$ cm is seen. A beam can be seen at around 60 V. The beam flux decreases with radius and disappear around $r = 12$ cm. The background distribution (around $V = 40$) has a maximum in the center ($r = 0$) and another peak at $r = 14$ cm, corresponding to a maximum in the energetic electron current shown in figure 4.23b.

Figure 4.24 shows that the results described for 2.0 sccm conditions are largely reproduced at 1.5 sccm showing the same features for all accessible parameters. The plasma potential (4.24a) and the floating potential (4.24b) is behaving similarly to figure 4.22. The high energy tail temperature in figure 4.24c peaks in the same places at in figure 4.22c. Density in figure 4.24d is a bit lower but still the same profile as in 4.22d. The electron flux to the RFEA in figure 4.22f has peaks in the same places as in figure 4.22f, although the height of the peaks is slightly different.

In figure 4.25 the whole scans from the ion RFEA (a) and electron-RFEA (b) is shown. A comparisons of the ion-RFEA measurments at different pressures is given in Paper 4 [67] and a further description of the results from the electron-RFEA measurements is given in Paper 5 [88]

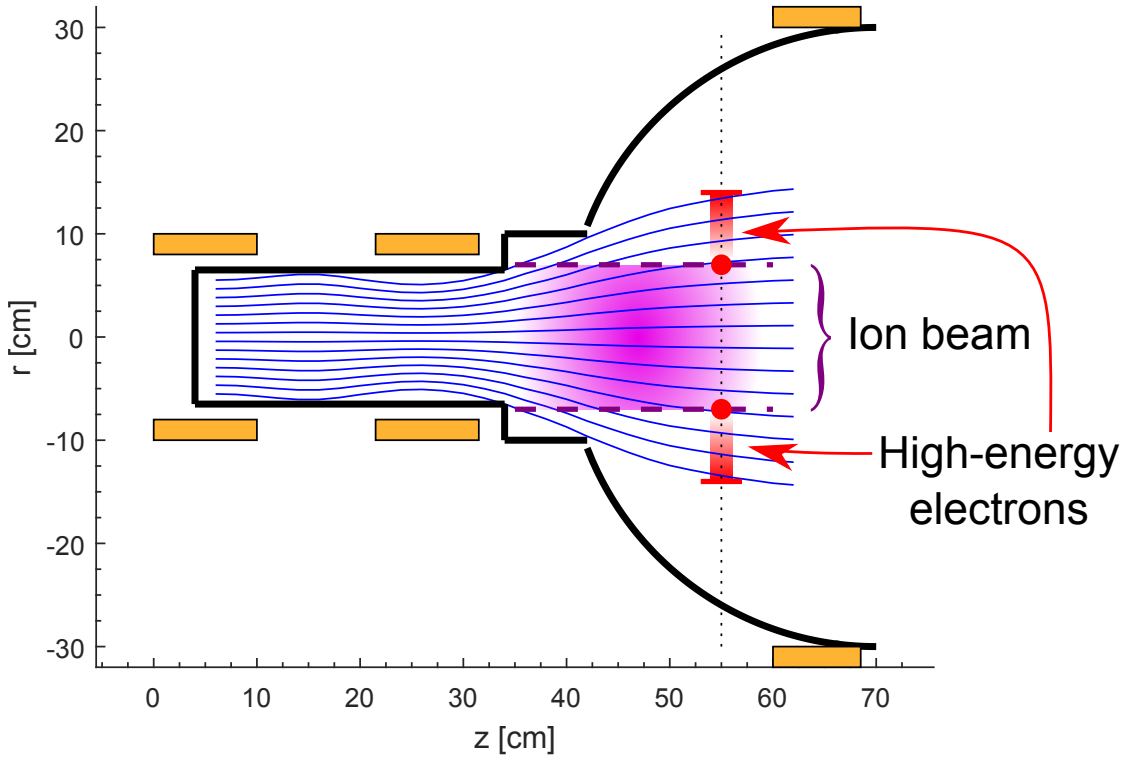


**Figure 4.26:** Positions of observed features with respect to the magnetic field.

## 4.6 Summarizing observations

At last we take a closer look at the positions of the shown features with respect to the magnetic field and source geometry. Computations of the outermost field lines from the source in the 5-6-0 A configuration (section 2.1.1) have shown that it connect with the walls of the port between the source and the expansion chamber (figure 2.4). This will alter the path of electrons emerging from the source and may explain some of the behavior we have seen in this configuration in figure 4.12 and 4.14. By using a 5 A current in the downstream coil, producing a downstream magnetic field of 30G, the outermost field line no longer connects to the port. This seems to be a much more favorable configuration for beam production, as seen by comparing figure 4.12 and figure 4.13. To get undisturbed beam measurements we have choosen to focuse this study on the configuration with a 5 A current in the downstream coil, the 5-6-5 A configuration.

Figure 4.26 shows the magnetic field lines originating in the source of Njord calculated from the axial magnetic field, with 5 A in the third coil. The three magnetic coils are marked in orange. The vertical dotted line at $z = 55$ cm marks the position of the radial probes. The horizontal dashed lines at $r = \pm 7$ cm represent the width of the source and the beam, as seen in figure 4.23e, figure 4.24e and paper 4 [67]. With the electron RFEA we see a peak in the electron current at this point (marked with a red dot). (Paper 5 [88]). The red marks crossing the line at $z = 55$ cm and $r = \pm 14$ cm are the locations of the small maxima seen in the ion RFEA measurements

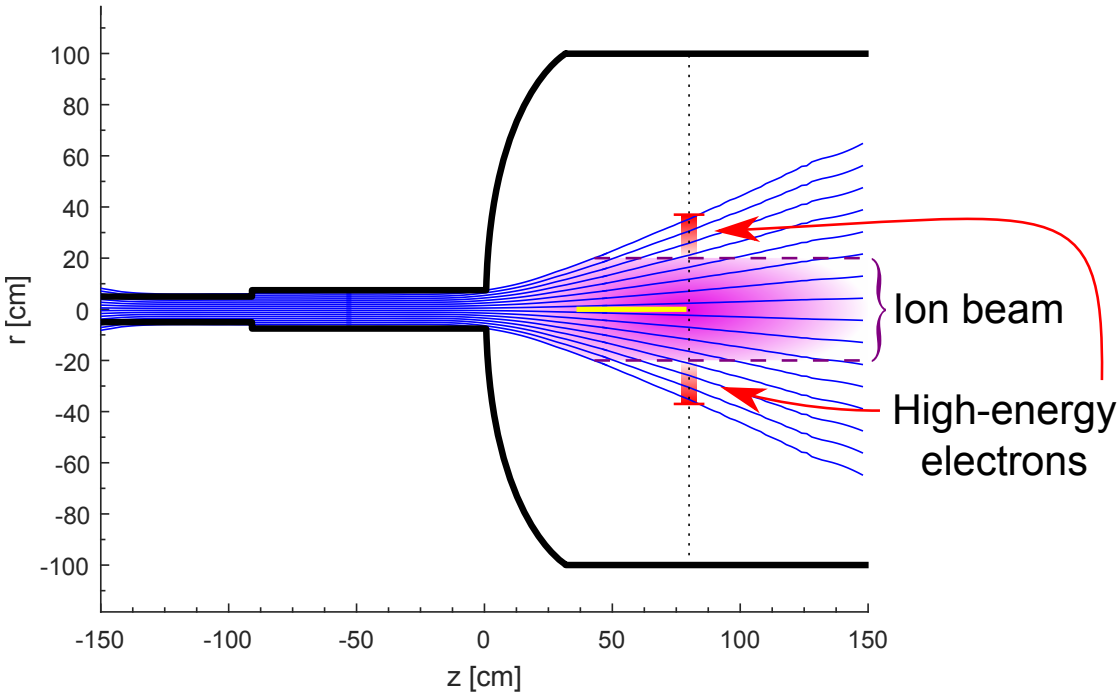


**Figure 4.27:** Magnetic field lines and positions of the observed features in HELIX-LEIA.The yellow line in the middle of the expansion chamber marks the area accessible with the reentrant LIF probe.

(figure 4.23a and paper 4 [67]). These marks fits well with the calculated outermost magnetic field line coming from the source and they are also in the same area where we observe high electron temperatures and high electron currents with the RFEA [88] (Paper 5).

Figure 4.27 shows the magnetic field lines in HELIX-LEIA that originates in the source HELIX based on the magnetic field shown in figure 2.6. The magnetic field lines are calculated in the same way as in figure 2.4. The vertical dotted line at $z = 80$ cm marks the position of the radial probes. The horizontal dashed lines at $r = \pm 20$ cm represent the width of the beam as seen in figure 4.18e and paper 4 [67]. The red marks crossing the line at $z = 80$ cm marks the small ion maximum seen in the RFEA measurements at $r = 37$ cm (Figure 9,paper 4 [67]). They fit well with the outermost field line coming from the source. The yellow line in the middle of the expansion chamber (LEIA) marks the area accessible with the reentrant LIF probe.

The width of the ion beam indicates that the ions follow the magnetic field lines until the field is down to about 60 Gauss, corresponding to an ion Larmor radius of 13 cm. From there on the ions continue as a spatial collimated beam. The effects of the magnetic field on the ion beam and the high-energy electrons are further discussed in paper 4 [67] and paper 5 [88].

# Chapter 5

# Articles

## Paper 1

W. J. Miloch, N. Gulbrandsen, L. N. Mishra, and Å. Fredriksen, **"The role of acceptance angle in measurements with ion energy analyzers: Study by numerical simulations"**, *Applied Physics Letters*, **97**, 261501, (2010), doi: 10.1063/1.3531757.

This article is the first in a series of three where we used a 3-dimentional particle-in-cell simulation developed by Wojciech Miloch to simulate an Retarding Field Energy Analyzer (RFEA) in a plasma. We investigate how the sheath surrounding the probe in combination with a certain acceptance angle of the probe would affect the velocity distribution seen by the probe. For convenience in the simulation, the RFEA was assumed to be spherical. This represents an extreme case furthest from an idealized planar probe.

We showed that the low energy tail (velocities lower than the peak) is completely an effect of the sheath in combination with the acceptance angle. In addition, the high-energy part of the distribution is much wider than expected from 1-dimentional theory.

For flowing plasmas or plasmas with beams, the orientation of the analyzer's orifice gives different results due to bending of ion trajectories in the vicinity of the analyzer. We demonstrated that the peak of the ion velocity distribution seen by the probe is at slightly lower energies than the plasma potential.

## Paper 2

W. J. Miloch, N. Gulbrandsen, L. N. Mishra, and Å. Fredriksen, **"Ion velocity distributions in the sheath and presheath of a biased object in plasma"**, *Physics of Plasmas*, **18**, 083502, (2011), doi: 10.1063/1.3614520.

In this second article from the 3-dimensional particle-in-cell simulation of a Retarding Field Energy Analyzer (RFEA) we investigated the ion velocity distribution in the sheath surrounding

the probe. By integrating over spherical shells around the probe of velocity directed towards the probe, assuming spherical symmetry, we managed to reconstruct the radial velocity distribution to the ions in the sheath. The ion dynamics around the object lead to distorted radial velocity distributions in the presheath and the sheath edge region. We investigated how different potentials of the probe affect the velocity distribution as well as, ion temperatures, and ion masses, and showed that the velocity distribution does not necessary follow 1-dimensional sheath models. We observed an increase in the thermal velocity in the radial direction far in the sheath.

## Paper 3

N. Gulbrandsen, W. J. Miloch, and Å. Fredriksen, **"Interpretation of Ion Velocity Distributions Measured with a Grounded Retarding Field Energy Analyzer (RFEA) in an Inductively Coupled Helicon Plasma"**, *Contributions to Plasma Physics*, **53**, 27, (2013), doi: 10.1002/ctpp.201310005.

This article interprets the results from the two previous articles. A Retarding Field Energy Analyzer (RFEA) with a grounded surface in a plasma will be surrounded by a sheath. The ion distribution function (IDF) measured at the probe will be distorted as compared to the IDF in a plasma unaffected by the sheath. We interpret the radial ion distribution from paper 2 and compare them to some simple models used to interpret RFEA-measurements. Our main finding is that none of the simple models manages to explain our simulation results

## Paper 4

N. Gulbrandsen, Å. Fredriksen, J. Carr, and E. Scime, **"A comparison of ion beam measurements by retarding field energy analyzer and laser induced fluorescence in helicon plasma devices"**, *Physics of Plasmas*, **22**, 033505, (2015), doi: 10.1063/1.4913990.

This article is a thorough comparison of ion beam diagnostics using Retarding Field Energy Analyzer (RFEA) and Laser Induced Fluorescence (LIF) in two different Helicon Plasma Devices. Here we both compared two different types of diagnostics, one intrusive (RFEA) and one remote, non-intrusive (LIF), and we also compared them in two different Helicon Plasma Devices, HELIX-LEIA at West Virginia University and Njord at University of Tromsø. The devices were different both in size and parameter range. While the LIF technique provides a direct measurement of the velocity distribution in the plasma, the RFEA measures ion flux as a function of a retarding potential.

We presented a method to compare the two techniques, by converting the LIF velocity distribution to an equivalent of a RFEA measurement. We found good agreement between beam energies of the two methods. We also observed that the RFEA is capable of measuring ion

beams with densities too low for the LIF to resolve, while the LIF-technique better resolves the background ion distribution.

We present measurements of the axial development of the ion beam in both experiments. Beam densities drop exponentially with distance from the source, both in LIF and RFEA measurements and we found an efficient quenching cross section from LIF in LEIA to be $\sigma_{b,*} = 4 \times 10^{-19}$ m$^2$, and the beam collisional cross sections by RFEA in Njord to be $\sigma_b = 1.7 \times 10^{-18}$ m$^2$.

This article contains the major results from my 10 months research stay at West Virginia University, USA.

## Paper 5

N. Gulbrandsen and Å. Fredriksen, **"RFEA Measurements of High-Energy Electrons in a Helicon Plasma Device with Expanding Magnetic Field"**, *Frontiers in Physics*, **5**, 2, (2017), doi: 10.3389/fphy.2017.00002.

This paper looks into an interesting finding I came across during my investigation of ion beams. We had for long observed disturbances in the RFEA measurements outside of the beam at some certain radial positions where we would need a very high repeller voltage (more that 200 V) to get a reasonable Ion Distribution Function from the RFEA. Also in the HELIX-LEIA plasma device at West Virginia University, we observed that a floating front grid charged up very negatively in a certain radial area outside the ion beam. This all indicates the presences of a population of electrons with very high energies.

In a radial scan with a RFEA biased to collect ions a localized increase in the plasma ion density near the magnetic field line emerging from the plasma near the wall of the source was observed. This is interpreted as a signature of high-energy electrons ionizing the neutral gas. In addition, a dip in the floating potential of a Langmuir probe is evident in this region where high-energy electrons is observed.

In this article, we used an RFEA with inverted grid biases to measure the high-energy electrons. We found a significant population of high-energy electrons just inside the magnetic field line mapping to the edge of the source. A second peak in high-energy electrons density was observed in a radial position corresponding to the radius of the source. In addition, throughout the main column a small contribution of high-energy electrons was observed.

# Paper 1:

# The role of acceptance angle in measurements with ion energy analyzers: Study by numerical simulations

W. J. Miloch, N. Gulbrandsen, L. N. Mishra, and Å. Fredriksen, *Applied Physics Letters*, **97**, 261501, (2010), doi: 10.1063/1.3531757.

# Paper 2:

# Ion velocity distributions in the sheath and presheath of a biased object in plasma

W. J. Miloch, N. Gulbrandsen, L. N. Mishra, and Å. Fredriksen, *Physics of Plasmas*, **18**, 083502, (2011), doi: 10.1063/1.3614520.

# Paper 3:

# Interpretation of Ion Velocity Distributions Measured with a Grounded Retarding Field Energy Analyzer (RFEA) in an Inductively Coupled Helicon Plasma

N. Gulbrandsen, W. J. Miloch, and Å. Fredriksen, *Contributions to Plasma Physics*, **53**, 27, (2013), doi: 10.1002/ctpp.201310005.

# Paper 4:

# A comparison of ion beam measurements by retarding field energy analyzer and laser induced fluorescence in helicon plasma devices

N. Gulbrandsen, Å. Fredriksen, J. Carr, and E. Scime, *Physics of Plasmas*, **22**, 033505, (2015), doi: 10.1063/1.4913990.

# Paper 5 :

# RFEA Measurements of High-Energy Electrons in a Helicon Plasma Device with Expanding Magnetic Field

N. Gulbrandsen and Å. Fredriksen, *Frontiers in Physics*, **5**, 2, (2017), doi: 10.3389/fphy.2017.00002.

# Bibliography


[1] J. Hopwood, "Review of inductively coupled plasmas for plasma processing", *Plasma Sources Science and Technology*, **1**, 109, (1992), doi: 10.1088/0963-0252/1/2/006.

[2] P. Chabert and N. Braithwaite, *Physics of Radio-Frequency Plasmas*, Cambridge University Press, Cambridge, 2011, ISBN 978052176300.

[3] M. Lieberman and A. Lichtenberg, *Principles of Plasma Discharges and Materials Processing*, Wiley, New York, 2005, ISBN 9780471724247.

[4] R. W. Boswell, "Very efficient plasma generation by whistler waves near the lower hybrid frequency", *Plasma Physics and Controlled Fusion*, **26**, 1147, (1984), doi: 10.1088/0741-3335/26/10/001.

[5] R. W. Boswell and F. F. Chen, "Helicons-the early years", *IEEE Transactions on Plasma Science*, **25**, 1229, (1997), ISSN 0093-3813, doi: 10.1109/27.650898.

[6] F. F. Chen and R. W. Boswell, "Helicons-the past decade", *IEEE Transactions on Plasma Science*, **25**, 1245, (1997), ISSN 0093-3813, doi: 10.1109/27.650899.

[7] C. Charles and R. Boswell, "Current-free double-layer formation in a high-density helicon discharge", *Applied Physics Letters*, **82**, 1356, (2003), doi: 10.1063/1.1557319.

[8] C. Charles and R. W. Boswell, "Laboratory evidence of a supersonic ion beam generated by a current-free "helicon" double-layer", *Physics of Plasmas*, **11**, 1706, (2004), doi: 10.1063/1.1652058.

[9] L. P. Block, "A double layer review", *Astrophysics and Space Science*, **55**, 59, (1978), ISSN 1572-946X, doi: 10.1007/BF00642580.

[10] M. A. Raadu, "The physics of double layers and their role in astrophysics", *Physics Reports*, **178**, 25 , (1989), ISSN 0370-1573, doi: 10.1016/0370-1573(89)90109-9.

[11] M. A. Raadu, "Energy release in double layers", *Space Science Reviews*, **68**, 29, (1994), ISSN 1572-9672, doi: 10.1007/BF00749114.

[12] S. Eliezer and H. Hora, "Double layers in laser-produced plasmas", *Physics Reports*, **172**, 339 , (1989), ISSN 0370-1573, doi: 10.1016/0370-1573(89)90118-X.

[13] N. Hershkowitz, "Review of recent laboratory double layer experiments", *Space Science Reviews*, **41**, 351, (1985), ISSN 1572-9672, doi: 10.1007/BF00190655.

[14] C. Charles, R. W. Boswell, and R. Hawkins, "Oblique Double Layers: A Comparison between Terrestrial and Auroral Measurements", *Phys. Rev. Lett.*, **103**, 095001, (2009), doi: 10.1103/PhysRevLett.103.095001.

[15] J. M. Little and E. Y. Choueiri, "Thrust and efficiency model for electron-driven magnetic nozzles", *Physics of Plasmas*, **20**, 103501, (2013), doi: 10.1063/1.4824613.

[16] S. A. Cohen, N. S. Siefert, S. Stange, R. F. Boivin, E. E. Scime, and F. M. Levinton, "Ion acceleration in plasmas emerging from a helicon-heated magnetic-mirror device", *Physics of Plasmas*, **10**, 2593, (2003), doi: 10.1063/1.1568342.

[17] X. Sun, S. A. Cohen, E. E. Scime, and M. Miah, "On-axis parallel ion speeds near mechanical and magnetic apertures in a helicon plasma device", *Physics of Plasmas*, **12**, 103509, (2005), doi: 10.1063/1.2121347.

[18] N. Plihon, C. S. Corr, and P. Chabert, "Double layer formation in the expanding region of an inductively coupled electronegative plasma", *Applied Physics Letters*, **86**, 091501, (2005), doi: 10.1063/1.1869533.

[19] O. Sutherland, C. Charles, N. Plihon, and R. W. Boswell, "Experimental Evidence of a Double Layer in a Large Volume Helicon Reactor", *Phys. Rev. Lett.*, **95**, 205002, (2005), doi: 10.1103/PhysRevLett.95.205002.

[20] K. Takahashi, Y. Shida, T. Fujiwara, and K. Oguni, "Supersonic Ion Beam Driven by Permanent-Magnets-Induced Double Layer in an Expanding Plasma", *Plasma Science, IEEE Transactions on*, **37**, 1532, (2009), ISSN 0093-3813, doi: 10.1109/TPS.2009.2024342.

[21] E. E. Scime, I. A. Biloiu, J. Carr, S. C. Thakur, M. Galante, A. Hansen, S. Houshmandyar, A. M. Keesee, D. McCarren, S. Sears, C. Biloiu, and X. Sun, "Time-resolved measurements of double layer evolution in expanding plasmaa)", *Physics of Plasmas*, **17**, 055701, (2010), doi: 10.1063/1.3276773.

[22] S. Popescu, Y. Ohtsu, and H. Fujita, "Current-free double-layer formation in inductively coupled plasma in a uniform magnetic field", *Phys. Rev. E*, **73**, 066405, (2006), doi: 10.1103/PhysRevE.73.066405.

[23] H. S. Byhring, C. Charles, Å. Fredriksen, and R. W. Boswell, "Double layer in an expanding plasma: Simultaneous upstream and downstream measurements", *Physics of Plasmas*, **15**, 102113, (2008), doi: 10.1063/1.3002396.

[24] N. Singh, "Current-free double layers: A review", *Physics of Plasmas*, **18**, 122105, (2011), doi: 10.1063/1.3664321.

[25] C. Charles, "A review of recent laboratory double layer experiments", *Plasma Sources Science and Technology*, **16**, R1, (2007).

[26] A. M. Keesee, E. E. Scime, C. Charles, A. Meige, and R. Boswell, "The ion velocity distribution function in a current-free double layer", *Physics of Plasmas*, **12**, 093502, (2005), doi: 10.1063/1.2033647.

[27] W. Cox, C. Charles, R. W. Boswell, and R. Hawkins, "Spatial retarding field energy analyzer measurements downstream of a helicon double layer plasma", *Applied Physics Letters*, **93**, 071505, (2008), doi: 10.1063/1.2965866.

[28] T. Schröder, O. Grulke, and T. Klinger, "The influence of magnetic-field gradients and boundaries on double-layer formation in capacitively coupled plasmas", *EPL (Europhysics Letters)*, **97**, 65002, (2012).

[29] C. Biloiu, X. Sun, E. Choueiri, F. Doss, E. Scime, J. Heard, R. Spektor, and D. Ventura, "Evolution of the parallel and perpendicular ion velocity distribution functions in pulsed helicon plasma sources obtained by time resolved laser induced fluorescence", *Plasma Sources Science and Technology*, **14**, 766, (2005).

[30] S. D. Baalrud, T. Lafleur, R. W. Boswell, and C. Charles, "Particle-in-cell simulations of a current-free double layer", *Physics of Plasmas*, **18**, 063502, (2011), doi: 10.1063/1.3594565.

[31] M. A. Lieberman and C. Charles, "Theory for Formation of a Low-Pressure, Current-Free Double Layer", *Phys. Rev. Lett.*, **97**, 045003, (2006), doi: 10.1103/PhysRevLett.97.045003.

[32] A. Meige, R. Boswell, C. Charles, J.-P. Boeuf, G. Hagelaar, and M. Turner, "One-dimensional simulation of an ion beam generated by a current-free double-Layer", *Plasma Science, IEEE Transactions on*, **33**, 334, (2005), ISSN 0093-3813, doi: 10.1109/TPS.2005.844956.

[33] K. Takahashi and T. Fujiwara, "Observation of weakly and strongly diverging ion beams in a magnetically expanding plasma", *Applied Physics Letters*, **94**, 061502, (2009), doi: 10.1063/1.3080205.

[34] K. Takahashi, Y. Igarashi, and T. Fujiwara, "Plane and hemispherical potential structures in magnetically expanding plasmas", *Applied Physics Letters*, **97**, 041501, (2010), doi: 10.1063/1.3467857.

[35] K. Takahashi, Y. Itoh, and T. Fujiwara, "Operation of a permanent-magnets- expanding plasma source connected to a large-volume diffusion chamber", *Journal of Physics D: Applied Physics*, **44**, 015204, (2011), doi: 10.1088/0022-3727/44/1/015204.

[36] Z. Harvey, S. C. Thakur, A. Hansen, R. Hardin, W. S. Przybysz, and E. E. Scime, "Comparison of gridded energy analyzer and laser induced fluorescence measurements of a two-component ion distribution", *Review of Scientific Instruments*, **79**, 10F314, (2008), doi: 10.1063/1.2953411.

[37] G. Severn, D. A. Edrich, and R. McWilliams, "Argon ion laser-induced fluorescence with diode lasers", *Review of Scientific Instruments*, **69**, 10, (1998), ISSN 0034-6748, doi: 10.1063/1.1148472.

[38] M. J. Goeckner, J. Goree, and T. E. Sheridan, "Laser induced fluorescence characterization of a multidipole filament plasma", *Physics of Fluids B: Plasma Physics*, **3**, 2913, (1991), doi: 10.1063/1.859924.

[39] R. F. Boivin and E. E. Scime, "Laser induced fluorescence in Ar and He plasmas with a tunable diode laser", *Review of Scientific Instruments*, **74**, 4352, (2003), doi: 10.1063/1.1606095.

[40] X. Sun, C. Biloiu, R. Hardin, and E. E. Scime, "Parallel velocity and temperature of argon ions in an expanding, helicon source driven plasma", *Plasma Sources Science and Technology*, **13**, 359, (2004).

[41] S. C. Thakur, A. Hansen, and E. E. Scime, "Threshold for formation of a stable double layer in an expanding helicon plasma", *Plasma Sources Science and Technology*, **19**, 025008, (2010).

[42] Å. Fredriksen, L. N. Mishra, and H. S. Byhring, "The effects of downstream magnetic field on current-free double layers and beam formation in the Njord helicon plasma device", *Plasma Sources Science and Technology*, **19**, 034009, (2010), doi: 10.1088/0963-0252/19/3/034009.

[43] P. A. Keiter, E. E. Scime, and M. M. Balkey, "Frequency dependent effects in helicon plasmas", *Physics of Plasmas*, **4**, 2741, (1997), doi: 10.1063/1.872142.

[44] E. E. Scime, P. A. Keiter, M. M. Balkey, R. F. Boivin, J. L. Kline, M. Blackburn, and S. P. Gary, "Ion temperature anisotropy limitation in high beta plasmas", *Physics of Plasmas*, **7**, 2157, (2000), doi: 10.1063/1.874036.

[45] H. M. Mott-Smith and I. Langmuir, "The Theory of Collectors in Gaseous Discharges", *Phys. Rev.*, **28**, 727, (1926), doi: 10.1103/PhysRev.28.727.

[46] R. L. Merlino, "Understanding Langmuir probe current-voltage characteristics", *American Journal of Physics*, **75**, 1078, (2007), doi: 10.1119/1.2772282.

[47] A. Savitzky and M. J. E. Golay, "Smoothing and Differentiation of Data by Simplified Least Squares Procedures.", *Analytical Chemistry*, **36**, 1627, (1964), doi: 10.1021/ac60214a047.

[48] F. Magnus and J. T. Gudmundsson, "Digital smoothing of the Langmuir probe I-V characteristic", *Review of Scientific Instruments*, **79**, 073503, (2008), doi: 10.1063/1.2956970.

[49] F. F. Chen, "Langmuir probe measurements in the intense RF field of a helicon discharge", *Plasma Sources Science and Technology*, **21**, 055013, (2012), doi: 10.1088/0963-0252/21/5/055013.

[50] I. D. Sudit and F. F. Chen, "RF compensated probes for high-density discharges", *Plasma Sources Science and Technology*, **3**, 162, (1994), doi: 10.1088/0963-0252/3/2/006.

[51] R. F. Kemp and J. M. Sellen, "Plasma Potential Measurements by Electron Emissive Probes", *Review of Scientific Instruments*, **37**, 455, (1966), doi: 10.1063/1.1720213.

[52] J. R. Smith, N. Hershkowitz, and P. Coakley, "Inflection-point method of interpreting emissive probe characteristics", *Review of Scientific Instruments*, **50**, 210, (1979), doi: 10.1063/1.1135789.

[53] E. Y. Wang, N. Hershkowitz, T. Intrator, and C. Forest, "Techniques for using emitting probes for potential measurement in rf plasmas", *Review of Scientific Instruments*, **57**, 2425, (1986), doi: 10.1063/1.1139088.

[54] M. Y. Ye and S. Takamura, "Effect of space-charge limited emission on measurements of plasma potential using emissive probes", *Physics of Plasmas*, **7**, 3457, (2000), doi: 10.1063/1.874210.

[55] J. P. Sheehan, Y. Raitses, N. Hershkowitz, I. Kaganovich, and N. J. Fisch, "A comparison of emissive probe techniques for electric potential measurements in a complex plasma", *Physics of Plasmas*, **18**, 073501, (2011), doi: 10.1063/1.3601354.

[56] I. H. Hutchinson, *Principles of plasma diagnostics*, Cambridge University Press, Cambridge, 1987.

[57] J. A. Simpson, "Design of Retarding Field Energy Analyzers", *Review of Scientific Instruments*, **32**, 1283, (1961), doi: 10.1063/1.1717235.

[58] M. Wiebold, Y.-T. Sung, and J. E. Scharer, "Experimental observation of ion beams in the Madison Helicon eXperiment", *Physics of Plasmas*, **18**, 063501, (2011), doi: 10.1063/1.3596537.

[59] C. Böhm and J. Perrin, "Retarding-field analyzer for measurements of ion energy distributions and secondary electron emission coefficients in low-pressure radio frequency discharges", *Review of Scientific Instruments*, **64**, 31, (1993), doi: 10.1063/1.1144398.

[60] D. Gahan, S. Daniels, C. Hayden, D. O. Sullivan, and M. B. Hopkins, "Characterization of an asymmetric parallel plate radio-frequency discharge using a retarding field energy analyzer", *Plasma Sources Science and Technology*, **21**, 015002, (2012), doi: 10.1088/0963-0252/21/1/015002.

[61] G. D. Conway, A. J. Perry, and R. W. Boswell, "Evolution of ion and electron energy distributions in pulsed helicon plasma discharges", *Plasma Sources Science and Technology*, **7**, 337, (1998), doi: 10.1088/0963-0252/7/3/012.

[62] R. L. Stenzel, R. Williams, R. Agüero, K. Kitazaki, A. Ling, T. McDonald, and J. Spitzer, "Novel directional ion energy analyzer", *Review of Scientific Instruments*, **53**, 1027, (1982), doi: 10.1063/1.1137103.

[63] D. D. Neiswender and F. C. Kohout, "An Apparatus for Electron Energy Analysis in Glow Discharge Plasmas", *Review of Scientific Instruments*, **43**, 1475, (1972), doi: 10.1063/1.1685468.

[64] S. G. Ingram and N. S. J. Braithwaite, "Ion and electron energy analysis at a surface in an RF discharge", *Journal of Physics D: Applied Physics*, **21**, 1496, (1988), doi: 10.1088/0022-3727/21/10/005.

[65] D. Gahan, B. Dolinaj, and M. B. Hopkins, "Comparison of plasma parameters determined with a Langmuir probe and with a retarding field energy analyzer", *Plasma Sources Science and Technology*, **17**, 035026, (2008), doi: 10.1088/0963-0252/17/3/035026.

[66] C. P. DeNeef and A. J. Theiss, "Effect of finite analyzer size on the distribution functions measured in field-free plasmas", *Review of Scientific Instruments*, **50**, 378, (1979), doi: 10.1063/1.1135832.

[67] N. Gulbrandsen, Å. Fredriksen, J. Carr, and E. Scime, "A comparison of ion beam measurements by retarding field energy analyzer and laser induced fluorescence in helicon plasma devices", *Physics of Plasmas*, **22**, 033505, (2015), doi: 10.1063/1.4913990.

[68] G. A. Emmert, R. M. Wieland, A. T. Mense, and J. N. Davidson, "Electric sheath and presheath in a collisionless, finite ion temperature plasma", *Physics of Fluids*, **23**, 803, (1980), doi: 10.1063/1.863062.

[69] W. J. Miloch, N. Gulbrandsen, L. N. Mishra, and Å. Fredriksen, "The role of acceptance angle in measurements with ion energy analyzers: Study by numerical simulations", *Applied Physics Letters*, **97**, 261501, (2010), doi: 10.1063/1.3531757.

[70] E. Leal-Quiros and M. Prelas, "An enhancement of ion energy spectra resolution and sensitivity in a multigridded energy analyzer with a retarding grid potential: the variable energy analyzer (VEA)", *Plasma Science, IEEE Transactions on*, **16**, 661 , (1988), ISSN 0093-3813, doi: 10.1109/27.16555.

[71] Y. Sakai and I. Katsumata, "An Energy Resolution Formula of a Three Plane Grids Retarding Field Energy Analyzer", *Japanese Journal of Applied Physics*, **24**, 337, (1985).

[72] C. Charles, A. W. Degeling, T. E. Sheridan, J. H. Harris, M. A. Lieberman, and R. W. Boswell, "Absolute measurements and modeling of radio frequency electric fields using a retarding field energy analyzer", *Physics of Plasmas*, **7**, 5232, (2000), doi: 10.1063/1.1322557.

[73] N. Gulbrandsen, W. J. Miloch, and Å. Fredriksen, "Interpretation of Ion Velocity Distributions Measured with a Grounded Retarding Field Energy Analyzer (RFEA) in an Inductively Coupled Helicon Plasma", *Contributions to Plasma Physics*, **53**, 27, (2013), ISSN 1521-3986, doi: 10.1002/ctpp.201310005.

[74] W. J. Miloch, N. Gulbrandsen, L. N. Mishra, and Å. Fredriksen, "Ion velocity distributions in the sheath and presheath of a biased object in plasma", *Physics of Plasmas*, **18**, 083502, (2011), doi: 10.1063/1.3614520.

[75] J. M. Buzzi, H. J. Doucet, and D. Gresillon, "Ion Distribution Functions in Collisionless Surface Ionized Plasmas", *Physics of Fluids*, **13**, 3041, (1970), doi: 10.1063/1.1692899.

[76] S. A. Andersen, V. O. Jensen, P. Michelsen, and P. Nielsen, "Determination and Shaping of the Ion-Velocity Distribution Function in a Single-Ended Q Machine", *Physics of Fluids*, **14**, 728, (1971), doi: 10.1063/1.1693495.

[77] Y. Hamada, Y. Kawasumi, H. Iguchi, A. Fujisawa, Y. Abe, and M. Takahashi, "Mesh effect in a parallel plate analyzer", *Review of Scientific Instruments*, **65**, 1606, (1994), doi: 10.1063/1.1144900.

[78] V. Kanarov, D. Siegfried, P. Sferlazzo, A. Hayes, and R. Yevtukhov, "High resolution energy analyzer for broad ion beam characterization", *Review of Scientific Instruments*, **79**, 093304, (2008), doi: 10.1063/1.2972175.

[79] K. Takahashi, C. Charles, R. Boswell, W. Cox, and R. Hatakeyama, "Transport of energetic electrons in a magnetically expanding helicon double layer plasma", *Applied Physics Letters*, **94**, 191503, (2009), ISSN 0003-6951, doi: 10.1063/1.3136721.

[80] D. Gahan, S. Daniels, C. Hayden, P. Scullin, D. O'Sullivan, Y. T. Pei, and M. B. Hopkins, "Ion energy distribution measurements in rf and pulsed dc plasma discharges", *Plasma Sources Science and Technology*, **21**, 024004, (2012), doi: 10.1088/0963-0252/21/2/024004.

[81] R. A. Stern and J. A. Johnson, "Plasma Ion Diagnostics Using Resonant Fluorescence", *Phys. Rev. Lett.*, **34**, 1548, (1975), doi: 10.1103/PhysRevLett.34.1548.

[82] D. N. Hill, S. Fornaca, and M. G. Wickham, "Single frequency scanning laser as a plasma diagnostic", *Review of Scientific Instruments*, **54**, 309, (1983), doi: 10.1063/1.1137389.

[83] P. Schef, A. Derkatch, P. Lundin, S. Mannervik, L.-O. Norlin, D. Rostohar, P. Royen, and E. Biémont, "Lifetimes of metastable levels in Ar II", *The European Physical Journal D*, **29**, 195, (2004), doi: 10.1140/epjd/e2004-00043-1.

[84] A. K. Hansen, M. Galante, D. McCarren, S. Sears, and E. E. Scime, "Simultaneous two-dimensional laser-induced-fluorescence measurements of argon ionsa)", *Review of Scientific Instruments*, **81**, 10D701, (2010), doi: 10.1063/1.3460630.

[85] J. Carr, Jr., *Laser Induced Fluorescence Studies of Electrostatic Double Layers in an Expanding Helicon Plasma*, PhD thesis, West Virginia University, 2013.

[86] R. F. Boivin, Study of The Different Line Broadening Mechanisms for the Laser Induced Fluorescence Diagnostic of the HELIX and LEIA Plasmas, Technical Report PL-039, West Virginia University, Morgantown, USA, (2002).

[87] R. F. Boivin, Zeeman Splitting for LIF Transitions and De-Convolution Technique to Extraction Temperatures, Technical Report PL-050, West Virginia University, Morgantown, USA, (2002).

[88] N. Gulbrandsen and Å. Fredriksen, "RFEA Measurements of High-Energy Electrons in a Helicon Plasma Device with Expanding Magnetic Field", *Frontiers in Physics*, **5**, 2, (2017), ISSN 2296-424X, doi: 10.3389/fphy.2017.00002.